

**FABRICATION AND CHARACTERIZATION  
OF THIN FILMS AND COATINGS**

by

Timothy James Miller

A dissertation submitted to the Faculty of the University of Delaware in partial fulfillment of the requirements for the degree of Doctor of Philosophy in Chemistry and Biochemistry

Winter 2015

© 2015 Timothy James Miller  
All Rights Reserved

UMI Number: 3685336

All rights reserved

INFORMATION TO ALL USERS

The quality of this reproduction is dependent upon the quality of the copy submitted.

In the unlikely event that the author did not send a complete manuscript and there are missing pages, these will be noted. Also, if material had to be removed, a note will indicate the deletion.



UMI 3685336

Published by ProQuest LLC (2015). Copyright in the Dissertation held by the Author.

Microform Edition © ProQuest LLC.

All rights reserved. This work is protected against unauthorized copying under Title 17, United States Code



ProQuest LLC.  
789 East Eisenhower Parkway  
P.O. Box 1346  
Ann Arbor, MI 48106 - 1346

**FABRICATION AND CHARACTERIZATION  
OF THIN FILMS AND COATINGS**

by

Timothy James Miller

Approved:

---

Murray V. Johnston, Ph.D.  
Chair of the Department of Chemistry and Biochemistry

Approved:

---

George H. Watson, Ph.D.  
Dean of the College of Arts and Sciences

Approved:

---

James G. Richards, Ph.D.  
Vice Provost for Graduate and Professional Education

I certify that I have read this dissertation and that in my opinion it meets the academic and professional standard required by the University as a dissertation for the degree of Doctor of Philosophy.

Signed:

---

Andrew V. Teplyakov, Ph.D.  
Professor in charge of dissertation

I certify that I have read this dissertation and that in my opinion it meets the academic and professional standard required by the University as a dissertation for the degree of Doctor of Philosophy.

Signed:

---

Cecil Dybowski, Ph.D.  
Member of dissertation committee

I certify that I have read this dissertation and that in my opinion it meets the academic and professional standard required by the University as a dissertation for the degree of Doctor of Philosophy.

Signed:

---

Karl S. Booksh, Ph.D.  
Member of dissertation committee

I certify that I have read this dissertation and that in my opinion it meets the academic and professional standard required by the University as a dissertation for the degree of Doctor of Philosophy.

Signed:

---

Michael E. Mackay, Ph.D.  
Member of dissertation committee

## ACKNOWLEDGMENTS

I would not be where I am today with the help and guidance of so many others. First and foremost, my deepest gratitude goes to my advisor, Prof. Andrew V. Teplyakov, who knew to push the right buttons and was always there to bounce ideas off of. Further acknowledgement goes to my committee members: Prof. Cecil Dybowski, Prof. Karl S. Booksh, and Prof. Michael E. Mackay.

All past and present members Teplaykov group are also greatly thanked. They were my HF acid etching “buddies”, instrument trainers, and idea bouncers. Gratitude goes to Prof. Mackay, Dr. Jon Kiel, and Mr. Roddel Remy for materials and direction. Thanks goes to Prof. Robert L. Opila, Dr. Fang Fang, Dr. Dan Yang, and Mr. Kevin Jones for XPS measurements as well as Prof. Opila and Prof. Anette M. Karlsson for use the nanoindentation instrument. Prof. Thomas P. Beebe, Dr. Holt Bui, and Mr. Zachary Voras of the Surface Analysis Facility are acknowledged for further XPS and ToF-SIMS measurements while Prof. Booksh, Dr. Laurel Kegel, and Ms. Devon Boyne are thanked for help with the ATR-IR measurements. Dr. Chaoying Ni, Mr. Frank Kriss, Dr. Fei Deng, and Dr. Jennifer Sloppy at the W.M. Keck Electron Microscopy Facility are deeply thanks for AFM, SEM, and TEM training and help. Prof. Ismat Shah and Mr. Roy Murray are thanked for XRD measurements.

Dr. Laurent Pirolli is deeply thanked for the internship opportunity at Schlumberger. Mr. Derrick Allen is thanked for the mechanical cutting of coupons down to the precise sizes I could analyze, and Mr. Jim Draper and Mr. John Famiglietti are thanked for their electrical expertise.

I would like to thank the University of Delaware, NSF's IGERT program, Schlumberger Technology Corp., and NSF grants CHE-0650123 and CHE-1057374 for funding throughout my research.

Lastly, I would like to thank my family and friends for their love and support throughout my life.

## TABLE OF CONTENTS

LIST OF TABLES .....	x
LIST OF FIGURES .....	xi
ABSTRACT .....	xvi

### Chapter

1	INTRODUCTION .....	1
1.1	Introduction to Surface and Interfacial Chemistry .....	1
1.2	Thin Films for Photovoltaic Applications .....	2
1.3	Thin Film's and Coating's Role in Protective Applications .....	7
1.4	Novel Wet-Chemical Deposition of Nanoparticles .....	12
1.5	Scope and Outline of the Dissertation .....	14
2	EXPERIMENTAL PROCEDURES AND INSTRUMENTATION.....	15
2.1	Introduction .....	15
2.2	Chemicals Used and Preparation Procedures .....	15
2.2.1	Monolayer Preparation of Amino-Terminated Si(111) Surface..	15
2.2.2	TDMAT Chemical Vapor Deposition Procedure .....	17
2.2.3	Electrospark Deposition of TiCN and WC coatings .....	18
2.2.4	Nanoparticle Layer-by-Layer Growth .....	19
2.3	Instrumentation Used and Theory .....	21
2.3.1	X-ray Photoelectron Spectroscopy .....	21
2.3.2	Auger Electron Spectroscopy .....	23
2.3.3	Fourier Transform Infrared Spectroscopy .....	24
2.3.4	Atomic Force Microscopy .....	27
2.3.5	Time of Flight Secondary Ion Mass Spectroscopy.....	28
2.3.6	Scanning Electron Microscopy, Energy-dispersive X-ray Spectroscopy, Focused Ion Beam.....	29
2.3.7	Transmission Electron Microscopy .....	32
2.3.8	X-ray Diffraction .....	33
2.3.9	Mechanical NanoIndentation Characterization .....	33

3	ATTACHMENT CHEMISTRY OF PCBM TO A PRIMARY-AMINE-TERMINATED ORGANIC MONOLAYER ON A SI(111) SURFACE .....	36
3.1	Abstract .....	36
3.2	Introduction .....	36
3.3	Experimental Details .....	38
3.3.1	Monolayer Preparation .....	38
3.3.2	Surface Characterization .....	40
3.3.3	Computational Details .....	40
3.4	Results and Discussion .....	41
3.4.1	Interrogation of the Monolayer Formation and PCBM Adsorption by XPS .....	41
3.4.2	Topography Changes Followed by AFM .....	46
3.4.3	Vibrational Identification of Surface Species Produced by PCBM Modification .....	49
3.4.4	Identification of the PCBM Chemisorption Structure by ToF-SIMS .....	52
3.4.5	Analysis of the Formation of Possible PCBM Chemisorption Structures by DFT .....	55
3.5	Conclusions .....	58
4	INVESTIGATION OF THIN TITANIUM CARBONITRIDE COATINGS DEPOSITED ONTO A 4140 STEEL SUBSTRATE .....	60
4.1	Abstract .....	60
4.2	Introduction .....	61
4.3	Experimental Details .....	61
4.3.1	TDMAT Deposition Procedure .....	61
4.3.2	Coating Characterization .....	62
4.4	Results and Discussion .....	62
4.4.1	Coating Chemical Concentration Ratios and Chemical State Analysis .....	62
4.4.2	Cross-sectional Analysis of Coating, Interface, and Substrate....	65
4.4.3	Substrate and Coating Topography .....	70
4.4.4	Mechanical Properties of the Substrate and Deposited Coating .	72
4.5	Conclusions .....	73

5	INVESTIGATION OF THICK TITANIUM CARBONITRIDE AND TUNGSTEN CARBIDE COATINGS DEPOSITED ONTO A 4140 STEEL SUBSTRATE .....	75
5.1	Abstract .....	75
5.2	Introduction .....	75
5.3	Experimental Procedures.....	78
5.3.1	Deposition Methods.....	78
5.3.2	Characterization Techniques .....	78
5.4	Results and Discussion.....	78
5.4.1	ESD Deposited Chemical States .....	78
5.4.2	Topographic and Cross-sectional Analysis of Coating, Interface, and Substrate .....	81
5.4.3	TEM Investigation of the Interfaces in ESD-produced Coatings.....	86
5.4.4	Crystalline Structure of the ESD Coatings, Interfaces, and Substrate .....	89
5.4.5	Topography of the ESD Coatings' Surfaces .....	91
5.4.6	Mechanical properties of ESD coatings .....	93
5.5	Conclusions .....	94
6	NOVEL NANOPARTICLE DEPOSITION TECHNIQUE USING “CLICK CHEMISTRY” .....	96
6.1	Abstract .....	96
6.2	Introduction .....	96
6.3	Experimental Procedure .....	101
6.3.1	Sample Preparation.....	101
6.3.2	Surface Characterization .....	101
6.4	Results and Discussion.....	102
6.4.1	Proof of Chemical Reactions in NPLD .....	102
6.4.2	Surface Coverage and Microscopy Studies.....	108
6.5	Conclusions .....	112
7	SUMMARY AND FUTURE WORK.....	113
7.1	Thin Films for Photovoltaic Applications.....	113

7.2	Thin Film TiCN Protective Coating for Perfect Deposition .....	114
7.3	Thin Film TiCN Protective Coating by Practical Deposition Methods	115
7.4	Novel Wet-Chemistry-Based Nanoparticle Deposition .....	116
7.5	Overall Conclusions .....	117
REFERENCES .....		118
Appendix		
A	DFT MODEL XYZ COORDINATES .....	133
B	COPYRIGHT PERMISSIONS .....	145

## LIST OF TABLES

Table 1.1:	Comparison of selected coatings with a common steel substrate. ....	11
Table 5.1:	Young's modulus of ESD-deposited TiCN, WC and substrate steel, GPa. ....	93
Table A.1:	PCBM Coordinates.....	133
Table A.2:	Si111-AUD Coordinates .....	135
Table A.3:	Si111-AUD-PCBM <b>Structure 1</b> Coordinates .....	137
Table A.4:	Si111-AUD-PCBM <b>Structure 2</b> Coordinates .....	141

## LIST OF FIGURES

- Figure 1.1: The figure shows the (a) energy diagram of a photovoltaic cell Polymeric solar cell heterojunctions; (b) planar heterojunction; (c) bulk heterojunction; and (d) ordered heterojunction. Figure 2 in reference [27], reproduced under Creative Commons License 3.0. .... 4
- Figure 2.1: Common vibration modes in an organic molecule. They are (a) asymmetrical, (b) symmetrical, (c) scissoring, (d) rocking, (e) twisting, and (f) wagging. The blue and red lines indicate the direction of atom movement. The direction indicated alternates between red and blue. .... 25
- Figure 3.1: Schematic diagram of the chemical modification steps performed. A H-terminated Si(111) wafer is refluxed in *t*-BOC protected 1-amino-10-undecene under N<sub>2</sub> followed by deprotection in TFA and NH<sub>4</sub>OH. The deprotected AUD SAM is then exposed to the PCBM. The final product may be the result of the PCBM reacting through its ester functionality to form an amide with the SAM (**Structure 1**) or through its C<sub>60</sub> frame (**Structure 2**). .... 39
- Figure 3.2: High-resolution XPS spectra of: 3.2(a,d,g) C 1s, N 1s, and Si 2p regions, respectively, for H-terminated Si(111) surface; 3.2(b,e,h) C 1s, N 1s, and Si 2p regions, respectively, for AUD-Si(111) surface; and 3.2(c,f,i) C 1s, N 1s, and Si 2p regions, respectively, for PCBM-AUD-Si(111) surface. .... 43
- Figure 3.3: N 1s region of Si(111)-AUD-PCBM sample in addition to Si(111)-AUD (black line), Si(111)-AUD-PCBM **Structure 2** (blue line), and Si(111)-AUD-PCBM **Structure 1** (red line) models. .... 46
- Figure 3.4: AFM images of: (a) H-terminated Si(111) wafer; (b) AUD-modified Si(111), (c) PCBM-terminated Si(111) wafer (exposure time 3 hours), (d) PCBM-terminated Si(111) wafer (exposure time 5 hours). The corresponding line profiles (white lines in each figure) are shown as an inset in each image. .... 47

Figure 3.5: Experimental and computational investigation of PCBM adsorption on AUD-functionalized Si(111) surface: (a) experimental spectrum for PCBM in KBr; (b) experimental spectrum for Si(111)-AUD-PCBM-5 hr system; (c) the product of AUD reaction with PCBM in KBr pellet; (d) the DFT-predicted spectrum of PCBM; (e) the DFT-predicted spectrum for <b>Structure 2</b> ; and (f) the DFT-predicted spectrum for <b>Structure 1</b> . The background spectra for the experimental studies presented in (a) and (c) were collected with a pure KBr pellet. AUD-functionalized silicon sample was used as a background for spectrum (b). .....	51
Figure 3.6: The ToF-SIMS results for the OCH <sub>3</sub> <sup>-</sup> and C <sub>60</sub> N <sup>-</sup> regions for (a,f) Si(111)-AUD-PCBM (5 hr); (b,g) Si(111)-AUD-PCBM (3 hr); (c,h) analogous AUD-PCBM experiment; (d,i) molecular PCBM; and (e,j) Si(111)-AUD. The constant presence of the OCH <sub>3</sub> <sup>-</sup> peak at <i>m/z</i> 31.02 and presence of the C <sub>60</sub> N <sup>-</sup> peak at <i>m/z</i> 734.984 are indicative of the <b>Structure 2</b> product. ....	54
Figure 3.7: Optimized models of (a) product <b>Structure 1</b> and (b) product <b>Structure 2</b> . Methanol is also a product of the reaction resulting in <b>Structure 1</b> but it is not shown. The N 1s core level energy comparison used to compare with the experimental XPS spectra utilized these models. ....	56
Figure 3.8: Graphical representation of the gas phase rest energies of the reactant, products, and transition states of the propylamine and PCBM reaction. The reactants were set to 0.0 kJ/mol and the relative rest energies of the products and transition states were compared to rest value. ....	57
Figure 4.1: AES for TiCN films prepared by 3.0 x 10 <sup>4</sup> L exposure of TDMAT onto a clean 4140 steel surface under UHV conditions. ....	63
Figure 4.2: XPS spectra of (a) carbon 1s, (b) nitrogen 1s, (c) oxygen 1s, and (d) titanium 2p for TiCN films prepared by 3.0 x 10 <sup>4</sup> L exposure of TDMAT onto a clean stainless steel surface under UHV conditions.....	64
Figure 4.3: ToF-SIMS depth profile of UHV-deposited TiCN. The signals corresponding to selected species have been scaled as indicated to show their relative concentration throughout the sample.....	66
Figure 4.4: Cross-sectional TEM image of 3.0 x 10 <sup>4</sup> L TiCN film. Two distinct regions are seen: the TiCN layer and the 4140 steel substrate. A carbon layer was used to protect the TiCN layer while cutting. ....	69

Figure 4.5: AFM image of uncoated 4140-series steel sputtered in UHV conditions (a and c) with respective line profile shown in (c) and AFM images of UHV-deposited TiCN coating (b and d) with respective line profile shown in (d). The line profiles for the micro scale images are shown underneath each image. The scale bars are shown at the bottom of each image.....	71
Figure 5.1: XPS analysis of ESD coatings and the steel substrate of the (a) titanium $2p$ , (b) tungsten $4f$ , and (c) iron $2p$ regions.....	79
Figure 5.2: Surface (plane view) SEM images for (a) TiCN and (b) WC coatings at 250 X magnification. Both exhibit typical splash patterns commonly observed for electrospray-deposited coatings. ....	81
Figure 5.3: Surface (plane view) SEM images for (a) TiCN and (b) WC coatings at 10000 X magnification. Both images were magnifications of the splash patterns seen in Figure 5.2. The TiCN coating is significantly rougher than the WC. ....	82
Figure 5.4: SEM cross-section for ESD WC with linescan EDX. The white dashed line in the SEM image represents the WC coating-substrate interface. The red line plots relative Fe concentration in counts-per-second (CPS) along the linescan, the black line plots the relative W (CPS) along the linescan, and the blue line plots the relative C (CPS) along the linescan. The black dashed line in the line profile represents the WC coating-substrate interface. ....	84
Figure 5.5: SEM cross-section for TiCN with linescan EDX. The white dashed line in the SEM image represents the WC coating-substrate interface. The red line plots relative Fe concentration in counts-per-second (CPS) along the linescan, the black line plots the relative Ti (CPS) along the linescan, the blue line plots the relative C (CPS) along the linescan, and the yellow line plots the relative N (CPS) along the linescan.....	86
Figure 5.6: TEM images of (a-b) WC and (c-d) TiCN coatings deposited by ESD. The images on the left show the general area of the interface while the images on the right show a high magnification zoom-in. ....	88
Figure 5.7: XRD investigation of (a) 4140 steel, (b) WC ESD coating on a 4140 steel coupon, (c) TiCN ESD coating on a 4140 steel coupon, (d) a zoom-in (x20) of the TiCN ESD coating on a 4140 steel coupon, (e) TiCN electrode used to deposit TiCN coating for a sample characterized in (c-d).....	91

- Figure 5.8: Representative 500 nm by 500 nm images of (a) TiCN and (b) WC coated samples. The common depth scale is given on the right. The scale bars are shown at the bottom of each image. .... 92
- Figure 6.1: Morphological changes after “click chemistry” of functionalized nanoparticles. Figures (a,c) show non-functionalized iron nanoparticles at low and high magnification, respectively. Figures (b,d) show the iron nanoparticles after “click chemistry”. Figures (a) and (b) are at the same magnification (50K), and (c) and (d) are at the same magnification (200K). Figure adapted from reference [79]. .... 98
- Figure 6.2: Basic scheme of layer-by-layer (LbL) nanoparticle deposition. After the surface is modified with an azide-terminated layer, an alkyne functionalized 80 nm nanoparticle reacts with the surface. The subsequent alkyne-terminated reacts with azide functionalized 50 nm particles. This cycle could theoretically repeat endlessly for the LbL deposition. .... 99
- Figure 6.3: ATR FT-IR spectra of (a) 11-azidoundecanethiol modified Au substrate; (b) 80-nm alkyne functionalized nanoparticles deposited onto sample (a); (c) 50-nm azide functionalized nanoparticles deposited on sample (b); and (d) 80-nm alkyne functionalized nanoparticles deposited on sample (c). .... 103
- Figure 6.4: XPS studies of each layer of nanoparticle deposition. On the left is the C 1s region, and the right shows the N 1s region of: (a,e) the azide-terminated gold surface; (b,f) the alkyne 80-nm nanoparticle deposited onto azide-terminated gold surface; (c,g) the azide 50-nm nanoparticles deposited onto the first 80-nm nanoparticle layer; and (d,h) the second 80-nm alkyne nanoparticle layer on the 50-nm azide nanoparticle layer. The solid lines in the N 1s region show to the predicted energy shifts from DFT calculations. The colors of each bar correspond with the colors of the model, and the lighter lines show the azide information while the darker lines provide information for the triazole ring compound. .... 106

Figure 6.5: SEM studies to determine the surface coverage and film thickness. The figure shows: (a) the 80-nm alkyne nanoparticle-deposited layer surface (plane view); (b) the cross sectional view 80-nm alkyne nanoparticle layer; (c) the 50-nm azide nanoparticle deposited layer surface (plane view) deposited on top of the first layer; (d) the cross sectional view of 50-nm azide nanoparticles layer deposited on top of the first layer; (e) the second 80-nm alkyne nanoparticle deposited layer surface (third overall layer, plane view); and (f) the second cross sectional view of the three-layer system. .... 109

Figure 6.6: Control experiments to show the importance of the complementary chemistry and the stable nature of the triazole ring. The figure shows (a) the same procedure for first layer nanoparticle deposition sans for azide termination of the gold substrate and washing; (b) the same procedure for first layer nanoparticle deposition sans for azide termination of the gold substrate; and (c) the procedure as written (for reference)..... 111

## **ABSTRACT**

Surface and interfacial chemistry is a major, well-researched topic in science. From microelectronics to biosensors to catalysis, surface chemistry research is applicable to many different areas. This dissertation focuses on three of these areas: photovoltaics, protective coatings, and a novel nanoparticle deposition procedure. These three areas are all related through energy-related research. An additional focus is placed on the understanding of the systems' chemistries at the molecular level. Several surface spectroscopic and microscopic techniques are utilized to understand the systems. Spectroscopic techniques include Fourier-transform infrared spectroscopy (FT-IR), X-ray photoelectron spectroscopy (XPS), time-of-flight secondary ion mass spectroscopy (ToF-SIMS), and X-ray diffraction (XRD). Surface microscopic techniques include scanning electron microscopy (SEM), transmission electron microscopy (TEM), atomic force microscopy (AFM). Additionally, nanoindentation measurements are used to determine Young's modulus for the protective coatings. For some studies, density functional theory models were used to complement experimental results, and predict pathways.

## **Chapter 1**

### **INTRODUCTION**

#### **1.1 Introduction to Surface and Interfacial Chemistry**

Surface and interfacial science is an interdisciplinary, wide-ranging, and well-studied field in science and engineering. Although the terms are in some instances used interchangeably, surface science nominally applies to the studies of the interactions between two different phases (e.g. solid-liquid, solid-gas, etc.) while interfacial science addresses the interactions at any boundary between phases, regardless of their types. The concepts of surface and interfacial science are relevant to microelectronics [1], responsive sensors [2], protective coatings [3], and photovoltaics [4] as well as many other fields.

Surface science and, specifically, surface chemistry discoveries give us better understanding and new insights into phenomena that could increase our quality of life. The applications for surface science are numerous and the scales can vary from nanometers (e.g. microelectronics) to micrometers (e.g. protective coatings). The science in these experiments involves the basic principle of how a surface or coating interacts with the environment to which it is subjugated, regardless of the name of the scale.

Over the course of the thesis, different applications of surface and interfacial science are described and investigated. These projects, which range from surface functionalization to protective coatings, are all connected through surface science and chemistry. The overarching theme of the entire work is the relevance of surface

processes to the energy sector, one of the largest industries in the world with over \$2 billion in sales each year [5]. Although research in the energy sector covers a wide variety of topics and length scales [6-14], it is often at the surface or interface of the materials that the chemistry happens [15, 16]. Fundamental research must be carried out to improve upon these applications because the need for low-cost, low-carbon-emitting energy sources is imperative to protect our world while maintaining the sophistication which leads to the comfortable lifestyle we enjoy [17, 18]. The projects described in this dissertation address several fundamental issues in photovoltaics, protective coatings, and novel materials and are all derived from the molecular-level understanding of surface properties relevant to each kind of chemical system.

## **1.2 Thin Films for Photovoltaic Applications**

An area that provides low-cost, low-carbon-emitting energy technologies is photovoltaic energy [19, 20]. Briefly, photovoltaics use a  $p-n$  junction to produce a voltage difference [20]. Most solar cells on the market today are single and multicrystalline silicon solar cells [20]. Although silicon solar cells are able to produce energy with relatively high efficiencies (25% [21]), there are some drawbacks and challenges. Among them are (1) high initial costs, and (2) energy-intensive processes to remove impurities and convert metallurgical silicon to electronic-grade silicon [22].

There are many different types of photovoltaic cells aside from those based on crystalline silicon [20, 23]. A majority of the different photovoltaic cell types also use silicon but some variants, such as copper indium gallium diselenide and cadmium telluride, do not. Another type of photovoltaic cell that does not use metal in the active layer is an organic/polymer photovoltaic (OPV) cell [24]. This system is very appealing because of (1) the ultrafast optoelectronic response at the interface of the

electron donor and electron acceptor, (2) the tunability of the band gap, (3) the availability of lightweight, flexible, low-cost characteristics, and (4) the possible integration with many other products [25]. Instead of doped metals as the electron donor and acceptor, an OPV cell normally has a polymeric compound as the donor and a fullerene-derived compound as the acceptor [26]. Currently the record for OPV efficiency is 11.1% [23], although most reported high efficiencies hover around 5% [26, 27].

The active layer of an OPV, comprised of the electron donor (*p*-type) and electron acceptor (*n*-type) materials, is sandwiched between indium tin oxide (ITO) covered glass and poly(3,4-ethylenedioxythiophene):poly(styrenesulfonate) (PEDOT:PSS) on one side, and an evaporated metal, such as aluminum, on the other side of the active layer [27, 28]. The ITO and Al are then connected to the load. Common materials for the active layer include PCBM, MDMO-PPV, P3HT, and PCPDTBT. These materials are normally chosen because they are electronically active and because they have strong optical transitions [27]. The active layer architecture (the geometry of the electron donor and electron acceptor) plays a major role in determining the efficiency of the OPV [26, 27].

Figure 1.1(a) shows an energy diagram of a photovoltaic cell [27]. When the electron donor absorbs a photon, the electron is excited from the highest occupied molecular orbital (HOMO, or *valence band*) to the lowest unoccupied molecular orbital (LUMO, or *conduction band*), and an electron-electron hole pair (*exciton*) is created. If the exciton is created at or near an interface, the electron may migrate to the electron acceptor (commonly PCBM) and the exciton pair can further migrate to their respective electrodes while avoiding traps and recombination. It is important that the

exciton is created at or near an interface because the diffusion length of an electron in this system is only on the order of 3-10 nm [29-31]. A number of different device architectures have been created, of which three common types of architecture are the planar heterojunction (Figure 1.1(b)), the bulk heterojunction (Figure 1.1(c)), and the ordered heterojunction (Figure 1.1(d)) [27].

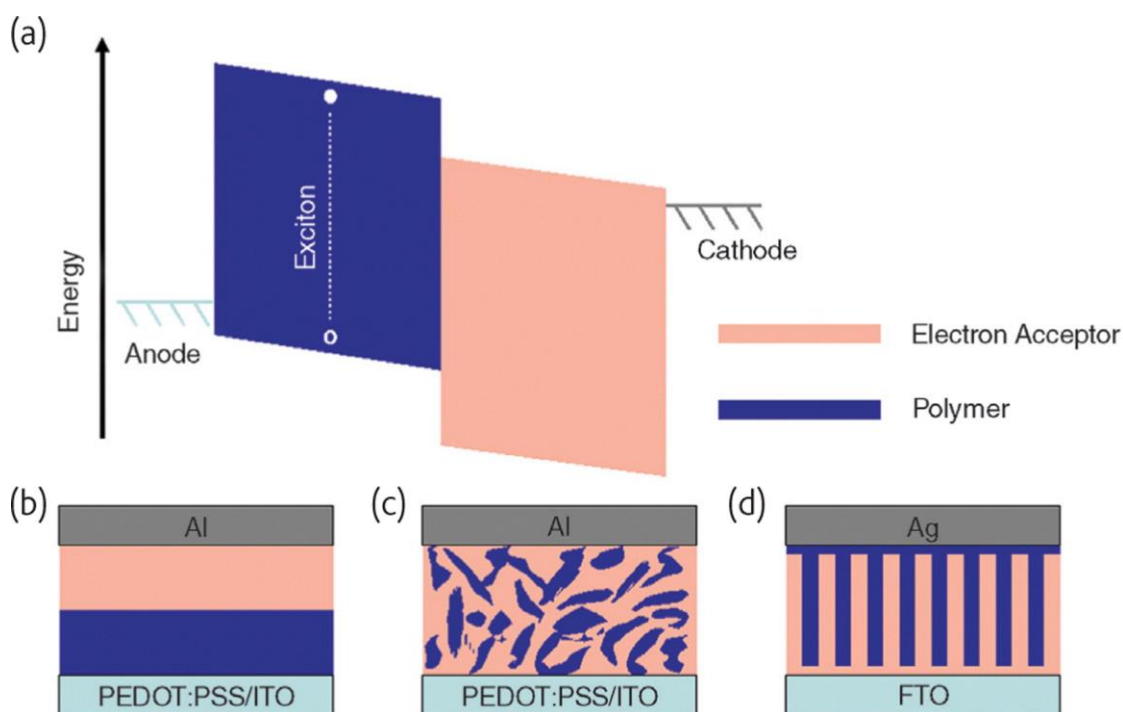


Figure 1.1: The figure shows the (a) energy diagram of a photovoltaic cell Polymeric solar cell heterojunctions; (b) planar heterojunction; (c) bulk heterojunction; and (d) ordered heterojunction. Figure 2 in reference [27], reproduced under Creative Commons License 3.0.

A planar heterojunction is the simplest heterojunction that can be produced. Normally, one layer is spin-coated onto the electrode followed by spin-coatings of the second. This technique results in short formation times and relatively inexpensive

devices. However, this method has drawbacks: 1) the recombination of an electron-electron hole pair is a serious threat to cell efficiency because any exciton created further than 3-10 nm from a donor-acceptor interface is likely to recombine; and 2) the subsequent active region is very thin, so the device is not thick enough to absorb a majority of the solar photons [32]. To overcome these deficiencies, other styles of heterojunctions are fabricated.

Bulk heterojunctions address these problems, and are perhaps the most successful and commonly used type of heterojunction [27, 33-35]. In a bulk heterojunction, the electron donor and acceptor are mixed together in a common solvent and spun coated onto the substrate. It is imperative during processing that the two materials are sufficiently intermixed because insufficient mixing results in recombination from the small exciton diffusion length. Sufficient mixing means that nearly all of the excitons formed cross the interface, and increase the efficiency of the device. Film morphology, thickness, materials, and solvent are all important parameters when fabricating a polymer photovoltaic device [27]. However, as seen in Figure 1.1(c) [27], there still is a possibility that there is insufficient mixing to create regions of large islands where recombination occurs. In addition, there is always the possibility of traps being formed.

Perhaps the most efficient device architecture is the ordered heterojunction [36-38]. In the structure shown in Figure 1.1(d) [27], the small straight pores' diameter are radially less the electron diffusion length while also longitudinally thick enough to absorb the light. Although the power conversion efficiency is not as efficient as for bulk heterojunction geometries, future research is promising [39]. However, a number of factors must still be understood to improve device efficiency. For instance, different

electron donor and electron acceptor materials provide different efficiencies. The chemistry between two different materials is crucial to understand and improve the device efficiency, and without this understanding, device improvement would be impossible.

A major challenge in understanding the behavior of excitons and electrons [40] in organic solar cells is the fact that these systems are mostly disordered and the interfaces involved in the process are not well-defined. A reliable and reproducible method must be used to obtain well-defined model systems to examine the electronic properties and donor/acceptor behavior. One method to produce a reliable and reproducible system is use of a functionalized self-assembled monolayer (SAM) on a Si(111) surface.

By itself, surface functionalization is an important area in surface modification, and it is often needed to attach a linker molecule to a functionalized layer that would react with the macromolecule [41-49]. Surface functionalization techniques are utilized in many different applications and are a well-researched area. They provide a reproducible framework to explore surface chemistry and understand reactions. Organic monolayer surface functionalization is a great candidate to provide a chemical linkage because organic molecules have predictable and controllable chemistry with both the silicon surface (as well as many other types of surfaces) and with the target molecules that must be attached to it.

It is crucial to understand the chemistry of possible new materials in a disordered organic photovoltaic system. By using a silicon functionalization system with self-assembly of an amino-terminated monolayer and a reaction with PCBM, which is not a reaction that has been studied extensively in literature with or without

the silicon monolayer system, to reliably reproduce a system, we can observe this chemistry and could perhaps improve device efficiency.

### **1.3 Thin Film's and Coating's Role in Protective Applications**

A large area of organic photovoltaic research is focused on protection and stability of the photovoltaic cells [50]. As noted in Jørgensen et al. [50], research in processing, power conversion efficiency, and stability are equally important when looking to improve this technology because overall progress requires progress in all three areas simultaneously. Organic photovoltaic materials as well as some electrode materials react poorly with oxygen in the atmosphere. Therefore, the material must be encapsulated with barrier layers and fabricated with care to protect from the ambient environment as well as from harsh UV light and weather [51].

Another research area that focuses on sample protection with coatings is the field of mechanical materials, such as tools and pumps, to increase wear resistance and tool lifetime [52]. Protective coatings combine their unique and tunable properties with the physical properties of substrate materials (hardness, porosity, ease of processing) [3, 53-55]. The coatings are often more expensive than the substrates but offer a wide range of properties that can often be fine-tuned to fit the application.

Protective coatings used for hard tools are one of the quickly developing areas of research and, in this particular case, a high degree of control over not only the coating itself but also over the interface formed between the coating and underlying steel substrate becomes extremely important. Normally, a surface is investigated before and after reaction to study the differences in chemical composition or functionality. However, a bare or unreacted surface does not usually have the desired characteristics that are generally required for future applications. For example, in

protective-coating applications, a soft substrate may be exposed to an abrasive or high-pressure environment that would result in the failure of the component [56, 57]. A hard protective coating would be required to preserve the substrate for a longer period of time.

Depending on the desired coating and application, there are a number of methods that can be used to deposit the coatings. An important distinction can be made between depositing a thin film or coating in a vacuum environment and depositing a thin film or coating in an ambient atmospheric environment. Vacuum methods, which include physical vapor deposition (PVD) [52, 58] and chemical vapor deposition (CVD) [3, 52] and their derived methods (PVD: cathodic arc vapor deposition, magnetron sputtering; CVD: atomic layer deposition, microwave plasma-assisted CVD; and others), are all done under vacuum, high-vacuum, or ultra high-vacuum conditions. These coatings are characterized by high-purity films and uniform deposition depth, but are restricted by lack of depth, deposition efficiency, and long deposition time [59]. Each degree of ‘vacuumness’ has its own advantages and disadvantages. Some reasons for a vacuum environment include reduction in contaminants in deposited layer [60], increasing mean free path to reduce collision induced particle reaction [61], and provide fine-tuning for thin film or coating thickness and composition [62].

Both CVD and PVD methods are beneficial for applications in which the substrate is small and fits into a vacuum chamber. CVD can provide the most controlled conditions for deposition and thus the most flexibility in designing the appropriate interfaces. However, this method is difficult for producing films of tens of microns needed for certain application, in addition to requiring a vacuum. PVD can be

used to deposit thicker films at a faster rate; however, the control over the interface formation is more difficult, as the deposited films may suffer from delamination [63] and the method requires vacuum-based procedures. When a vacuum deposition is either geometrically or economically unfeasible (the tool or piece of machinery cannot fit into a vacuum chamber or to build one would be too costly), one must look to other methods performed at ambient conditions. These methods include high-velocity oxy/air-fuel (HV(O/A)F) [64, 65] and electrospark deposition/alloying (ESD) [66]. HV(O,A)F is an industry-wide technique that provides very dense, varying thickness coatings, minimal metallurgical changes, and minimal temperature effects (the entire material does not need to be heated) in the ambient environment. In an HV(O,A)F application, molten materials (the final coating) are shot out of a nozzle at supersonic speeds. It produces thick yet oxidized coatings very quickly, but it is very difficult to control the formation of the interface between the coating and the substrate, as the voids can easily form, which would lead to delamination and fracturing [67-69]. An electrospark deposited coating is another ambient air technique, but unlike HV(O/A)F, a metallurgical bond is built between the material and coating without post-treatment through chemicals or annealing [70]. Thus, in this case there should be no delamination. Like in HV(O/A)F, the substrate does not need to be heated, and the coatings can be applied with varying thickness. However, given the radial length of the electrode, deposition may take time.

In addition to the deposition method of the coating, the coating material itself is very important. For example, molybdenum disulfides are used for dry lubricants while another material, such as stainless steel, would be improperly used as a dry lubricant. An abrasive and wear-resistant coating that is also impervious to extreme

chemical conditions (e.g., very acidic or very basic conditions) is desired for extending tool and machine lifetime. Additional parameters (hardness, coefficient of thermal expansion, and modulus of elasticity) must have specific values when depositing onto a substrate that may physically change during operation. There has been great interest in carbide and nitride-based films for this specific purpose [52]. A number of studies have focused on a Ti(C,N)-based system as a titanium-based carbide possesses extraordinary hardness [71] while a titanium-based nitride exhibit extraordinary toughness [72]. Titanium carbonitride (TiCN) is amenable to deposition using a large number of methods that can be tailored to fit the potential application. Of course, other applications may require the final material to possess a specific set of physical and chemical properties. For example, conformal filling in microelectronics (that is, filling in the topography of the semiconductor substrate) may require slower, but more controlled, methods of coating based on chemical vapor deposition (CVD) [73-75]. On the other hand, substantially faster deposition rates, albeit with lower degree of control, could be achieved using physical vapor deposition to deposit the TiCN material [73, 74, 76-78]. It is important to realize that TiCN-based films are deposited using all these different methods (as well as the ESD mentioned previously), and continuous work on novel chemical deposition metalorganic precursors for chemical methods promises to deliver even higher variety of properties that can be introduced into the film.

Table 1.1 compares a common soft steel substrate (4000 series steel) with frequently deposited protective coatings (Ti(C,N)) coatings as well as the very common tungsten carbide (WC) coating. For the coating to perform according to the

application desired, some of its properties have to align perfectly with the properties of a desired substrate.

Table 1.1: Comparison of selected coatings with a common steel substrate.

<b>Compound</b>	<b>4000 Series Steel</b>	<b>Tungsten Carbide</b>	<b>Titanium Nitride</b>	<b>Titanium Carbide</b>	<b>Titanium Carbonitride</b>
Vickers Hardness, GPa	2.35	23.5	22.07	27.48	32.5
Coefficient of Thermal Expansion, $10^{-6} \text{ K}^{-1}$	10.4	5.2-7.3	7.4	7.95	9
Thermal Conductivity, $\text{W}/(\text{m}\cdot^{\circ}\text{C})$	42.7	42-84.2	19	17.1-30.9	31
Crystal Structure	BCC	Hexagonal	Cubic	Cubic	Tetragonal
Melting Point, $^{\circ}\text{C}$	1400-1538	2800-2870	2930	3065	3050
Modulus of Elasticity, GPa	210	669-696	500	430	473

In addition to increased hardness, a Ti(C,N)-based coating has to have some properties that are similar to stainless steel, such as coefficient of thermal expansion for processing and reliable high-temperature performance (which is often the case for long-term use tools). TiCN fits that requirement perfectly, because it possesses a very high hardness, even compared to the materials that are commonly thought of as hard coatings, such as TiN or TiC. In fact, TiCN also possesses a coefficient of thermal expansion and thermal conductivity very close to those for 4140 steel, meaning that mechanical changes caused by heating should affect these two materials in a similar way. This combination of properties and the multitude of available deposition methods make a TiCN coating such an attractive coating for tool protection purposes. When building the diffusion barriers for microelectronics, TiCN coatings are deposited from a common CVD chemical precursor, tetrakis(dimethylamido)titanium (TDMAT). However, there have been no literature studies to examine the mechanical and tribological properties of films deposited with this precursor and deposition method.

These must be examined to expand the applications for this method. Concurrently, because CVD is normally performed in vacuum, if the substrate's geometry is not conducive to a vacuum system, an alternative approach must be used for the ambient environment and more straightforward practical applications. To address this concern, an electrospark deposited coating was used to compare with the CVD deposited films.

#### **1.4 Novel Wet-Chemical Deposition of Nanoparticles**

One way to produce coatings for protective applications is to chemically attach the coating to a substrate. If an otherwise adequate coating (high hardness, high abrasion resistance, etc.) is not chemically attached to a substrate, there is the possibility of failure, either through delamination or spalling. One way to circumvent this problem is to chemically attach parts of the surface and deposit a different coating around the deposited layer. This procedure is analogous to rebar in concrete, where the rebar gives structural support to the concrete.

A very well known approach to chemically attach two different molecules together is through "click chemistry". In a very well known type of "click chemistry", an azide and an alkyne chemically react in the presence of a copper catalyst to form a triazole ring. Previously, we have shown a morphological change in iron nanoparticles after "click chemistry" [79]. We explained as due to the fact that after iron nanoparticle functionalization with azide or alkyne termination, the reaction takes place in a three-dimensional space and creates a new material. As a thought experiment, if alkyne functionalized nanoparticles were to react with an azide-functionalized surface in the presence of the copper catalyst, and then further with correspondingly opposite nanoparticles, one may achieve layer-by-layer (LbL) growth through click chemistry.

Layered structures have been a target of intense research for many decades. For example, the ability to produce exceptional conformal filling over the high aspect ratio features needed in microelectronics has been based on the formation of targeted strong chemical bonds in the course of atomic layer deposition (ALD) and the need for high-level control at the slightly larger scale for such applications as a photoresist formation or metalorganic layer growth has been realized in molecular layer deposition (MLD) processes. Both approaches utilize surface-limited reactions to form a layer of one atom to several atomic lengths thick that are perfectly suitable for a wide variety of applications. The main advantage of both methods is in atomic- and molecular-level precision of the multilayers created. One of the main disadvantages is that the growth rate and the size of the building elements are very limited.

At the same time, the layered materials with structural fragments of nanometers to tens of nanometers in size are needed for applications such as spintronics, specifically tunnel magnetoresistance [80], heterogeneous catalysis [81, 82], magnetic materials [83, 84], solar energy conversion with photoelectrochemical cells [85, 86] and many more. The formation of such films and materials using lithography or ALD and MLD methods is a very complex and expensive task.

If one were able to deposit the nanoparticles in a LbL growth with chemical attachment to a surface followed by a vapour deposition of a hard coating, we would have something that is very similar to rebar in concrete. This material would also have applications for protective coatings that need to also be chemically active.

However, as ideal as this system would be, the first step is to show high coverage following the click reaction between the nanoparticles and the substrate,

which has not been shown before. Once this is shown, the deposition of conformal coatings can commence.

## **1.5 Scope and Outline of the Dissertation**

The main focus of this dissertation is the development of thin films and coatings for targeted applications, in addition to understanding their chemical, structural, and, in some cases, their mechanical properties. It is important to focus fundamental research on real-world applications to enhance future breakthroughs.

Chapter 1 provides broad background on thin films and coatings for photovoltaic and protective coatings applications, and is expanded upon more in depth in further chapters. A description of the chemicals and materials used throughout the dissertation are discussed in Chapter 2 along with outlining the experimental methods used to adequately characterize the systems. After this, three projects are discussed in full detail. In Chapter 3, molecular attachment of a fullerene derivative to an amino-terminated surface is discussed with reference to the chemistry involved and future directions. In the next two chapters (Chapter 4-5), a protective coating is deposited by different methods onto a substrate to interrogate the chemical and mechanical properties of the coatings. In the final project (Chapter 6), a novel approach to chemically attaching nanoparticles is developed using layer-by-layer growth. The final chapter (Chapters 7) provides overarching conclusions as well as future work.

## Chapter 2

### EXPERIMENTAL PROCEDURES AND INSTRUMENTATION

#### 2.1 Introduction

The following sections describe the chemical preparation for each of the subsequent chapters in this thesis. Section 2.2.1 describes the methodology in Chapter 3. Section 2.2.2 is the experimental procedure for Chapter 4 while Chapter 5's method is described in section 2.2.3. Chapter 6's experimental description is detailed in section 2.2.4. All chemicals used show the company of origin and purity.

The description of all analytical methods follows the experimental procedures in section 2.3. Following the instrumentation descriptions, the parameters for each experiment are listed.

#### 2.2 Chemicals Used and Preparation Procedures

##### 2.2.1 Monolayer Preparation of Amino-Terminated Si(111) Surface

Chapter 3 details the experiment with an amino-terminated silicon substrate and [6,6]-phenyl-C<sub>61</sub>-butyric acid methyl ester (PCBM). A hydrogen-terminated Si(111) surface was prepared using a modified RCA (Radio Corporation of America) cleaning cycle [44]. All reactions were performed with Teflon beakers and tweezers, and the samples rinsed with Milli-Q water (18 M $\Omega$  · cm) between the steps. The Teflon beakers and tweezers were cleaned in a 4:1:1 solution of Milli-Q water, ammonium hydroxide (Fisher, 29% certified ACS plus grade), and hydrogen peroxide (Fisher,

30% certified ACS grade) (SC1 solution) for 30 min at 80°C while bubble rinsed with N<sub>2</sub>. The Si(111) wafers (Virginia Semiconductor, VA, double polished, n-doped, 500 um thick, >0.1 Ωcm resistivity) were cleaned with SC1 solution for 10 min at 80°C. The wafers were placed in an HF acid-buffer solution (Transene Company, Inc.) for 2 min at room temperature. Finally, the wafers were placed in a 4:1:1 water, hydrochloric acid (Fisher, 37.3% certified ACS grade), and hydrogen peroxide solution (SC2) for 10 min at 80°C. At this point, one wafer was removed to be the referencing spectrum for selected background infrared spectra. The rest of the wafers were placed in the HF acid buffer solution (Transene Company, Inc.) for 1 min at room temperature and then immediately placed in ammonia fluoride solution (Fluka, 40%) for 6 min at room temperature to form a well-ordered hydrogen-terminated Si(111) surface, as confirmed by a sharp single absorption peak at 2083 cm<sup>-1</sup> in the infrared spectra [87-91].

The H-terminated silicon wafers obtained as described above were placed in deoxygenated *tert*-butyloxycarbonyl (*t*-BOC) protected 1-amino-10-undecene (prepared from 1-amino-10-undecene (AUD), GFS, 97%) [92, 93] under nitrogen in a 25 mL round-bottom flask with a reflux condenser with running cold water. The flask was placed in an oil bath at 110°C. This reaction was conducted under reflux conditions for 2 hrs. The modified wafers were removed and cleaned with petroleum ether (40-60°C, (Fisher, Certified ACS), methanol (Fisher, 99.9%), dichloromethane (Fisher, 99.9%), Milli-Q water, and dried with N<sub>2</sub>. The resulting self-assembled monolayer (SAM) was deprotected with trifluoroacetic acid (Aldrich, 99%) and NH<sub>4</sub>OH, and then cleaned with Milli-Q water before further modification with PCBM.

The silicon wafer modified with the AUD SAM was placed in a 1 mM PCBM (Nano-C, 99.5%) in toluene solution (Fisher, 99.9%) in a 25 mL round bottom flask for either 3 hours or 5 hours, as indicated in the results, for the monolayer formation. The solution was held at reflux temperature (110°C) under N<sub>2</sub>. The resulting sample was cleaned with pure toluene (Fisher, 99.9%) and immediately characterized by appropriate analytical techniques.

To prove that the reaction proceeded as predicted and to provide necessary spectroscopic benchmarks, an analogous experiment for a 1:1 ratio of unprotected 1-amino-10-undecene (GFS, 97%) and PCBM in toluene was conducted under N<sub>2</sub>. The product of this reaction was used in infrared and mass spectroscopic studies to compare to that for the modified silicon wafer.

### **2.2.2 TDMAT Chemical Vapor Deposition Procedure**

In Chapter 4, a CVD precursor was used to deposit a titanium carbonitride (TiCN) coating. The deposition of TiCN was carried out on 4140-series steel discs. The 4140 series steel contains: 0.38-0.43% C, 0.15-30% Si, 0.80-1.10% Cr, 0.75-1.0% Mn, 0.15-0.25% Mo, <0.040% S, <0.035% P, and the balance Fe (all by weight) [94]. The first set of experiments was performed under ultra-high vacuum (UHV) conditions on an instrument with a base pressure of  $7.5 \times 10^{-10}$  torr. A 12-mm diameter steel disc was cut from a larger steel block with a thickness of 1 mm that was then polished and cleaned with ethanol and acetone. Immediately after cleaning, the disc was placed into the UHV chamber. The disc further underwent cleaning cycles of Ar<sup>+</sup> sputtering ( $3.0 \times 10^{-5}$  torr, 2 keV, 30 min, Ar (Product Grade, Matheson Tri-Gas)) and annealing to a temperature of 600 K. Auger electron spectroscopy was used to determine the cleanliness of the steel surface. Tetrakis(dimethylamido)titanium

(TDMAT, 99.99%, Acros Organics) was cleaned using three freeze-pump-thaw cycles before introduction into the ultra-high vacuum (UHV) chamber using a leak-valve. The steel disc was dosed with 30,000 L of TDMAT (where 1L =  $1 \times 10^{-6}$  torr · sec).

The rest of the experiments were conducted in a high-vacuum instrument at the (base pressure  $<1.0 \times 10^{-5}$  torr). Again, 12-mm diameter steel discs were used for deposition. Before introduction into the chamber, ethanol and acetone were used to clean the steel surface, and because this chamber was neither equipped with an ion sputter nor an Auger spectrometer, no further preparation procedures were performed. Deposition of TDMAT was done at 600 K by a 30,000 L dose.

### **2.2.3 Electrospray Deposition of TiCN and WC coatings**

Chapter 5 described an electrospray deposited (ESD) TiCN coating. ESD-deposited coatings were produced on 4140 series steel coupons. This is the same 4140-series steel used in the previous section. The coupons were 0.5 inches x 1 inch x 0.25 inches. The deposition was performed by Advanced Surfaces and Processes, Inc. (Cornelius, OR) with a 3<sup>rd</sup> generation electrospray deposition technique (NanoFusion™). Although the NanoFusion™ technique should not be confused with previous generations of electrospray deposition, we use the term electrospray deposition (ESD) interchangeably for simplicity's sake. Tungsten carbide (WC) was deposited from a precursor electrode available at Advanced Surfaces and Processes, Inc. To deposit TiCN, an appropriate TiCN electrode was custom made by Kyocera, Inc. (Kyoto, Japan). This sample was a 4-inch long, 3/16-inch in radius TiCN cermet rod. Deposition of both coatings has been performed at the same set of proprietary process parameters.

Before the coupons were sent for deposition, they were polished to remove dirt and cleaned with acetone and ethanol. No further cleaning or annealing was performed before deposition. A single deposition pass coated the samples with a 15 – 25  $\mu\text{m}$  of coating measured from the surface to interface. Following deposition, the coupons were cut (or polished for cross-sectional SEM studies) to fit into the various instruments.

#### **2.2.4 Nanoparticle Layer-by-Layer Growth**

In Chapter 6, a nanoparticle layer-by-layer (LbL) deposition method is interrogated. Prefabricated gold substrates (1000 Å gold thickness on silicon wafer support with titanium adhesion layer, Sigma Aldrich) were cleaned by immersing the substrate into piranha solution (1:3 hydrogen peroxide (30%, Fisher Scientific):concentrated sulfuric acid (98%, Fisher Scientific) for 5 min followed by immersion in Milli-Q water (18 M $\Omega$ ·cm) for 5 min. The substrate was then washed with HCl 37%, Fisher Scientific), water, ethanol, and then dried under a flow of N<sub>2</sub> gas. The clean Au substrate was immersed into 1 mM solution of 11-azido-undecanethiol (96%, Krackeler Scientific, Inc.) in ethanol for 24-36 hours in the dark to produce the azide-terminated monolayer on Au substrate [95]. The surface was then washed with ethanol, methylene chloride, and water, and dried under a flow of nitrogen gas.

Surface functionalization of 80-nm silica nanoparticles (dried, NanoComposix) to prepare alkyne functional groups was based on a previously published procedure [96]. 218  $\mu\text{L}$  of tetramethyl orthosilicate (98%, Sigma-Aldrich) and 218  $\mu\text{L}$  of 4-pentyn-1-ol (97%, Sigma-Aldrich) were dissolved in 10 mL of toluene. The resulting solution was stirred at room temperature for 24 hours. The 80-nm silica nanoparticles

were dispersed into 2 mL of toluene and added to the solution. The mixture was stirred at 80°C for 24 hours to form the alkyne-terminated silica nanoparticles. The resulting nanoparticles were washed in methanol five times followed by dispersion into methanol for further use.

The 50-nm silica nanoparticles (10mg/mL, dispersed in water, NanoComposix) exchanged solvents by dispersion in a series of ethanol/water mixtures (1:1, 3:2, 1:0 and 1:0) [97], so that the solvent could be changed from water to ethanol. The solvent was then exchanged to toluene by a series of toluene/ethanol solvents (1:1, 3:2, 1:0 and 1:0) to produce 50-nm silica nanoparticles dispersed in toluene. The azido-termination was performed similarly to that for alkyne-terminated silica nanoparticles. 218  $\mu$ L of tetramethyl orthosilicate and 36  $\mu$ L of 2-azidoethanol (95%, MolPort) were dissolved into 10 mL of toluene. The resulting solution was stirred in 80°C for 24 hours and used without further purification. The 50-nm of silica nanoparticles were dispersed into 2 mL of toluene and added to the solution. The mixture was then stirred and refluxed for 24 hours to form the azide-terminated silica nanoparticles. The resulting nanoparticles were then washed in methanol five times followed by dispersion into methanol for further use.

The gold substrate was immersed into 4:1 methanol:water (by volume) with 3 mg/mL 80-nm of alkyne-terminated silica nanoparticles. Catalytic amounts of copper sulfate pentahydrate (Fisher Scientific) and sodium ascorbate (Fisher Scientific) were added to the system. The mixture was then sonicated for 24 hours, followed by washing with ethanol, methylene chloride, and ethanol, and further sonicated for 30 min in ethanol to remove physically adsorbed nanoparticles.

The gold substrate modified with the first layer of 80 nm silica nanoparticles with alkyne functional group was incubated with a drop of azide-terminated 50-nm silica nanoparticles in 4:1 methanol:water (by volume) solvent until dry. The sample was rinsed with ethanol, methylene chloride, ethanol, and further sonicated for 30 min in ethanol to remove the physically adsorbed nanoparticles.

The resulting triple layer of nanoparticles on the gold wafer was covered with a drop of alkyne-terminated 80-nm silica nanoparticles 4:1 methanol:water (by volume) with trace amount of copper sulfate pentahydrate and sodium ascorbate catalysts until dry. The sample was then rinsed with ethanol, dichloromethane, ethanol and sonicated for 30 min in ethanol to remove the physically adsorbed nanoparticles.

## **2.3 Instrumentation Used and Theory**

### **2.3.1 X-ray Photoelectron Spectroscopy**

X-ray photoelectron spectroscopy (XPS, also known as electron spectroscopy for chemical analysis, ESCA) is a surface science technique to explore surface chemical and oxidation states. Performed under UHV conditions, XPS is commonly used to probe the top 1-5 nm of the surface, and can detect all elements with an atomic number of 3 and above. During sample collection, energy in the form of X-rays is emitted from a source (usually Al or Mg) towards the surface focusing on an area a few hundred square microns in size. When the X-rays hit the surface, electrons are emitted at the X-ray energies that correspond to the individual electron's binding energy. An electron's binding energy is directly correlated to the electron configuration in the atom; that is, electrons in the outmost shell are weakly bound

(~30 eV for W 4*f*, for example) whereas the innermost atom electrons are much more strongly bound (~593 eV for W 4*s*).

During collection of electrons by the detector, a spectrum of binding energy versus electron counts can be plotted. To compare the relative atomic concentrations on the sample surface, one must divide the peak area by the elements relative sensitivity factor, which can vary greatly depending on the X-ray source used.

In addition to an electron's elemental and energy level, the binding energy is greatly influenced by the oxidation state of the atom (known as the *chemical shift*). Electrons from oxidized atoms tend to shift to a higher binding energy while reduced atom's electrons tend to a lower binding energy. This fact is very important when assigning peaks to chemical bond species. In the studies of TiCN in Chapters 4 and 5, for example, in the Ti 2*p* region, the oxidized titanium peak is located at a higher binding energy than the carbide or nitride titanium peak. XPS instrumentation is a powerful tool when characterizing a surface.

In all experiments (Chapters 3-6), the XPS spectra were collected on a PHI 5600 X-ray Photoelectron Spectrometer with an Al K $\alpha$  X-ray source ( $h\nu=1486.6$  eV) at a 45° take-off angle. The measurements were performed in a vacuum chamber with a base pressure of  $1 \times 10^{-9}$  Torr. Before spectra taken in Chapter 4 (CVD TiCN deposition), argon sputtering (3 kV, 30 seconds) was used to remove any contaminants adsorbed on a surface while transferring the samples from one instrument to another. Survey spectra were collected from 0 to 1000 eV binding energy. High-resolution spectra were collected with a pass energy ranging from 20 to 30 eV and an energy resolution of 0.1 eV. In Chapters 3, 5, and 6, 15 to 20 passes per cycle were taken. In Chapter 4, 1-5 passes per cycle were taken. The C 1*s* peak at 284.6 eV was used to

calibrate the spectra in Chapter 3-5. In Chapter 6, the Au  $4f_{7/2}$  peak at 83.8 eV (which corresponds to 284.6 eV for the C  $1s$  spectrum) was used to calibrate. Data processing and peak fitting were performed using CasaXPS software. It must be noted that fitting XPS data is highly suggestive. All peaks fitted in this thesis come from the basis that what we one expects to be present in the sample.

### 2.3.2 Auger Electron Spectroscopy

Auger electron spectroscopy (AES) is a process very similar to XPS. While slightly less robust, AES still is useful in determining elemental composition. AES measures Auger electrons in lieu of core electrons emitted by X-ray collisions. When an X-ray collides with a core electron in an atom, and, if the energy is sufficiently high to eject the electron, the core electron is emitted while leaving a hole in the electron level (which is the basis for XPS). An outer-shell-level electron may fill the inner electron shell, and the transition energy is imparted to an outer shell electron and that electron is ejected. The Auger electron process is a three-electron process and occurs independently of the photoemission process (XPS).

Just like XPS, the Auger process is performed under ultra high vacuum conditions and the Auger electrons emitted are normally between 50 eV and 3000 eV. The Auger spectrum is not normally plotted as energy versus Auger electron counts; it is plotted as energy versus the derivative of Auger electron counts over energy. The relative concentrations for the elemental composition of the sample are determined by comparing the peak intensities and relative sensitivity factors, which is seen in Equation 1.

$$C_A = \frac{I_A/S_A}{I_A/S_A + I_B/S_B + I_C/S_C + \dots} \quad \text{Equation 2.1}$$

In Equation 2.1,  $C_A$  is the relative concentration of species  $A$ ,  $I_A$  is the peak intensity of species  $A$  (in any arbitrary units), and  $S_A$  is the relative sensitivity factor for species  $A$  (which can be found in pregenerated tables). Symbols with subscripts  $B$  and  $C$  correspond to species  $B$  and  $C$ . Auger electron spectroscopy is an essential surface analytical tool, especially for coating and thin film growth performed under UHV.

In Chapter 4, for samples prepared in UHV conditions, the surface composition was determined using a single-pass Auger electron spectrometer (STAIB Instruments).

### 2.3.3 Fourier Transform Infrared Spectroscopy

Infrared spectroscopy uses light in the infrared region of the electromagnetic spectrum to obtain information on the chemical species present in a sample. The infrared region is light that has a longer wavelength and lower frequency than red light (hence infra, “below, further on”). As the light sweeps through the range one wishes to measure, a detector records the intensity of light being transmitted through the sample. Molecular bonds in the sample absorb light that correlates to the energy of the bond, which is known as the resonance frequency. As the bonds absorb the light, the amount of light reaching the detector decreases. When compared to the background spectrum, a peak is discerned. Some molecular bonds produce a strong peak and other bonds produce a weak peak. The intensity of the peak is related to how large the change in dipole moment is for that vibrational mode (in addition to how much of the molecular bond is present in the sample). There are  $3N-5$  degrees of vibrational modes for linear molecules and  $3N-6$  vibrational modes for non-linear molecules, where  $N$  is the number of atoms in the molecule. In an organic molecule, there are 6 common vibrational modes, which are shown in Figure 2.1 (although it must be stressed that the

molecules with additional molecules are more complex; the depictions here are of a special representative material).

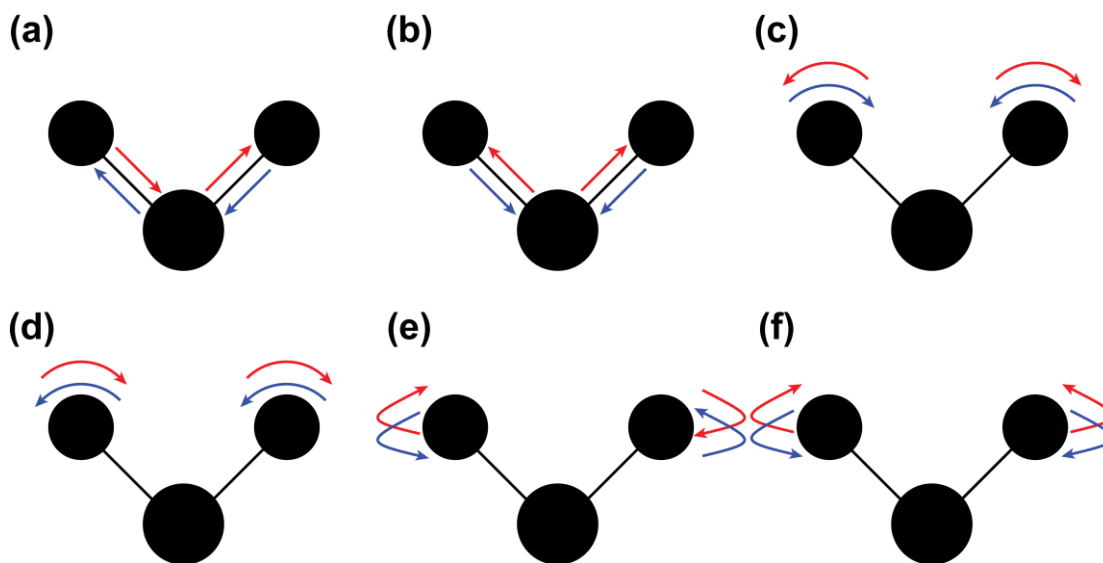


Figure 2.1: Common vibration modes in an organic molecule. They are (a) asymmetrical, (b) symmetrical, (c) scissoring, (d) rocking, (e) twisting, and (f) wagging. The blue and red lines indicate the direction of atom movement. The direction indicated alternates between red and blue.

Originally, the method of collection for IR spectroscopy involved transmitting light and scanning the range by utilizing a monochromator. However, because of long detection times, a mathematical transformation is often used to speed up the process. In Fourier transform infrared spectroscopy (FT-IR), the infrared light is passed through an interferometer. The interferometer splits the light beam into two where one half reaches the detector without passing through the sample while the other half passes through the sample. The combined light produces an interferogram detected optically and a Fourier transform is applied to produce the sample spectrum.

In some cases, a single-transmission pass does not contain enough signal for adequate sample analysis. In these cases, a technique known as attenuated total reflectance (ATR) can be used to examine solid or liquid states. The infrared beam passes through a crystal and reflects at least once off the surface that is in contact with the sample. Depending on the wavelength, refractive index, incidence angle, and both media, the penetration depth is at maximum 2 microns. When the signal bounces multiple times, the signal-to-noise ratio is very high.

In Chapter 3, single transmission FT-IR measurements were performed on a Nicolet Magna 560 spectrometer using a liquid nitrogen-cooled MCT detector. The silicon sample was placed at a  $57^\circ$  angle with respect to the incoming beam. The spectra were collected within the  $4000\text{-}650\text{ cm}^{-1}$  range at a resolution of  $8\text{ cm}^{-1}$  and 512 scans per spectrum. Presented in the chapter are the most informative regions of  $1600\text{-}1800\text{ cm}^{-1}$  and  $2700\text{-}3200\text{ cm}^{-1}$ , which show C=O stretch region and C-H stretch regions, respectively. An AUD-terminated wafer was used as the background for PCBM spectrum. For the parallel PCBM-AUD powder experiment, both PCBM and AUD-PCBM were mixed with KBr and the pure KBr pellet was used as a background. In Chapter 6, single point attenuated total reflectance Fourier transform infrared (ATR FT-IR) spectroscopy measurements were performed on a Bruker Optics (Billerica, MA) Vertex 70 FT-IR with a Bruker Hyperion 2000 Microscope attachment and liquid nitrogen cooled MCT detector. The Hyperion microscope is equipped with a dedicated single-point ATR attachment with a Germanium crystal tip for surface analysis. Each spectrum was produced from 256 scans at a resolution of  $4\text{ cm}^{-1}$ , and with a spectral range from  $4000\text{ cm}^{-1}$  to  $600\text{ cm}^{-1}$ . The functionalized surfaces and

nanoparticle deposited surfaces were referenced against a gold surface sonically cleaned in ethanol.

### **2.3.4 Atomic Force Microscopy**

Atomic force microscopy (AFM) is a surface topographical technique that uses a feedback system to investigate a surface. Performed under ambient to vacuum conditions, laser light is emitted onto a cantilever with a tip on one end. Ideally the tip is a few nm in width, but after a few scans, the tip tends to become more blunt (which would then reduce spatial resolution). To increase resolution, the cantilever is sometimes coated with a highly reflective metal such as Al. After the surface hits the tip and moves the cantilever, the laser is reflected into a photodiode. The photodiode is connected to a detector and feedback system to analyze the results as well as protect the tip. As the sample is scanned, topographical information is recorded.

During the recording process, the cantilever stays in a stationary position. The sample is the piece that is moving, and this is done with the piezoelectric effect. The piezoelectric effect is the small change in physical structure as electricity is passed through. Likewise, a mechanical stress can record an electric charge, but this method is not currently used in AFM analysis. The piezoelectric effect can be directed in the  $x$ -,  $y$ -, and  $z$ - directions.

In Chapters 3 and 4, AFM imaging was performed in a tapping mode on a Veeco Multimode SPM with a Nanoscope V controller while in Chapter 5 and 6, the AFM measurements were performed on a Veeco Multimode SPM with a Nanoscope Dimension 3100 controller. Budget Sensors' BS-Tap 300Al tips (monolithic silicon with reflective Al coating to enhance sensitivity) with a force constant of 40 N/m and a drive frequency of 300 kHz were used. The AFM images were collected at 512

pixels x 512 pixels (with varying width), and the spectra were analyzed using Gwyddion software [98].

### **2.3.5 Time of Flight Secondary Ion Mass Spectroscopy**

Time-of-flight secondary ion mass spectroscopy (ToF-SIMS) is a surface analytical technique that probes the surface by sputtering the surface with either a positive or negative primary ion beam and measuring the collected secondary ions. The collected data is analyzed in relation to the mass/charge ( $m/z$ ) of the molecular fragments (for organic molecules) or elemental species. Performed under UHV conditions, a variety of primary beams are used depending on the nature of the substrate and the desired peaks to analyze. After the primary beam impacts the surface and ejects material, lighter elements and fragments travel to the detector quicker than heavier fragments and elements. The spectrum is calibrated against known peaks. The data range is essentially limitless if there is enough signal for higher  $m/z$  ratios.

There are two different modes for ToF-SIMS analysis: the static mode and the dynamic mode. In the static mode, the top most layer is examined without regard to depth. Normally, the surface is analyzed with a negative primary beam and followed by a positive primary beam, or vice versa. The subsequent peaks are analyzed to observe what is present on the surface. In contrast, the dynamic mode deals with the bulk analysis (i.e. depth) of the sample. Depending on how long one wants to wait to analyze the surface, the depth can be limitless as well. A third beam is used to sputter away what is present on the surface very slowly. After each sputtering cycle, the secondary ions are analyzed through the detector. The cross-sectional analysis can then be determined by the successive set of measurements. It must be stated that one cannot compare different materials on the same scale; some materials are more easily

ionizable than others. However, one can compare the relative concentrations along the depth to see when the concentrations increase or decrease. Because of the robust applications of ToF-SIMS, this technique is an important tool in surface analysis.

In Chapter 3, ToF-SIMS measurements in a static mode were performed with a ToF-SIMS V spectrometer (ION-TOF, Münster, Germany) while in Chapter 4, a depth profile was determined from time-of-flight secondary-ion-mass-spectrometer in the dynamic mode. The measurements reported in Chapter 3 were analyzed in the high-current bunched mode with 25 keV  $\text{Bi}_3^+$  primary ions, a target current of 0.27 pA, and a beam dosage of  $10^{12}$  ions/cm<sup>2</sup> to spotter the surface. The ToF analyzer had a 2 kV extraction energy with 10 kV post-acceleration energy. The analyses in both chapters have a mass resolution of  $m/\Delta m=6000$  for  $\text{SiH}^+$ . The calibration masses were  $\text{H}^+$ ,  $\text{H}_2^+$ ,  $\text{H}_3^+$ ,  $\text{C}^+$ ,  $\text{CH}^+$ ,  $\text{CH}_2^+$ ,  $\text{CH}_3^+$ ,  $\text{C}_2\text{H}_3^+$ ,  $\text{C}_3\text{H}_5^+$ ,  $\text{C}_4\text{H}_7^+$ ,  $\text{C}_5\text{H}_5^+$ ,  $\text{C}_6\text{H}_5^+$ , and  $\text{C}_7\text{H}_7^+$  in positive mode, and  $\text{H}^-$ ,  $\text{C}^-$ ,  $\text{CH}^-$ ,  $\text{CH}_2^-$ ,  $\text{CH}_3^-$ ,  $\text{C}_2^-$ ,  $\text{C}_2\text{H}^-$ ,  $\text{C}_3^-$ ,  $\text{C}_4^-$ ,  $\text{C}_5^-$ ,  $\text{C}_6^-$ ,  $\text{C}_7^-$ , and  $\text{C}_8^-$  in negative mode. Additionally, for the samples that contained the PCBM molecule in Chapter 3,  $\text{C}_{60}^-$  was used to calibrate the higher mass fragments in negative mode. The silicon wafer experiments, molecular PCBM, and the analogous AUD-PCBM sample were investigated in positive and negative modes; however only the negative modes are presented in Chapter 3 because they contain all the necessary information. Each spectrum in Chapter 3 was calibrated against the  $\text{CO}_2$  count to produce normalized results.

### **2.3.6 Scanning Electron Microscopy, Energy-dispersive X-ray Spectroscopy, Focused Ion Beam**

Scanning electron microscopy (SEM) allows high-magnification images of surface topography and composition. Analogous to optical microscopes where light is

used to examine samples, an electron beam is used for high-resolution images. Normally examined under high vacuum, images can also be taken in low vacuum or environmental conditions. The most common imaging technique is the detection of secondary ions excited by a primary incident beam of electrons. Different detectors provide different levels of analysis. In-lens detection caused by inelastic scattering of electrons, for example, provides a high lateral resolution of elements near the surface of the specimen while a backscatter electron detector caused by elastic scattering of electrons provides high resolution of electrons emitted from much deeper in the sample.

If a sample under analysis is insulating or a semiconductor, it is normally coated with a thin layer of electrical conducting material (normally carbon or platinum). However, there are other ways around this problem, which include either reducing the working distance or the energy of the incident electron beam.

A technique often used in conjunction with SEM analysis is energy-dispersive X-ray spectroscopy (EDX, EDS, XEDS). EDX analysis is used for elemental analysis rather than chemical state analysis. Very similar to XPS analysis, a high-energy beam of electrons probes the sample and an electron from an inner shell is emitted. An electron fills this hole, and the difference in energy between the higher and lower energies is emitted in the form of X-rays. These X-rays are analyzed to determine which chemical species are present in the sample. If the energy of the incident electrons is not sufficient to produce energy high enough for characterization, there is a possibility of incorrect attribution. For example, the characteristic Si peak is located at 1.739 kV. If the incident electron beam is not strong enough, it may be confused with a W peak at 1.774 kV. To reduce the possibility of incorrect attribution, sufficient

incident energy is needed because there is another W peak at 8.396 keV. Multiple modes are available for this technique as well. One technique is the spot mode, where a EDX beam is focused onto a narrow spot and the X-rays are measured. Another is a line EDX, where the EDX beam rasters along a long, and relative intensities along the line are measured. One final technique is the map mode, where the EDX spot rasters along the entire image. The EDX technique is very useful when determining elemental analysis during scanning electron microscopy.

One additional technique often used with SEM analysis is utilization of a focused ion beam (FIB). A FIB uses a primary beam to sputter away a surface. This process is highly controllable and is used to fabricate highly intricate patterns with precise depth. This method can also be used to image the surface, but uses ions instead of electrons. This method was used to polish samples to examine the cross-sectional areas of different materials. The FIB/SEM system was also used to fabricate transmission electron lamellas.

In Chapters 5 and 6, a scanning electron microscope (Zeiss Auriga 60 FIB/SEM) was utilized to examine the morphology of the surface as well as cross-sections of coatings. The surface morphology images were collected by secondary electrons (in-lens detector) with an accelerating energy of either 20 keV (Chapter 5) or 3 keV (Chapter 6), and a working distance of 5.0 mm. In Chapter 5, to examine the interface between the coatings and the substrates, one side of each sample was polished with 420- and 600-grit sand paper under water. The samples were polished with a gallium FIB with a 20 nA current, and then finely polished with 4 nA and 2 nA currents. The samples were then removed from the chamber, flipped onto the side that was not polished, and placed back into the chamber. A line profile energy-dispersive

X-ray spectroscopy (EDX) procedure was used to follow elemental composition through the interface between the coating and the steel coupon substrate. In Chapter 6, to investigate the nanoparticle layer thickness, the gallium FIB was used to etch away nanoparticles. The gallium beam had an energy of 30 kV and a current of 120 pA. The polished samples were then placed at a 65° angle (which is the limit of the SEM/FIB stage), and images were taken.

### **2.3.7 Transmission Electron Microscopy**

Transmission electron microscopy (TEM) is a technique that is similar to SEM analysis but uses a beam of electrons transmitted through a thin (~10 nm) specimen. The electrons then interact with the specimen to form an image. The TEM technique is capable of much higher resolution (atomic scale). In the case of studies in the thesis, the TEM electron source is a tungsten filament, although in other instances a LaB<sub>6</sub> source is used. The electron beam is focused and condensed through the column to produce a highly focused electron beam. Both elastic scattering and inelastic scattering are present in the detection with elastic scattering resulting in no loss of energy while inelastic scattering produces a measureable loss of energy (important for EELS analysis, but not used in the thesis). As the atomic number increases, elastic scattering is more prevalent, and therefore, higher atomic number is associated with a brighter image.

In Chapters 4 and 5, a JEOL JEM-2010F FasTEM, operating at 20 KeV was used to interrogate the uniformity of the coating and the structure of the interface produced. The lamella for TEM experiments was prepared with the Auriga 60 FIB/SEM system (described in section 2.3.6).

### **2.3.8 X-ray Diffraction**

X-ray diffraction (XRD, or X-ray crystallography) is a bulk analysis technique that used to determine the atomic structure of crystalline materials. Incident X-rays are emitted into a sample, and the diffracted x-rays are collected at different angles. By measuring the peak positions and intensities, the three-dimensional structure of a material can be determined. If the X-rays do not interact with any atoms in the material, or the material is amorphous or noncrystalline, no peak is observed. In other words, if a coating is deposited onto a substrate, both the coating and the substrate produce different peaks without interaction (although they may overlap somewhat). The X-rays exhibit elastic scattering; that is the incident and outgoing beams are the same energy and wavelength. The only different is the direction of the X-rays.

In Chapter 5, the XRD measurements were conducted on the TiCN and WC ESD coatings as well as on the TiCN electrode. A Rigaku D/Max B x-ray diffractometer with Cu  $K\alpha$  radiation of a wavelength of 1.5418 Å was used in these studies. The scans were taken with a 2 s dwell time and a 0.02° step size. The current and voltage were 30 mA and 30 kV, respectively. To increase the signal-to-noise (S/N) ratio for thin films, a binomial smoothing algorithm was applied to selected results.

### **2.3.9 Mechanical NanoIndentation Characterization**

Tribological indentation is a useful tool for analyzing different mechanical properties. Because hardness is not always indicative of abrasion resistance (for example, a hard, brittle sample may break at first contact with an abrasive material), a more suitable mechanical property to investigate is Young's modulus. Young's modulus is the measure of the stiffness of the material. It is measured as the stress (the

force that continuous particles exert on each other) over the strain (the deformation after the strain of the displacement between the aforementioned stress). The Young's modulus can be measured in the linear portion of the stress-strain curve of a material.

It should be noted that obtaining Young's modulus is not as simple as reading measurements off an instrument. When reading the measurements from an instrument for a given depth, the Young's modulus values given do not normally take into account the Young's modulus of the tip (normally diamond), Young's modulus of the substrate, and Poisson's ratio of the tip, coating, and substrate. Additionally, surface effects influence values until  $5 \times R_{RMS}$  while substrate effects start to be felt at 20% of film thickness. For sufficiently thick and/or low roughness coatings, the range at which to take indentations is rather large, and no substrate effect calculations is required (one must still only use indentations at  $5R_{RMS}$ ). However, when the coating is thin with relatively high amount of roughness, one must take into account the substrate. Luckily, there are models that take into account each of the aforementioned parameters.

In Chapters 4 and 5, a Hysitron TI 900 TriboIndenter<sup>TM</sup> with a 50-nm (Chapter 4) or 150-nm (Chapter 5) diamond Berkovich tip was used to measure the Young's modulus of the steel substrate, TiCN and WC coatings. Before each indent, the piezoactuator stabilized for 60 s, and a drift correction was calculated for 40 s. The drift rate was calculated over the last 10 s. The tip approached the surface multiple times with different loads. The tip was loaded to a maximum force in 5 s, held constant at maximum load for 5 s, and unloaded in 5 s. These maximum loads ranged from 20  $\mu$ N to 2400  $\mu$ N. A total of twenty-seven indentations were taken for each coating, with all results from each trial being utilized to calculate the Young's

modulus. Eighteen indentations with maximum loads ranging from 200  $\mu\text{N}$  to 2400  $\mu\text{N}$  were performed on a 4140-series steel substrate to calculate its Young's modulus. The method used in the thesis to calculate the Young's modulus while taking into account substrate effects was described in detail by Tricoteaux et al.[99]

## Chapter 3

### ATTACHMENT CHEMISTRY OF PCBM TO A PRIMARY-AMINE-TERMINATED ORGANIC MONOLAYER ON A SI(111) SURFACE

#### 3.1 Abstract

In this chapter, a silicon surface modified with 1-amino-10-undecene was reacted with [6,6]-phenyl-C<sub>61</sub>-butyric acid methyl ester (PCBM) in toluene. Two possible competing reactions for PCBM, via the ester group and by a direct attachment to the C<sub>60</sub> portion, are analyzed. Various surface analytical techniques supplemented with density functional theory calculations were performed to adequately characterize the surface. Despite similarity of the energetics for those two reaction pathways, the predominant chemisorption occurs via the direct attachment of the C<sub>60</sub> cage to the functionalized silicon surface's primary amino-group. Adapted with permission from [100]. Copyright 2014 American Chemical Society.

#### 3.2 Introduction

Here, a [6,6]-phenyl-C<sub>61</sub>-butyric acid methyl ester (PCBM) molecule is attached to the aminofunctionalized surface. A PCBM molecule has a C<sub>60</sub> frame with a phenyl ring and carbon chain ester group, which is used to improve its solubility for practical applications [101, 102]. It is indeed commonly used in organic solar cells [103, 104]. Thus, the chemistry of this multifunctional molecule and its electronic properties must be understood with respect to all the functionalities involved. The reaction of PCBM with amines has not been evaluated in terms of the possible

reaction channels; however, there are several reports on amide-containing PCBM derivatives [105, 106]. Hummelen et al. [105] investigated an acid chloride reaction intermediate that was then reacted with histamine to form 1-(3-( $\omega$ -N-histaminocarbonyl)propyl)-1-phenyl[6,6]-C<sub>60</sub>. Liu et al. [106] showed that the amide-containing PCBM derivative was a result of the reaction between C<sub>60</sub> and t-butyl-5-(2-tosylhydrazano)pentamide. There are two types of functionalities available for the PCBM molecule suggesting that two completely different reaction pathways have to be considered in its attachment to an amino-functionalized surface. In one possible reaction, the PCBM would react with the surface primary amine via its ester group to form an amide [107]. In a similar reaction, Duevel and Corn [107] modified a gold surface with 11-mercaptopundecanoic acid and formed an amide after reaction through three different amines (hexylamine, benzylamine, and aniline). Even though the surface modified was a gold surface, the same chemistry and techniques apply. The second possible reaction has the PCBM reacting through the C<sub>60</sub> frame with the -NH<sub>2</sub> group on a surface [43, 108-110]. In Amelines-Sarria and Basiuk [108], the authors describe a theoretical approach to nucleophilic addition of multiple methylamine molecules. One primary task was to determine if the [6,6] bonds in a C<sub>60</sub> are always preferentially involved at every amination step, and it was found that the [6,6] bonds are indeed always preferential. This is important because one possible reaction pathway deals with reaction through the C<sub>60</sub>, and the fullerenes first reaction is with the phenyl ring and carbon chain ester group along one [6,6] bond. This suggests that additional reaction sites are preferential along the additional [6,6] bonds of the C<sub>60</sub>. Likewise, in Lin et al.[109], the authors study the reaction of methylamine with C<sub>50</sub>, C<sub>60</sub>, and single-walled nanotubes. The authors found that some reaction sites,

specifically the [6,6] bond of the C<sub>60</sub>, were exothermic in nature (-2.9 kcal/mol, 12.1 kJ/mol), especially when compared to the [5,6] bond (14.0 kcal/mol, 58.6 kJ/mol). However, because no studies have explored the reaction between an amine and the PCBM molecule, it is important to understand the reaction pathway when two competing chemistries are vying for the reactants.

### 3.3 Experimental Details

#### 3.3.1 Monolayer Preparation

The detailed procedure for SAM formation is found in section 2.2.1. A schematic diagram of this reaction is shown in Figure 3.1. Because the PCBM may react in two different ways with the deprotected AUD SAM, the two main possible products are referred to as **Structure 1** and **Structure 2**. These are shown in Figure 3.1. There is also the possibility that a single PCBM molecule may react with two separate AUD chains; or further, two different PCBM molecules may react differently with the surface. The modified surface would then be a mixture of both the **Structure 1** and **Structure 2**. It should be noted that **Structure 2** is only one representative structure produced by amine reaction with the C<sub>60</sub> cage, as explained in more detail further in section 3.4.5.

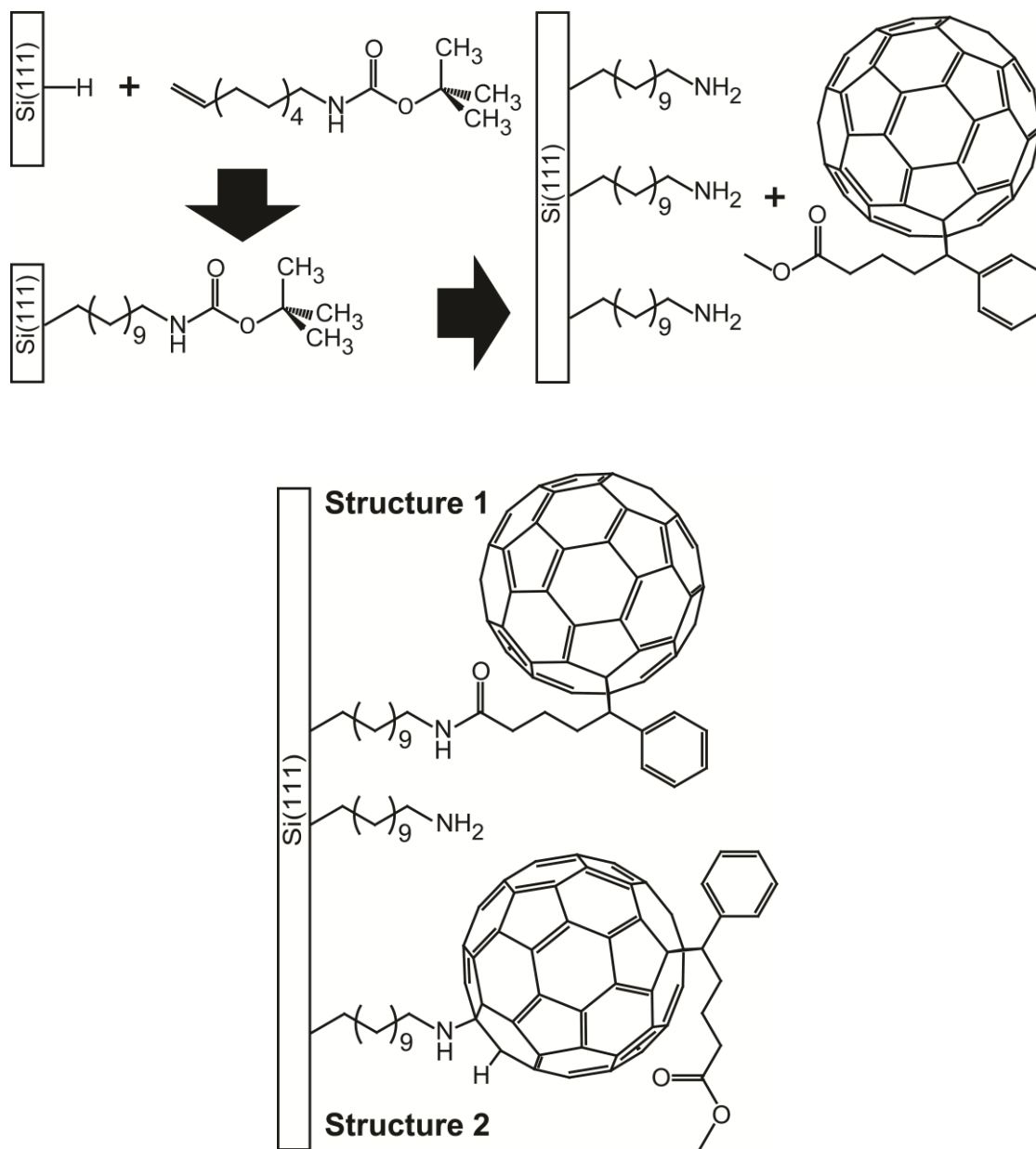


Figure 3.1: Schematic diagram of the chemical modification steps performed. A H-terminated Si(111) wafer is refluxed in *t*-BOC protected 1-amino-10-undecene under N<sub>2</sub> followed by deprotection in TFA and NH<sub>4</sub>OH. The deprotected AUD SAM is then exposed to the PCBM. The final product may be the result of the PCBM reacting through its ester functionality to form an amide with the SAM (**Structure 1**) or through its C<sub>60</sub> frame (**Structure 2**).

### 3.3.2 Surface Characterization

Each step of the chemical modification of Si(111) surface with PCBM is explored with X-ray photoelectron spectroscopy (XPS), atomic force microscopy (AFM), Fourier-transform infrared spectroscopy (FT-IR), and time-of-flight secondary ion mass spectroscopy (ToF-SIMS). Some of these experimental results are compared with and confirmed with the help of density functional theory (DFT) calculations.

### 3.3.3 Computational Details

Density functional theory calculations were used to complement experimental results. The Si(111) surface was represented by a  $\text{Si}_{10}\text{H}_{15}$  cluster. All silicon atoms except for those representing the surface were terminated with hydrogen atoms. The  $\text{Si}_{10}\text{H}_{15}$  cluster, PCBM molecule and 1-amino-10-undecene chain were optimized by the B3LYP functional [111-114] in the Gaussian 09 suite of programs [115]. Structure optimization, vibrational frequencies, and transition state predictions were calculated using the LANL2DZ basis set, and a scaling factor of 0.945 was applied to frequency results in the CH region, which is consistent with previous work [44, 116, 117]. This factor was obtained by comparing the predicted C-H stretching spectral region with the observed stretching region for known surface species. Results for the C=O stretch region are presented without additional scaling. To reduce computational time, the product of PCBM and 1-amino-10-undecene reaction without the  $\text{Si}_{10}\text{H}_{15}$  cluster was used for frequency calculations, and propylamine was used to determine the transition state energy instead of 1-amino-10-undecene tethered to the  $\text{Si}_{10}\text{H}_{15}$  cluster. The N 1s core-level energies of the samples were calculated using Koopmans' theorem. All of the B3LYP/LANL2DZ N 1s predicted core-level energies were adjusted by a

correction factor of 8.5 eV, which was determined previously [118-120]. The optimized DFT XYZ coordinates is found in Appendix A.

### 3.4 Results and Discussion

#### 3.4.1 Interrogation of the Monolayer Formation and PCBM Adsorption by XPS

The properties of the SAM on Si(111) wafer were investigated using XPS. The results for hydrogen-terminated silicon, deprotected 1-amino-10-undecene on silicon, and the PCBM-AUD monolayer on silicon are summarized in Figure 3.2. In Figures 3.2(a-c), the C 1s region of the three samples is presented. For the hydrogen terminated Si(111) surface (Figure 3.2(a)), only a very small peak at 284.6 eV appears. This peak corresponds to the adventitious carbonaceous material present in the atmosphere and likely deposited on the sample when it is briefly exposed to ambient conditions during the transfer into the XPS chamber. In Figure 3.2(b) for the AUD samples, three peaks are discerned. They are located at 284.6 eV, 286.6 eV, and 288.8 eV, and are assigned to the C-C bonds [121, 122], C-N/C-O bonds [49, 92], and C=O bonds [49, 92, 123], respectively. AUD has an alkyl chain, so having C-C bonds would be expected. Because it is the largest peak and corresponds to a well-known value, the peak location was used to calibrate all of the spectra for the same sample. The C-N/C-O peak originates from the C-N bond in AUD and the C-O bond may be from low concentration of *t*-BOC remaining on the AUD after deprotection [92]. The C=O peak is likely due to oxidation or adsorption of adventitious hydrocarbons that may occur during the sample transfer [92]. Figure 3.2(c) shows the C 1s region of the PCBM-terminated monolayer. Again, the peak at 284.6 eV, the signature of the C-C bonds, was used to calibrate the spectra. Much like in Figure 3.2(b), the peak at

286.6 eV was due to the C-O and C-N bonds, and the peak at 288.5 eV was due to the C=O peak. However, a new origin of these peaks can be suggested, in addition to any residual *t*-BOC protected AUD (C-O peak) and oxidation (C=O peak). PCBM has both of these in its structure. The increase in intensity of the 286.6 eV peak is consistent with the presence of the C-N and C-O containing functionalities caused by the PCBM adsorption; however, the real proof of the process is the presence of a peak at 291.6 eV, which corresponds to the  $\pi$ - $\pi^*$  shake-up in aromatic functional groups [121]. There are two possible sources of aromaticity in the sample: the C<sub>60</sub> and phenyl ring, both of which are found in the PCBM. Because this peak is not observed in the AUD sample, it is a strong indicator that there is PCBM present on the surface of this sample.

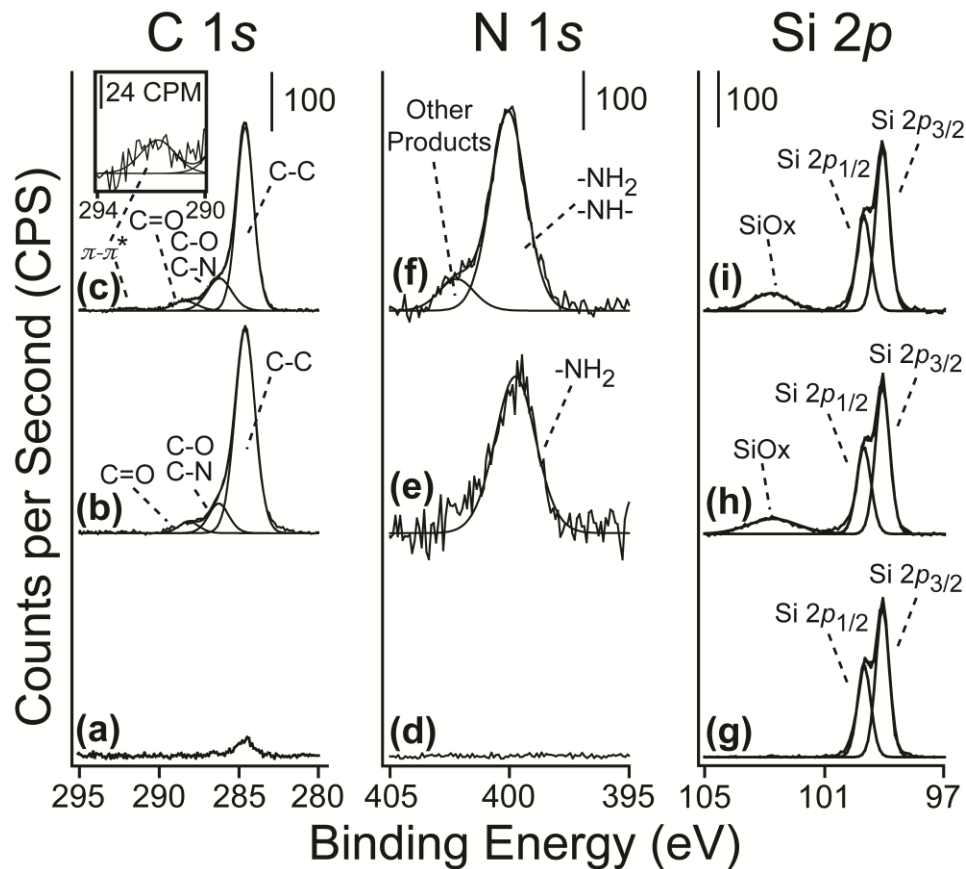


Figure 3.2: High-resolution XPS spectra of: 3.2(a,d,g) C 1s, N 1s, and Si 2p regions, respectively, for H-terminated Si(111) surface; 3.2(b,e,h) C 1s, N 1s, and Si 2p regions, respectively, for AUD-Si(111) surface; and 3.2(c,f,i) C 1s, N 1s, and Si 2p regions, respectively, for PCBM-AUD-Si(111) surface.

Figures 3.2(d-f) show the N 1s region of the hydrogen-terminated silicon, deprotected 1-amino-10-undecene on silicon, and the PCBM-AUD monolayer on silicon, respectively. In Figure 3.2(d), there is no nitrogen observed on the surface, which is expected because no nitrogen has been introduced to the sample during this preparation step. In Figure 3.2(e), the N 1s region of the AUD sample exhibits a peak at 399.8 eV corresponding to the -NH<sub>2</sub> termination (as confirmed later in this section). There is also a small shoulder at 401.6 eV that likely corresponds to the oxidized

nitrogen peak that appeared to be produced during sample transfer to the XPS chamber. The positions of both of these peaks are very much consistent with previously reported literature values [44, 88, 121, 124]. Figure 3.2(f) shows the N 1s region of the PCBM terminated sample. Here, there are clearly two different peaks that can be identified. The first at 399.7 eV corresponds to the  $\text{-NH}_2$  termination of unreacted nitrogen sites [44, 121, 124]. The second peak is detailed further in discussion below. In Figure 3.2(g-i), the Si 2p region is shown. In Figure 3.2(g), two bulk silicon peaks, the  $2p_{3/2}$  and  $2p_{1/2}$ , are observed at 98.9 eV and 99.5 eV, respectively [125]. No oxidation is seen. An oxide-free surface is imperative during SAM formation. In Figures 3.2(h-i), some oxidation is seen, as signified by a feature at around 103 eV [125]. Although the ultimate goal is to produce a completely oxide free surface to completion, in this experiment, the oxide presence occurred after initial monolayer formation with the 1-amino1-10-undecene, and was not shown to be detrimental to the chemistry in this system.

Figure 3.3 shows the magnification of the N 1s region for the PCBM-reacted sample. A minor contribution to the feature centred at approximately 402.3 eV comes from the oxidation observed before PCBM reaction. However, this is clearly not the only contribution. Figure 3.3 also plots the N 1s energies predicted for **Structure 1** and **Structure 2** using DFT calculations (see section 3.3.3 and section 3.4.5) [118]. The three bars shown below the experimental spectrum correspond to the computational predictions for amino-terminated surface (right, black bar), **Structure 2** product (middle, blue bar), and **Structure 1** product (left, red bar). The positions of the computationally predicted values in Figure 3 are relative to the peak predicted for the amino-terminated silicon surface ( $\text{-NH}_2$ ) that was matched with the experimental

value. Consistent with the experimental observation, formation of either one of the two types of proposed structures is expected to shift the N 1s level bands towards higher binding energy, with **Structure 1** shifting more than the **Structure 2** product. It should be noted that the previous DFT calculations following C<sub>60</sub> fullerenes on the surface yielded a slightly lower binding energy for a secondary amine formed during attachment [44]. The difference between two peaks with distinctly different N 1s binding energies obtained experimentally for the AUD-terminated sample and PCBM-modified surface experimental energies is 2.2 eV, which is consistent with the predicted shift of approximately 1.7 eV for **Structure 1** or 1.0 eV for **Structure 2**. Thus, based on this comparison, it is inferred that the chemical reaction has occurred and the observed binding energy shift could be explained by the presence of either **Structure 1** or **Structure 2** products on the surface. It does seem that the experimental results are in better agreement with **Structure 1** formation; however, this information is not sufficient to identify the surface product. In addition, the possibility of physisorption (and even clustering) of PCBM has to be considered. That is why the topography of the surface had to be interrogated by AFM, as described in the next section 3.4.2.

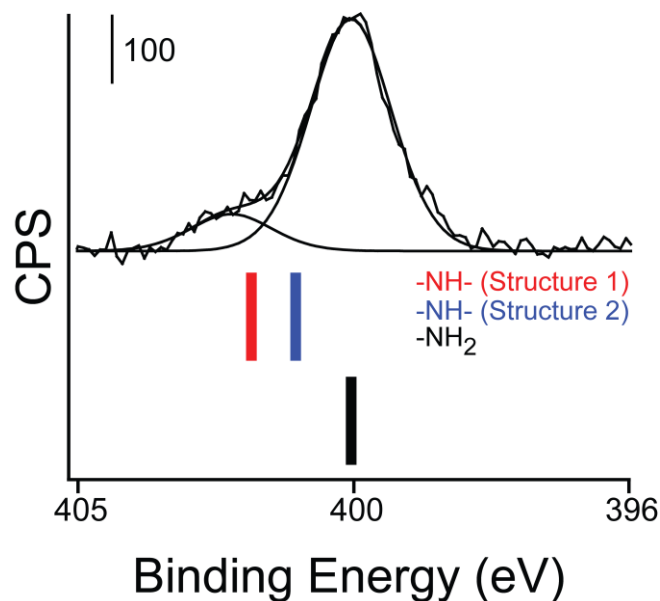


Figure 3.3: N 1s region of Si(111)-AUD-PCBM sample in addition to Si(111)-AUD (black line), Si(111)-AUD-PCBM **Structure 2** (blue line), and Si(111)-AUD-PCBM **Structure 1** (red line) models

### 3.4.2 Topography Changes Followed by AFM

Following topographical changes may prove crucial in understanding the process of chemisorption of PCBM on functionalized silicon. Figure 3.4 shows the AFM images of the hydrogen-terminated surface, the amino-terminated surface, and the PCBM-terminated surface at a 3-hour reaction time and a 5-hour reaction time. A representative line profile is included in each image. In Figure 3.4(a), a 1  $\mu\text{m}$  x 1  $\mu\text{m}$  hydrogen-terminated surface is shown. Atomic steps are clearly observed in the image. These atomic steps are approximately 0.3 nm in height, which corresponds to the size of a single atomic step on a silicon surface [126]. No dust or contaminants are observed in this experiment.

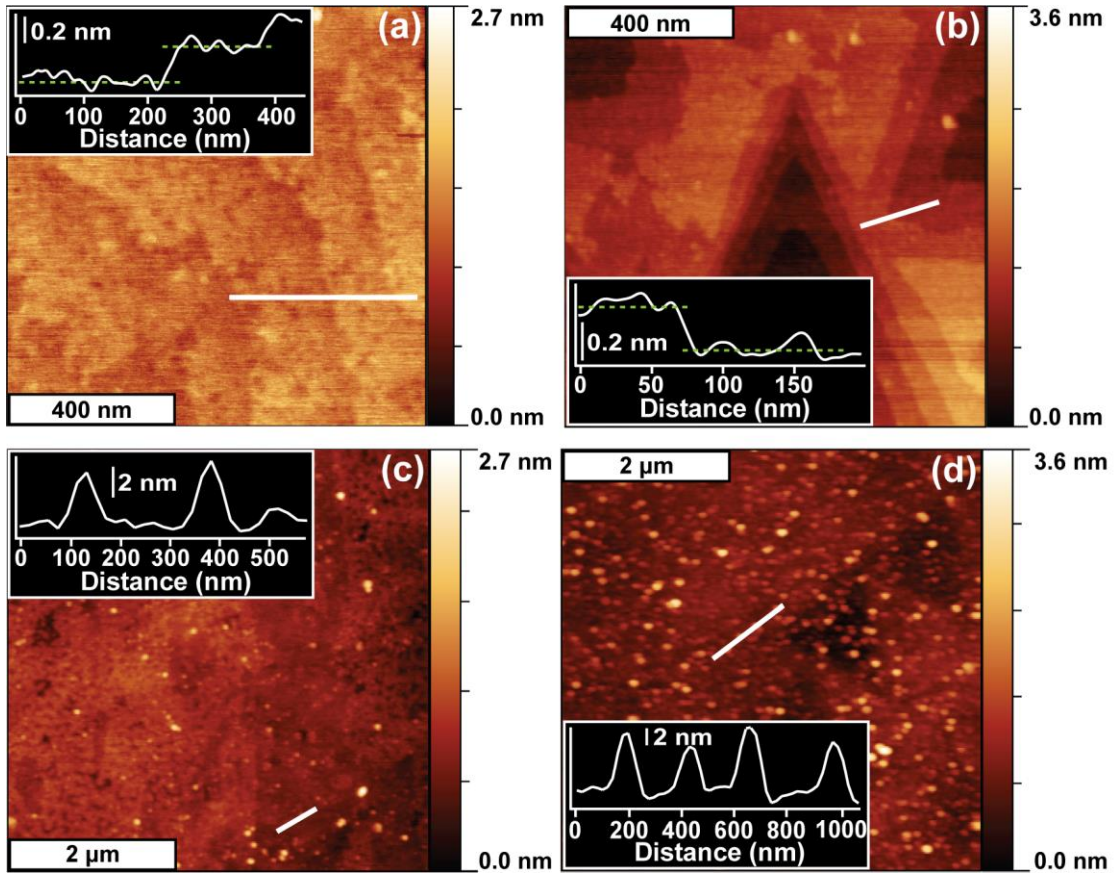


Figure 3.4: AFM images of: (a) H-terminated Si(111) wafer; (b) AUD-modified Si(111), (c) PCBM-terminated Si(111) wafer (exposure time 3 hours), (d) PCBM-terminated Si(111) wafer (exposure time 5 hours). The corresponding line profiles (white lines in each figure) are shown as an inset in each image.

Figure 3.4(b) shows a  $1 \mu\text{m} \times 1 \mu\text{m}$  amino-terminated surface. Similarly to the hydrogen-terminated surface in Figure 3.4(a), the 0.3 nm atomic steps are clearly observed. The surface is still free of contaminants and nearly atomically flat, with  $R_{RMS,AUD}=0.414 \text{ nm}$ . Again, it is important that the surface (that in this experiment is hydrophilic) is still contaminant-free.

Figure 3.4(c) shows a 5  $\mu\text{m}$  x 5  $\mu\text{m}$  PCBM-reacted surface at a reaction time of 3 hours. Here the atomic steps can no longer be observed as clearly as on the previous images; however, the overall surface roughness ( $R_{RMS,PCBM-3hr}=1.84$  nm) has increased, consistent with the presence of clearly distinguishable bright features corresponding to PCBM modification. The spacing between these particles is uniform, and it does not appear that any large clusters are formed. A representative line profile displays that the produced features are approximately 2.8 nm in height with a full width at half maximum (FWHM) of nearly 40 nm. The height is perfectly consistent with the presence of multifunctional PCBM molecules at submonolayer coverage. The large apparent FWHM can be mostly attributed to the tip effect, although when PCBM is dissolved in toluene, domain sizes of over 100 nm in size can be found [27]. The number is consistent with the previous studies of  $C_{60}$  fullerenes on the same surface [44]. In other words, at this regime, one molecule-high features are formed that likely corresponds to single PCBM molecules reacted with the functionalized silicon surface. Any PCBM not directly attached to the surface is washed away when rinsing. The formation of small one monolayer tall clusters cannot be completely ruled out, however, based on this investigation.

In Figure 3.4(d), a 5  $\mu\text{m}$  x 5  $\mu\text{m}$  PCBM-terminated surface at a reaction time of 5 hours is shown. Much like the 3-hour sample, the surface is much rougher than the hydrogen- and amino-terminated samples ( $R_{RMS,PCBM-5hr}=2.19$  nm). Compared to the 3-hour sample preparation time, the PCBM molecules actually appear to form small clusters because the apparent height of the observed features increases to approximately 4.0 nm.

Thus, to understand the chemistry of PCBM, shorter exposure times (3 hours) and relatively low PCBM concentration have to be used to insure the formation of adsorbate at submonolayer coverage. By itself, this technique does not confirm the chemisorption, and the chemical state of the adsorbed molecules has to be interrogated further.

### 3.4.3 Vibrational Identification of Surface Species Produced by PCBM Modification

Figure 3.5 summarizes the relevant experimental FT-IR results and the DFT-predicted spectra for model structures. All of the DFT-predicted results shown in Figure 3.5 were scaled by 0.945 applied to the CH stretching region. Spectrum in Figure 3.5(a) corresponds to the PCBM in KBr pellet. In the CH stretching region, the asymmetric  $\nu_a(\text{CH}_2)$  and symmetric  $\nu_s(\text{CH}_2)$  vibrational stretching frequencies from the alkyl chain of the PCBM molecule is observed at  $2925\text{ cm}^{-1}$  and  $2955\text{ cm}^{-1}$ , respectively. The phenyl C-H stretches are observed above  $3000\text{ cm}^{-1}$ . A strong, sharp peak at  $1730\text{ cm}^{-1}$  is attributed to the C=O stretching mode. In Figure 3.5(b), the experimental Si(111)-AUD-PCBM (5 hr) results are given. In the CH stretch region, strong  $\nu_a(\text{CH}_2)$  and  $\nu_s(\text{CH}_2)$  absorption bands at  $2921\text{ cm}^{-1}$  and  $2851\text{ cm}^{-1}$ , respectively, are observed if a clean silicon surface would be used as a background (not show). These values are expected for a well-ordered system [41, 44, 89, 93, 127-130]. This signature of a well-ordered hydrocarbon sample originates from the alkyl chains of 1-amino-10-undecene. However, to emphasize the absorption bands characteristic of PCBM reaction, the background used in Figure 3.5(b) is the AUD-terminated silicon crystal. The absorption features observed above  $3000\text{ cm}^{-1}$  in this sample are indicative of the presence of aromatic C-H. The peak at  $1729\text{ cm}^{-1}$

corresponds to the C=O stretching of the carbonyl group in the PCBM, which agrees well with the literature data [131]. This peak is one of the indicators of whether the reaction proceeds towards **Structure 1** or **Structure 2** product because 1-amino-10-undecene does not have a carbonyl group. Figure 3.5(c) shows the AUD-PCBM in KBr results. This is very similar to the PCBM in KBr spectra (Figure 5(a)). The only substantial difference is the  $\nu_d(\text{CH}_2)$  and  $\nu_s(\text{CH}_2)$  vibrational stretching frequencies that indicate a much more ordered alkyl chain system for the AUD-PCBM in KBr compared to those for the PCBM in KBr. This stems from the presence of long hydrocarbon chain in this sample. In the carbonyl region, no shift of the C=O stretching frequency is observed, which is a crucial indication that the carbonyl group of the PCBM molecule does not change its chemical surroundings during PCBM reaction with aminofunctionality.

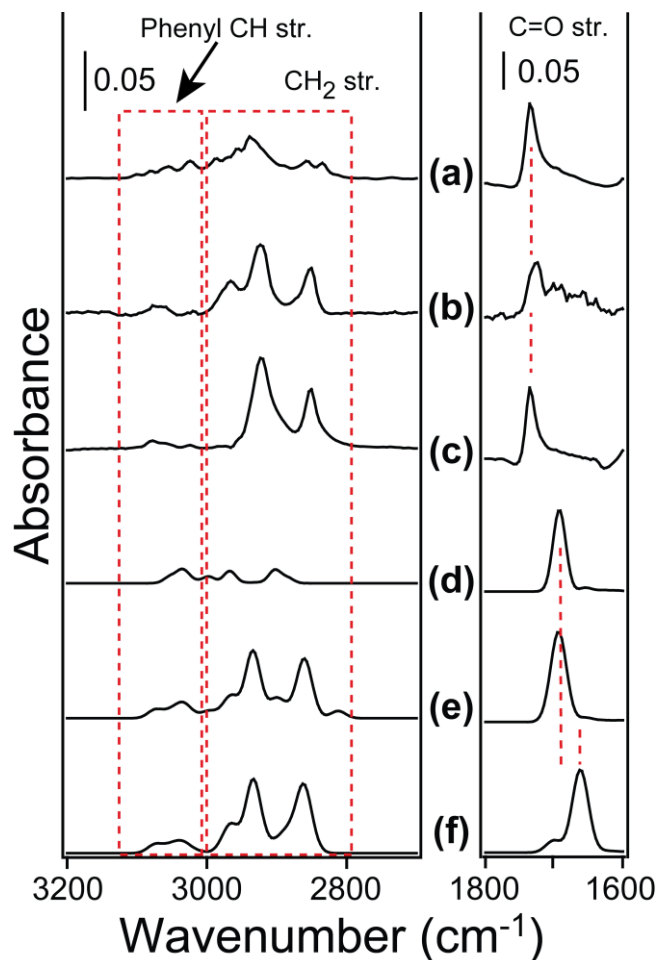


Figure 3.5: Experimental and computational investigation of PCBM adsorption on AUD-functionalized Si(111) surface: (a) experimental spectrum for PCBM in KBr; (b) experimental spectrum for Si(111)-AUD-PCBM-5 hr system; (c) the product of AUD reaction with PCBM in KBr pellet; (d) the DFT-predicted spectrum of PCBM; (e) the DFT-predicted spectrum for **Structure 2**; and (f) the DFT-predicted spectrum for **Structure 1**. The background spectra for the experimental studies presented in (a) and (c) were collected with a pure KBr pellet. AUD-functionalized silicon sample was used as a background for spectrum (b).

In Figure 3.5(d-f), the DFT-predicted frequencies of PCBM, product **Structure 2**, and product **Structure 1** are shown, respectively (see section 3.3.3). In

Figure 3.5(d), absence of intense  $\nu_a(\text{CH}_2)$  and  $\nu_s(\text{CH}_2)$  vibrational stretching modes and the presence of C-H phenyl stretching correlate well with the experimental results. A strong peak predicted at  $1692\text{ cm}^{-1}$  is the C=O stretching mode. In Figure 3.5(e), the DFT-predicted **Structure 2** is expected to exhibit strong absorption peaks for the C-H vibrations of the alkyl group as well as the C-H phenyl stretches. The predicted frequency for the C=O stretching mode is unchanged at  $1692\text{ cm}^{-1}$ . Figure 3.5(f) plots the DFT-predicted frequencies for **Structure 1**. Again, strong absorption bands are predicted for the  $\nu_a(\text{CH}_2)$  and  $\nu_s(\text{CH}_2)$  vibrations of the alkyl chain and C-H of the phenyl ring. However, in this case, a pronounced shift of  $30\text{ cm}^{-1}$  is predicted for the C=O stretch, which decreases to  $1662\text{ cm}^{-1}$ .

This pronounced vibrational signature change for **Structure 1** is not observed in the experimental data. The chemical environment of the C=O fragment is identical in molecular PCBM and in the same molecule tethered to the surface via the  $\text{C}_{60}$  cage (**Structure 2**). However, chemical environment of this group and thus its vibrational signature is expected to change if **Structure 1** were dominant on a surface. Thus, according to the infrared studies supplemented with the DFT calculations, **Structure 2** should be the expected product of PCBM interaction with functionalized silicon surface.

#### 3.4.4 Identification of the PCBM Chemisorption Structure by ToF-SIMS

To complement the infrared spectroscopy studies that provided information about the majority surface species, we have also performed the time-of-flight secondary-ion mass-spectroscopy measurements, whose high sensitivity is used to analyse both majority and minority surface adsorbates.

Before the reaction of PCBM and the amino-terminated silicon surface, the amount of  $C_{60}N^-$  recorded is effectively zero. As the PCBM is introduced into the reaction, the concentration of  $C_{60}N^-$  is recorded to increase. Of course, the intensity of the peaks for powder AUD-PCBM and PCBM samples cannot be directly compared to the surface adsorbate structures because of the relatively low concentration of PCBM in the samples produced on silicon compared to that in powder.

Figure 3.6 plots the relative concentrations recorded for the different samples in the  $OCH_3^-$  region (Figure 3.6(a-e)) and  $C_{60}N^-$  region (Figure 3.6(f-j)) for (a,f) Si(111)-AUD-PCBM (5 hr), (b,g) Si(111)-AUD-PCBM (3 hr), (c,h) analogous AUD-PCBM experiment, (d,i) molecular PCBM, and (e,j) Si(111)-AUD. In the  $OCH_3^-$  region, Figures 3.6(a-d) show a peak at  $m/z$  31.02, which corresponds to the  $OCH_3^-$  group. A small peak that may be from contaminants adsorbed on a surface during transfer at the same  $m/z$  is observed in Figure 3.6(e). A large peak at  $m/z$  31.00 in Figure 3.6(e) originates from  $NOH^-$  species from surface oxidation. This peak is greatly reduced when PCBM is introduced into the sample, and is non-existent in the molecular PCBM sample. Thus, because the  $OCH_3^-$  peak is still present following the reaction of PCBM with the surface, it is inferred that the product of the type of **Structure 2** (which has the  $OCH_3$  group) dominates as opposed to the **Structure 1**, which does not contain this fragment.

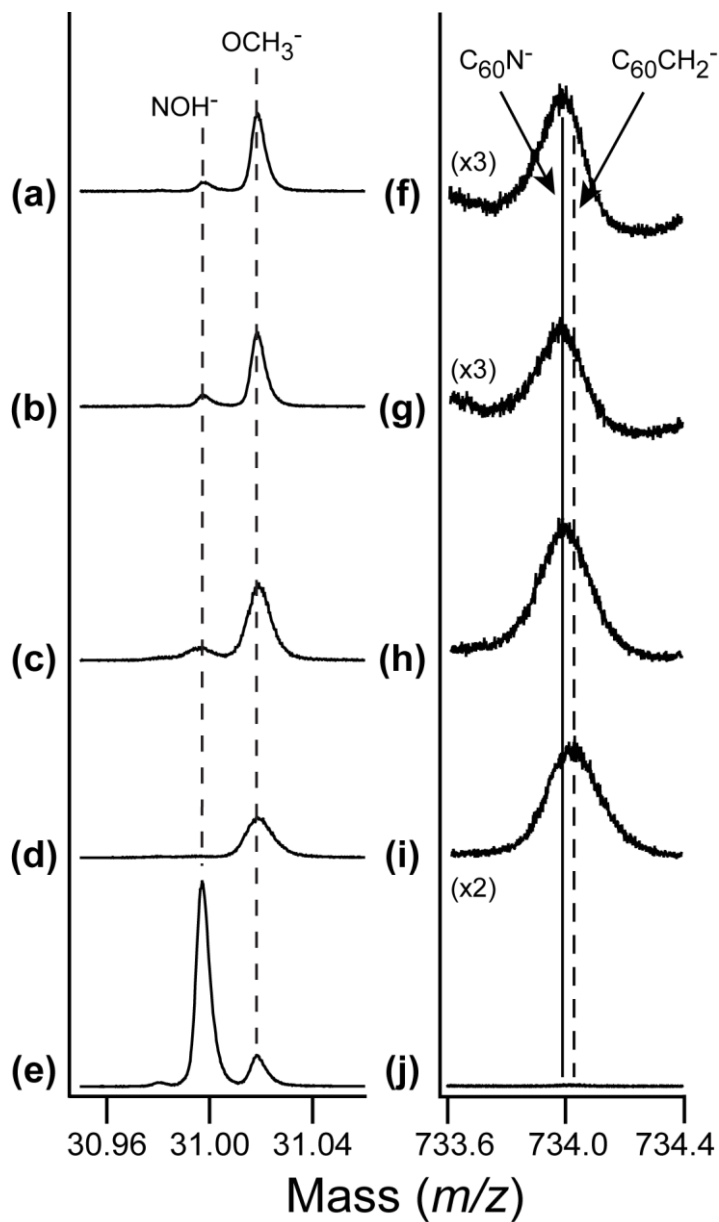


Figure 3.6: The ToF-SIMS results for the  $\text{OCH}_3^-$  and  $\text{C}_{60}\text{N}^-$  regions for (a,f) Si(111)-AUD-PCBM (5 hr); (b,g) Si(111)-AUD-PCBM (3 hr); (c,h) analogous AUD-PCBM experiment; (d,i) molecular PCBM; and (e,j) Si(111)-AUD. The constant presence of the  $\text{OCH}_3^-$  peak at  $m/z$  31.02 and presence of the  $\text{C}_{60}\text{N}^-$  peak at  $m/z$  734.984 are indicative of the **Structure 2** product.

On the right side of Figure 3.6, the  $C_{60}CH_2^-/C_{60}N^-$  region is shown. In the Si(111)-AUD sample (Figure 3.6(j)), no  $C_{60}$  is present in the sample, and no peaks are expected to be observed. After PCBM is introduced, the large peak in Figures 3.6(f-i) appears centered around  $m/z=734$ . There are two possible fragments that this peak has originated from, and both involve the  $C_{60}$  cage. The first is the  $C_{60}CH_2^-$  fragment ( $m/z$  734.02) and the second is the  $C_{60}N^-$  fragment ( $m/z$  734.003). The position of this peak observed experimentally for PCBM is  $m/z=734.016$ , which is completely consistent with the expected result. However, following the reaction of PCBM with the aminofunctionalized surface, the position of this peak shifts to lower  $m/z$ . It becomes  $m/z$  733.984 following the reaction of AUD with PCBM and remains extremely close to this position for surface reaction. The observed value for 5 hr reaction is  $m/z$  733.987. This is fully consistent with the formation of the  $C_{60}N^-$  fragment following surface reaction.

Thus, the ToF-SIMS results indicate that the 1-amino-10-undecene and PCBM react through the  $C_{60}$  rather than the ester, in a complete agreement with the FT-IR results.

### **3.4.5 Analysis of the Formation of Possible PCBM Chemisorption Structures by DFT**

In addition to predicted N 1s core level energies described in section 3.4.1 and predicted infrared spectra analysed in section 3.4.3, the energetic landscape for the PCBM reaction with primary amines comprising modified SAM on Si(111) was explored. The model with the  $Si_{10}H_{15}$  cluster was used to calculate the energy of the products and reactants. Figures 3.7(a,b) displays the cluster models used for both products. The energy of the reactants (AUD-modified cluster and PCBM) was set to

0.0 kJ/mol. The product that formed through the C<sub>60</sub> cage (**Structure 2**) was found to be -9.5 kJ/mol relative to the reactants, and the product that formed through the ester to form the amide (**Structure 1**) as well as methanol was found to be -18.4 kJ/mol relative to the reactants. For the DFT predicted **Structure 2** product, the 1-amino-10-undecene was reacted through the furthest [6,6] bond. It has been shown that reactions of amines and C<sub>60</sub> prefer the [6,6] bond over the [5,6] bond [108, 132]. Other possible products were modelled (including reaction over the [5,6] bond), but their energy was greater than the reactants and they were not included in further study.

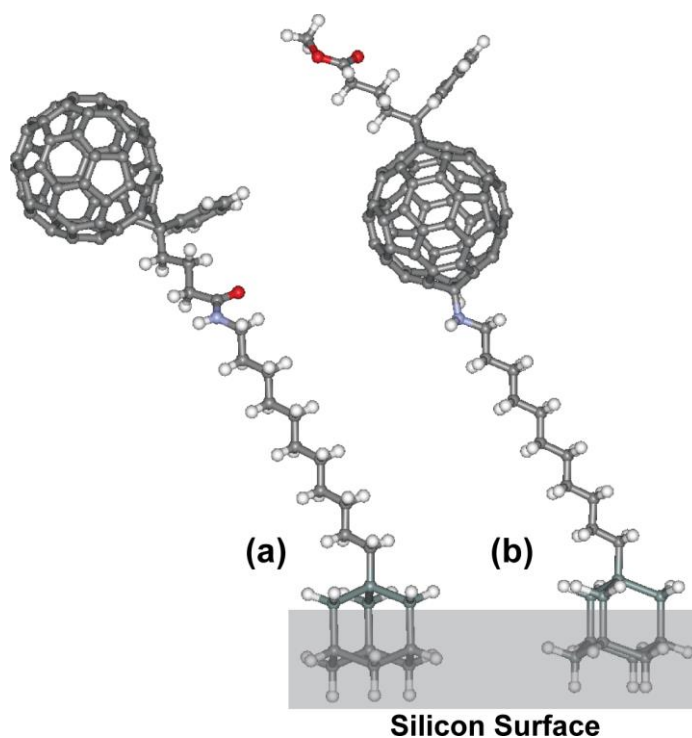


Figure 3.7: Optimized models of (a) product **Structure 1** and (b) product **Structure 2**. Methanol is also a product of the reaction resulting in **Structure 1** but it is not shown. The N 1s core level energy comparison used to compare with the experimental XPS spectra utilized these models.

To reduce the time required for the transition state calculations, propylamine was used in lieu of the 1-amino-10-undecene attached to the  $\text{Si}_{10}\text{H}_{15}$  cluster. The final energies were comparable to the full DFT models for **Structure 1** and **Structure 2**, respectively: -17.8 kJ/mol (propylamine) vs. -18.4 kJ/mol (Si(111)-AUD); and -9.7 kJ/mol (propylamine) vs. -9.5 kJ/mol (Si(111)-AUD). The energy barrier required to reach the **Structure 1** product is 119.3 kJ/mol compared to the reactants and the energy barrier for the **Structure 2** product is 131.4 kJ/mol. Figure 8 summarizes the structures of reactants and products and indicates the corresponding energies, including the energies of the corresponding transition states.

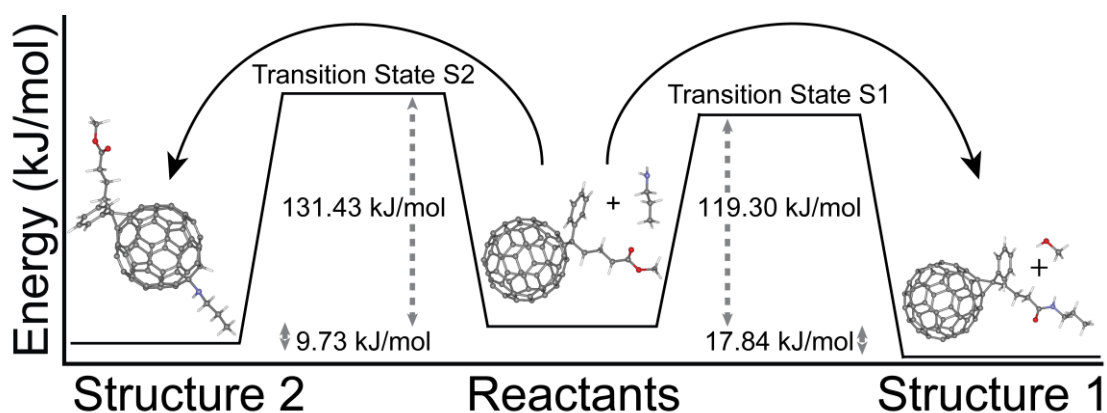


Figure 3.8: Graphical representation of the gas phase rest energies of the reactant, products, and transition states of the propylamine and PCBM reaction. The reactants were set to 0.0 kJ/mol and the relative rest energies of the products and transition states were compared to rest value.

Basically, these simple calculations indicate that there is no substantial thermodynamic or kinetic preference for the formation of one structure over the other although **Structure 1** is slightly more thermodynamically favorable. So how can these

findings be reconciled with the experimental evidence that suggests that the C<sub>60</sub> reaction site is preferred and that the PCBM attachment to AUD-modified Si(111) surface leads predominantly to the formation of **Structure 2**?

The answer may be very simple. As was mentioned above, there is only one structure of the type of **Structure 1** that is formed between PCBM and an amine. On the other hand, a C<sub>60</sub> molecule has 60 possible reaction sites (bonds). In PCBM, the number is reduced to 59 because the ester derivative is reacted with one of them. Out of all C=C bonds available, the [6,6] bond is more favorable energetically compared to the [5,6] bond, thus the number of possible bonding sites is further reduced to 29. Even if one takes into account that some of possible [6,6] reaction sites may be sterically hindered, there are still at least 20 possible reaction sites on a C<sub>60</sub> cage of the PCBM molecule. For comparable reaction barriers, this is what makes the reaction to occur predominantly via a direct attachment to a C=C bond of the C<sub>60</sub> cage rather than through the ester functionality and to form the product of the type of **Structure 2**. Additionally, the flexibility of the ester chain may come into play in determining the dynamics of the reaction. Compared to the rigid C<sub>60</sub> cage of the PCBM, the ester functionality is flexible, which may reduce the probability of amide formation between the 1-amino-10-undecene and the ester of the PCBM.

### 3.5 Conclusions

In this chapter, an amino-terminated silicon surface was reacted with [6,6]-phenyl-C<sub>61</sub>-butyric acid methyl ester (PCBM) in toluene. Analytical spectroscopy and microscopy was used in conjunction with theoretical predictions to understand the chemistry of this work. According to the DFT reconstruction of the energy landscape for PCBM chemisorption, there were two energetically favorable reactions possible

with similar kinetic requirements. The XPS study confirmed that the reaction has occurred and it involved the nitrogen atom of the primary amine group of the SAM covering the surface of the Si (111) single crystal. AFM investigations suggested that submonolayer coverage of PCBM could be formed on this surface without the formation of clusters that are more than one molecular diameter high. FT-IR identified a C=O absorption band and confirmed that there is no shift in the frequency of this vibration upon the completion of the surface reaction between PCBM and surface amino-groups, while the computational investigation predicted that the formation of the surface product corresponding to **Structure 1** above would shift this frequency substantially. ToF-SIMS results indicated that the nitrogen atom is directly attached to the C<sub>60</sub> cage of the PCBM molecule following surface reaction. Such selectivity and predominant formation of **Structure 2** type products are explained by the fact that there is a large number of possible similar reaction sites on the C<sub>60</sub> cage of PCBM and the flexibility of the ester chain hindering the reaction leading to the formation of **Structure 1**, and, despite similar energetic requirements for other reactions, direct attachment of the surface amino-group to the C<sub>60</sub> cage and the formation of the surface products of the type of **Structure 2** is the main surface reaction pathway for this process. This understanding is essential for further studies of PCBM reacted with functionalized solid surfaces via aminofunctionality.

## Chapter 4

### INVESTIGATION OF THIN TITANIUM CARBONITRIDE COATINGS DEPOSITED ONTO A 4140 STEEL SUBSTRATE

#### 4.1 Abstract

Titanium carbonitride (TiCN) coatings are commonly used in a variety of applications, from microelectronics to high-performance cutting tools. The TiCN coatings grown by chemical vapour deposition are especially attractive because this technique provides a very high degree of control during the procedure. A gas-phase deposition utilizing an organometallic precursor molecule, tetrakis-dimethylamino-titanium was used to grow thin TiCN coatings onto 4000 series steel prepared and cleaned in vacuum. A highly controlled conformal filling was achieved by deposition performed onto a sputter-cleaned steel surface held at 600 K. The film of the overall Ti:C:N composition of 1:1:1 was produced, as demonstrated by Auger electron spectroscopy. In air, these coatings are oxidized but maintain their uniformity, as demonstrated by time-of-flight secondary ion mass spectrometry. The chemical state of the elements in the coatings was investigated by X-ray photoelectron spectroscopy and morphology of the films produced was investigated by atomic force microscopy. Finally, the initial mechanical testing of the films was performed by comparing their Young's modulus to that of the underlying steel. Adapted with permission from [133]. Copyright 2012 Elsevier.

## **4.2 Introduction**

One of the most versatile classes of materials used in applications ranging from diffusion barriers in microelectronics [134-138] to responsive sensors [139] and to wear-resistant tool coatings are transition metal carbonitrides [78, 140]. Recent interest in TiCN-based films for extending tool and machine lifetime sparked a renewed effort to adapt the well-designed methods of highly controlled deposition of TiCN films developed for microelectronics applications for wear-resistant coatings on steel [74]. A TiCN system provides the hardness of a TiC based system with the toughness of a TiN system [71, 72]. It should be noted that once deposited, TiCN is reasonably easily oxidized in air, and in fact, this is what we see after deposition and before characterization [141, 142]. Although this may seem to be a disadvantage, it has been shown that introduction of oxygen into TiCN up to a certain concentration will actually increase the hardness [143]. Although hardness does not always correlate to abrasion resistance [144], it is often a good indicator of the stability of the material in mechanical applications.

In addition to compatibility of the coating material with the substrate, the structure of the interface between them often determines mechanical stability and propensity to delamination [145]. This chapter focuses on essentially ideal surface preparation techniques and on the carrier-free chemical vapour deposition to produce a clean interface between 4140 steel and the TiCN film.

## **4.3 Experimental Details**

### **4.3.1 TDMAT Deposition Procedure**

The detailed procedure for the TDMAT chemical vapor deposition is found in section 2.2.2. A highly controlled conformal filling was achieved by deposition

performed onto a sputter-cleaned 4140 steel surface held at 600 K. The film of the overall Ti:C:N composition of 1:1:1 was produced.

### **4.3.2 Coating Characterization**

Details of characterization techniques and settings are found in section 2.3. Auger electron spectroscopy showed the sample produced in UHV exhibited a Ti:C:N ratio of 1:1:1. In air this coating is oxidized but maintains its uniformity, as demonstrated by time-of-flight secondary ion mass spectrometry. Chemical state of the elements in the coatings was investigated by X-ray photoelectron spectroscopy and morphology of the film and the structure of the interface created were interrogated by atomic force microscopy (AFM) and transmission electron microscopy (TEM). The initial testing of the mechanical properties was performed using a Hysitron TI 900 TriboIndenter™ to obtain Young's modulus.

## **4.4 Results and Discussion**

### **4.4.1 Coating Chemical Concentration Ratios and Chemical State Analysis**

First, the ratio of concentrations for Ti, N, and C in the films was determined *in situ* (in ultra-high vacuum, immediately after deposition) by AES. Sample spectra of (a) sputtered and annealed stainless steel surface and (b) the deposited TiCN films are given in Figure 4.1. As suggested from the data, TiCN coating deposited in these experiments covers the entire sample surface and is oxygen free, as deposited. The ratio of Ti, N, and C in these films is consistently 1:1:1. The details of the calibration procedure and the description of the films are reported in reference [146].

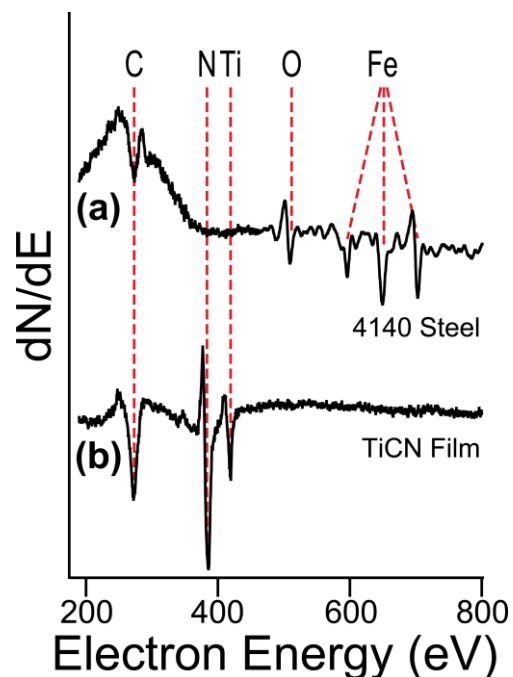


Figure 4.1: AES for TiCN films prepared by  $3.0 \times 10^4$  L exposure of TDMAT onto a clean 4140 steel surface under UHV conditions.

Following a brief exposure of the samples to ambient conditions upon transfer from deposition chamber to XPS chamber, the chemical states of each element in the TiCN coating on the steel substrate were determined through X-ray photoelectron spectroscopy. As shown in Figure 4.2(a-d), the carbon  $1s$ , nitrogen  $1s$ , oxygen  $1s$ , and titanium  $2p$  XPS regions were collected and are shown. The peaks were calibrated against the carbon  $1s$  peak corresponding to adventitious carbonaceous carbon at 284.6 eV. In Figure 4.2(a), the carbon  $1s$  region is shown. Based on our previous studies [147, 148], the peak at 284.6 eV is assigned to the C-C bond. A peak present at 281.8 eV is attributed to the carbide bond, which is normally a few eV lower than the C-C peak. The peak at 286.2 eV may be assigned to either the C-N bond (from the coating) or C-O bond (through oxidation or contamination through air). Finally, the

peak at 288.3 eV corresponds to C=O, which is likely due to oxidized carbon species that formed on the surface during sample transfer.

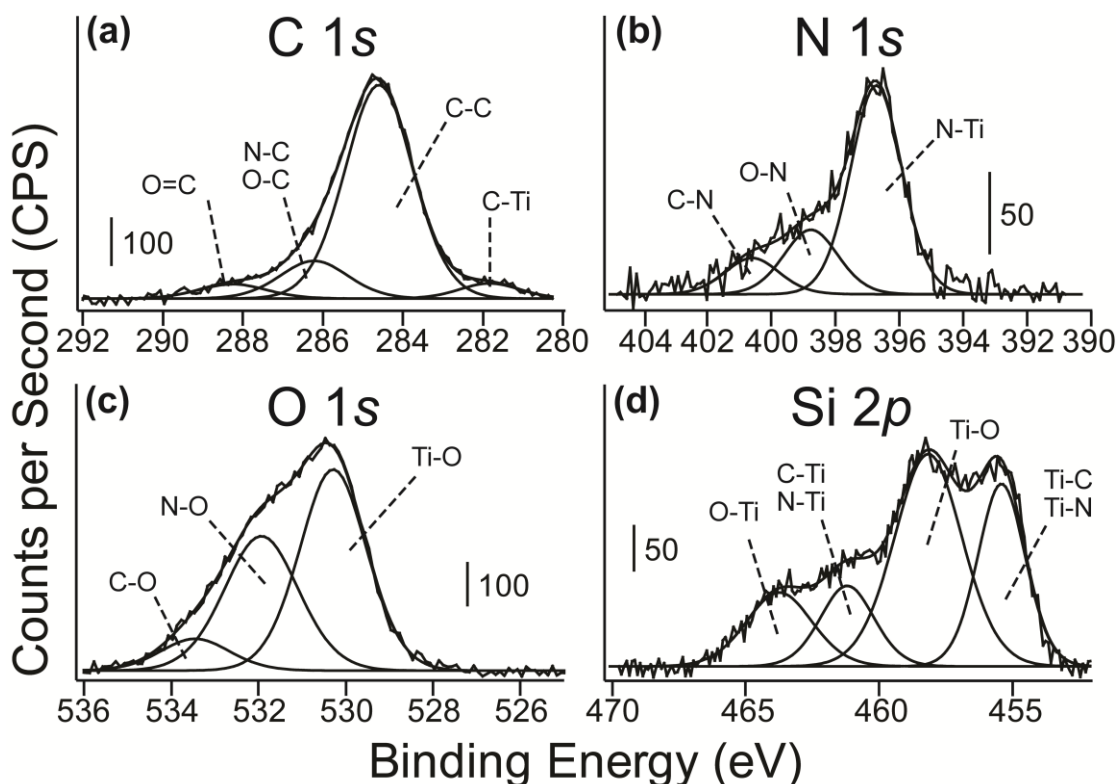


Figure 4.2: XPS spectra of (a) carbon 1s, (b) nitrogen 1s, (c) oxygen 1s, and (d) titanium 2p for TiCN films prepared by  $3.0 \times 10^4$  L exposure of TDMAT onto a clean stainless steel surface under UHV conditions.

Figure 4.2(b) displays the nitrogen 1s region. The peak at 396.7 eV corresponds to the N-Ti bond in the TiCN coating. The N-O oxidation bond is assigned the 398.7 eV peak. The peak at 400.6 eV is assigned to the N-C bond. These assignments are based on previous studies of nitrogen containing compounds on

semiconductor surfaces [147-151] and nitrogen as a part of thin TiCN films [135, 146, 152].

In Figure 4.2(c), the oxygen 1s region is shown. The three peaks in this figure correspond to the oxygen bonds with Ti (530.3 eV), nitrogen (531.9 eV), and carbon (533.5 eV) [135, 146-148, 152]. This figure mostly suggests that all three elements in the coating have varying degrees of oxidation. This is expected because the sample was removed from vacuum after an oxygen-free preparation and exposed to air. As mentioned in the introduction (section 4.2), TiCN oxidizes very readily in air. To test a sample without this oxidation, the XPS must be performed on the same vacuum instrument as the deposition process, which was not possible using the set-up used in the experiment.

In the final panel, Figure 4.2(d), the Ti 2p region is shown. This figure is characterized by two sets of doublets. The doublets occur because of the spin-orbit coupling effects of the final state normally seen for metals [153]. The peaks at 455.3 eV ( $2p_{3/2}$ ) and 461.1 eV ( $2p_{1/2}$ ) correspond to the Ti-C and Ti-N bonds. The peaks at 458.1 eV ( $2p_{3/2}$ ) and 463.7 eV ( $2p_{1/2}$ ) result from the oxidized titanium species [135, 146, 152].

#### **4.4.2 Cross-sectional Analysis of Coating, Interface, and Substrate**

To analyse the structure of the coating and uniformity through the interface, two different methods were utilized. The first, time of flight secondary ion mass spectroscopy (ToF-SIMS), was used to determine the uniformity of the TiCN coating on the 4140 steel substrate while the second, transmission electron microscopy (TEM), was used to understand the structural properties of the TiCN coating as well as to visualize the coating, interface, and substrate.

For ToF-SIMS analysis, the same samples as in section 4.4.2 were used. In Figure 4.3, the depth profile of the UHV-deposited TiCN coating is shown. Because some surface species ionize much more readily than others, a depth profile should not be treated as a specific ‘concentration’ profile. Coupled with the fact that the surface is not completely flat (section 4.4.3), the top few nanometers are expected to be rough. However, one could compare concentrations at different points within a depth profile after the top few nanometers to determine layers and inclusions in the film.

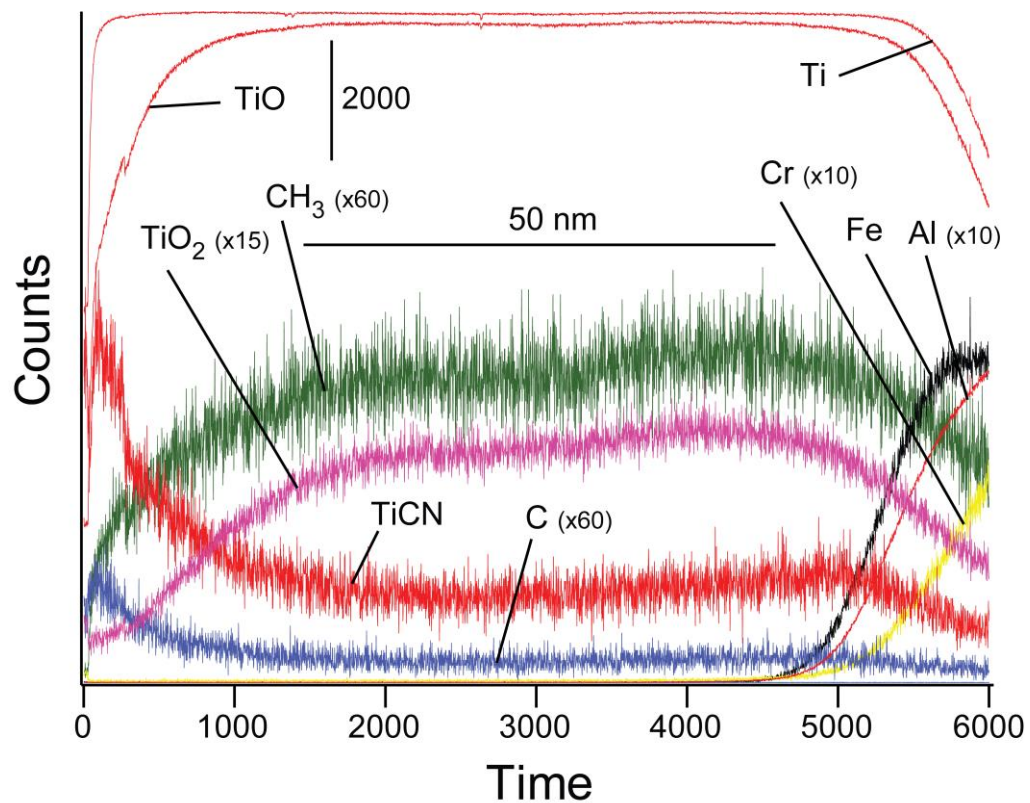


Figure 4.3: ToF-SIMS depth profile of UHV-deposited TiCN. The signals corresponding to selected species have been scaled as indicated to show their relative concentration throughout the sample.

In Figure 4.3, the depth profile is shown as a function of time. Using a previously determined sputtering rate for TDMAT from ToF-SIMS [146], the film thickness was determined to be 74 nm. After approximately the initial 1000 s (16 nm) of depth-profiling, a perfectly uniform coating is observed. Only after the depth reaches approximately 70 nm, the signals corresponding to chromium and iron-containing ions become substantial, while TiCN, TiO<sub>2</sub>, TiO, and titanium ionic signatures all decrease in intensity. In 4140-series steel, iron and chromium are both essential components, so it should be expected that their signals increase once the TiCN coating is removed.

Figure 4.3 also confirms that the entire surface of the samples under investigation is uniformly coated without noticeable exposed steel sample available. Additionally, this set of investigations suggests that the oxidation of TiCN film is uniform throughout the entire thickness of the film and no additional carbon- or oxygen-containing species are formed at the interface between TiCN and steel. Thus, this study suggests a well-controlled, uniform, and conformal film growth, which is especially remarkable given that the surface of the steel sample is relatively rough as shown below.

To understand the structural properties of the TiCN coating, a relatively thick TiCN coating (based on a dose of  $3.0 \times 10^4$  L of TDMAT) was deposited in high-vacuum instrument onto a polished 4140-series steel substrate and examined by cross-sectional TEM. Although this sample preparation approach is different from the one used for AES (section 4.4.1), XPS (section 4.4.1) and ToF-SIMS (previously in this section 4.4.2) studies, it is demonstrated that the films produced are very similar in both cases; however, the exact thickness, of course, depends on the exposure of

TDMAT. As shown in Figure 4.4, there are two distinct regions in the prepared structure (besides the protective carbon layer produced by focused ion-beam deposition): the TiCN region and steel substrate. The carbon layer was deposited to protect the TiCN while preparing the sample. The thickness of the TiCN layer in this experiment is approximately 25 nm and the protective carbon layer is approximately 200 nm thick. The top two images of Figure 4.4 show that the structural uniformity and thickness is consistent over a large area while the bottom two images zoom in on the structure of the film and the interface. In the steel region, one can easily observe the presence of grains. The sharp and well-defined interface is observed between the steel and the TiCN film.

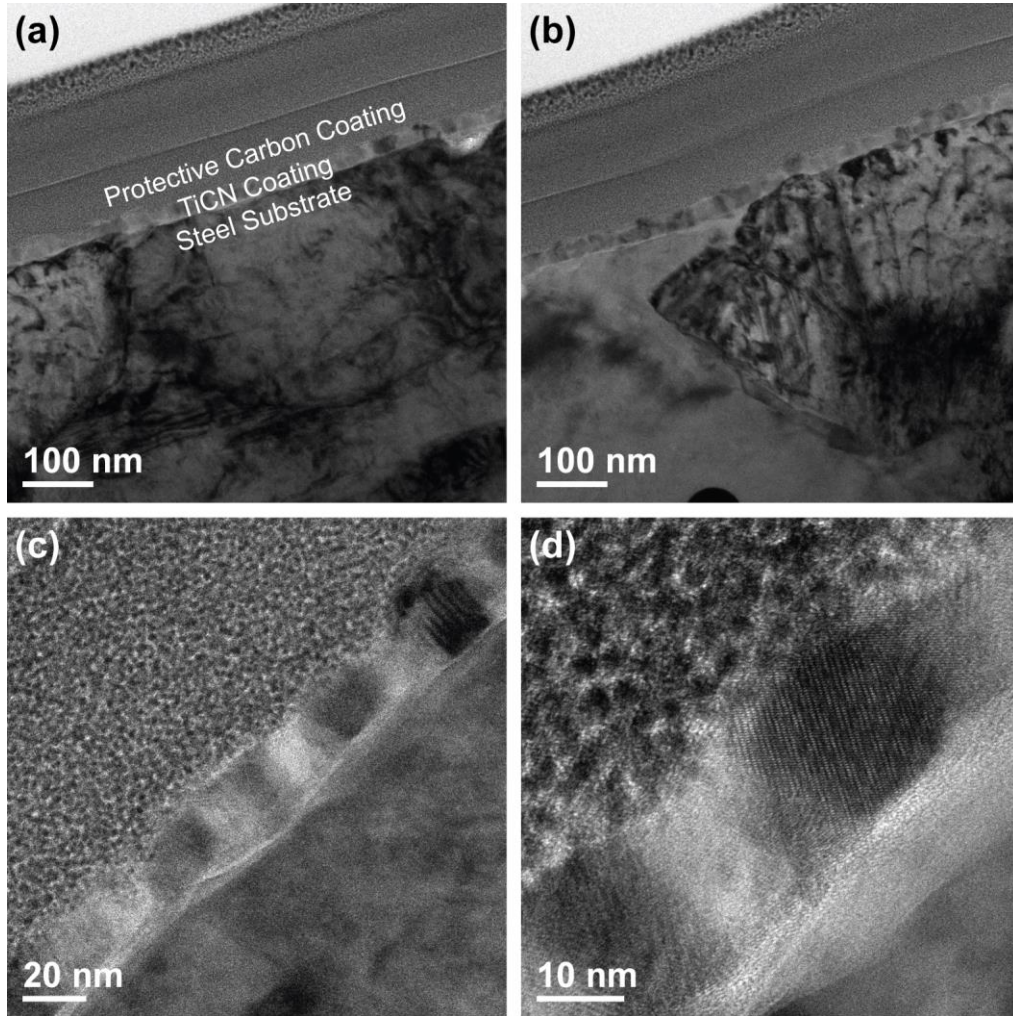


Figure 4.4: Cross-sectional TEM image of  $3.0 \times 10^4$  L TiCN film. Two distinct regions are seen: the TiCN layer and the 4140 steel substrate. A carbon layer was used to protect the TiCN layer while cutting.

Neither the presence of contaminants nor voids are observed between the coating and steel. This further proves the results provided by the ToF-SIMS analysis. In both cases, the film is uniform throughout and the interface is well-defined. Thus, despite the fact that two different deposition procedures (UHV and sputtering vs. HV and simple solvent pre-cleaning) were used, both of them produce well-controlled,

uniform films and sharp, well-defined interfaces. This leads us to conclude that HV deposition is sufficient to produce the desired results. It is very likely that surface oxidation that is unavoidable in HV experiments does not influence the growth of the film substantially and in fact that surface oxygen helps form thermodynamically stable bonds between the components of the TiCN coating and the steel. Further mechanistic and molecular-level studies of the TiCN film growth will be necessary to confirm this assumption.

#### **4.4.3 Substrate and Coating Topography**

The surface topography was investigated by AFM. Images in Figure 4.5 summarize these studies. Images shown in Figures 4.5(a-b) show relatively large areas of the two samples: (a) polished and ion-sputtered 4140-series steel sample prepared in UHV and (b) the UHV-deposited TiCN coating, respectively. Both images look similar, with scratches left by polishing procedure observed on both surfaces. Figures 4(c-d) show the same surfaces but under much higher magnification. In Figure 4(c), the RMS roughness ( $R_{rms}$ ) of the 4140-series steel grain along the white-line profile indicated is 0.40 nm. These roughness values become more important in the following section concerning Young's modulus measurement (section 4.4.4). Thus, although the surface of this microcrystalline material is relatively rough, within a single grain, it is actually very flat. However, it should be pointed out that the grains are not uniform in size.

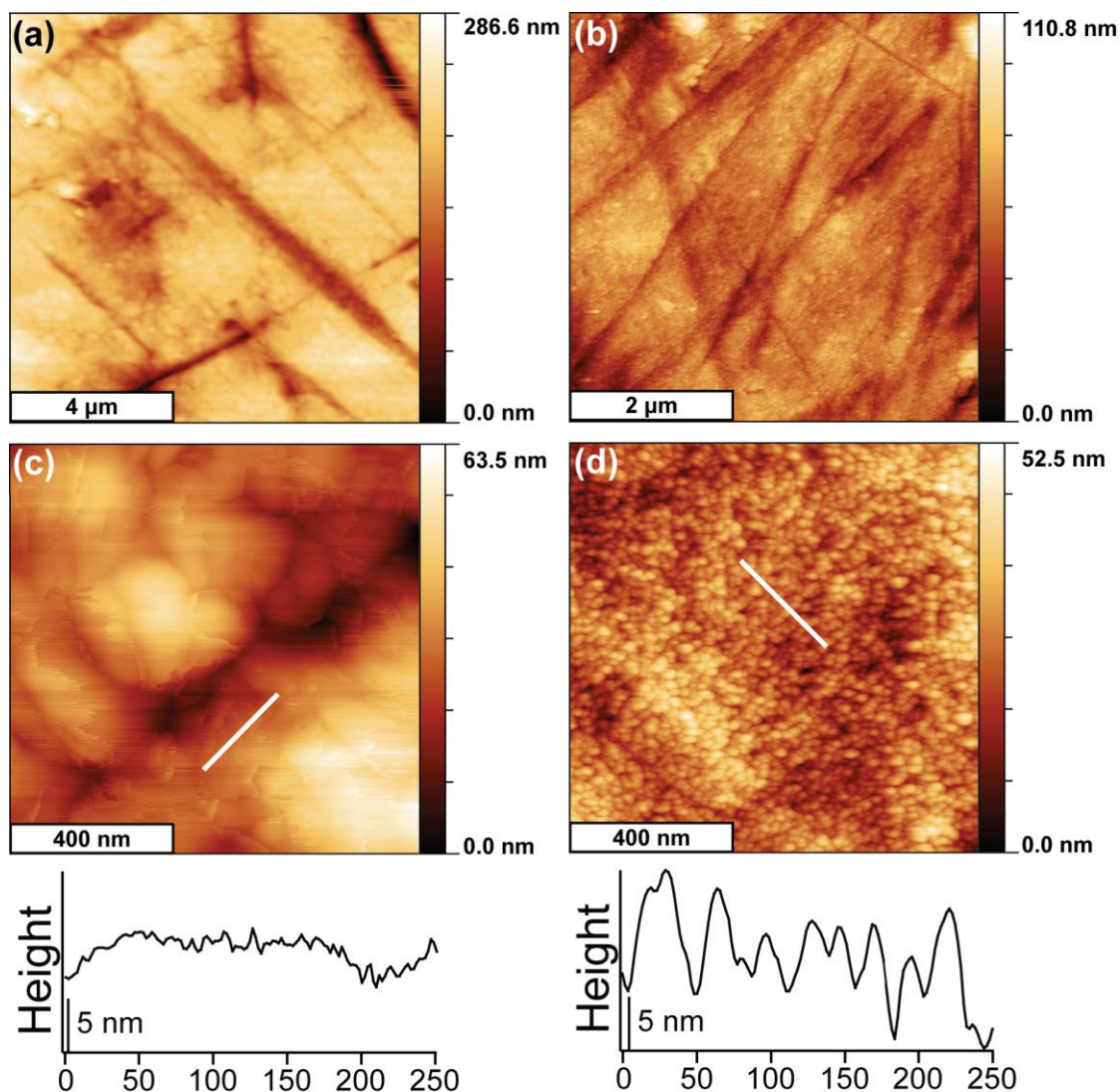


Figure 4.5: AFM image of uncoated 4140-series steel sputtered in UHV conditions (a and c) with respective line profile shown in (c) and AFM images of UHV-deposited TiCN coating (b and d) with respective line profile shown in (d). The line profiles for the micro scale images are shown underneath each image. The scale bars are shown at the bottom of each image.

In Figure 4(d), the UHV-deposited TiCN coating is shown. The roughness ( $R_{rms}$ ) value for this sample is 3.27 nm. This is a larger value compared to the studies

presented in Figure 4(c) for clean stainless steel; however, in this case it seems that TiCN deposition smoothed the boundaries between the grains of the stainless steel, which would be consistent with the results of the ToF-SIMS and TEM (section 4.4.2) experiments presented above. It is especially noteworthy that the tails of several depth profiles of species in ToF-SIMS studies extend further into the stainless steel, likely corresponding to the material that is deposited between the grains in certain regions. The image in Figure 4.5(d) also suggests that the TiCN film is composed of nanoparticles. According to the ToF-SIMS results (4.4.2), these structures are imbedded into a framework that covers the entire surface, likely very similar to the nanoparticles imbedded into the TiCN films used as diffusion barriers [152]. This observation is also consistent with high-resolution TEM studies in Figure 4.4, as the coating produced appears to consist of crystalline nanostructures approximately 20-25 nm in size imbedded in a framework that appears to lack order (possibly amorphous material). This combination actually proved perfect for microelectronics applications and likely possesses a set of very attractive mechanical properties as tested below.

#### **4.4.4 Mechanical Properties of the Substrate and Deposited Coating**

To provide a set of initial benchmark comparisons of mechanical properties of stainless steel with the TiCN coating, we used a Hysitron TI 900 TriboIndenter™ to obtain Young's modulus. Although further studies of the mechanical and tribological properties of the films discussed here are needed, Young's modulus provides a reliable mechanical property compares for thin films to bulk materials. Recall from section 2.3.9 that surface and substrate effects need to be taken into account to obtain a

reasonable Young's modulus value. The model used here to calculate the Young's modulus was described in detail by Tricoteaux et al. [99].

An uncoated 4140-series steel disc was also tested to make sure the measured values were solely from the coating and not from the substrate. From the 27 indentations made at various depths, the Young's modulus of  $671 \pm 159$  GPa (average  $\pm$  standard deviation) was obtained for TiCN film compared to  $259 \pm 32$  GPa for uncoated stainless steel. These numbers are in a very good agreement with those reported in literature for both bulk materials: 210 GPa was reported for 4140 stainless steel [154], and 467-510 GPa range was measured for the bulk titanium carbonitride materials [155]. It should be mentioned that the value obtained for titanium carbonitride varies substantially depending on the sample preparation, on the measurement strategy, and on the model applied to extract the Young's modulus for thin films, where interaction with the substrate is extremely important. In fact, the Young's modulus values for three TiCN coatings on the order of microns based on micro-indentation experiments, as reported by Tricoteaux et al., were 484, 461, and 681 GPa [99].

One final observation that must be pointed out is that the steel substrate is not perfectly flat, which may affect the Young's modulus measurements. The steel grains, in both the uncoated and coated samples, do influence how far the diamond tip penetrates into the sample. This may partially explain the relatively wide confidence intervals obtained in these measurements.

#### **4.5 Conclusions**

In this chapter TiCN was deposited onto a 4140-series steel substrate. TiCN films were grown by CVD both under UHV and HV conditions, using the deposition

precursor TDMAT. Both approaches produced very similar coatings, as confirmed spectroscopically. The *ex-situ* XPS studies showed that the surface is comprised of titanium, carbon, and nitrogen and that the film is partially oxidized in ambient. The ToF-SIMS studies provided a depth profile confirming that the film is uniform and that it covered the entire surface. It also suggested that the interface with the steel should be well-defined. The TEM investigation showed a sharp, clearly observed interface between the coating and steel substrate with uniformity throughout the coating, which is consistent with the ToF-SIMS analysis. The AFM studies showed that the topography of coated and uncoated samples was similar on the macroscopic scale but that the TiCN-covered samples exhibit nanostructuring with the structures on the order of 25-30 nm, forming a complete layer. Finally, the mechanical properties of coated and uncoated samples were tested by measuring Young's modulus, with the results consistent with the properties of steel and bulk TiCN materials. Thus, it is feasible to produce the TiCN coatings on steel by using CVD techniques. The films produced are well-defined and uniform throughout. They exhibit a sharp and well-defined interface between the coating and the substrate steel.

## **Chapter 5**

### **INVESTIGATION OF THICK TITANIUM CARBONITRIDE AND TUNGSTEN CARBIDE COATINGS DEPOSITED ONTO A 4140 STEEL SUBSTRATE**

#### **5.1 Abstract**

Protective hard coatings on steel that are produced by electrospark deposition (ESD) methods that do not require vacuum conditions are compared, and the interfaces formed are interrogated by a combination of analytical methods. A titanium carbonitride (TiCN) coating is produced and compared to a tungsten carbide (WC) ESD coating. Following deposition onto a 4140 grade steel substrate, the coatings were compared by X-ray photoelectron spectroscopy, scanning electron microscopy, energy-dispersive X-ray spectroscopy, transmission electron microscopy, atomic force microscopy, X-ray diffraction, and nanoindentation test to determine the Young's modulus as an indicator of mechanical strength. It was found that the coatings produced void- and impurity-free interfaces but that the interfaces are drastically different for the two coatings investigated and some of the differences are explained based on the different melting points of the two materials that affect the process of ESD. Adapted with permission from [156]. Copyright 2014 Elsevier.

#### **5.2 Introduction**

In the previous chapter, it was shown that a protective TiCN coating was deposited onto a steel substrate using CVD with titanium-containing metalorganic precursor. However, this deposition method is slower than other methods that are used

to produce the hard coatings (for example, to produce a coating of less than 100 nm thick, 30000 L exposure of the precursor molecule was required, which corresponded to the precursor pressure of  $5 \times 10^{-6}$  torr maintained for 100 min). PVD can be used to deposit thicker films within the same time frame; however, the control over the interface formation is more difficult and imprecise, as the deposited films may suffer from delamination [63].

Electrospark deposition (ESD), or electrospark alloying, is a micro-welding technique that welds a metallic electrode onto an electrically conductive substrate and is performed in the ambient environment [66, 157]. It is characterized by a high current, short pulse duration that transfers the electrode material through a plasma arc onto the substrate. During the process, the area of close proximity between the electrode and solid substrate is bathed in an inert gas (usually Ar), eliminating the possibility of interface and surface oxidation. Even though the technique uses a high current, the short pulse duration means that the temperature of the bulk of the substrate does not increase and the heating is only local. Both the electrode and the surface melt for a short period of time. This local rapid heating and cooling (with cooling rates that approach  $1.5 \times 10^5$  K/s) [158] leads to an oscillatory growth [159]. However, the rapid heating and cooling also leads to a thickness where the microstructural and tribological characteristics can be affected [158]. This is due to the forces exceeding coating material's tensile strength and the reduced cooling rate (and accumulation of heat) as the coating becomes thicker [158, 160]. This micro-welding technique has been shown to produce a strong metallurgical bond with the surface that should be resistant to delamination [66, 157, 158, 161-171]. The fact that this method is relatively inexpensive and easy to use made it popular in such applications as repairs

or tool protection [161, 166, 172, 173]. The lifetime increase for ESD-protected tools has been reported to be from 150% [173] to 2000% [172]. Specifically, as would be expected, the wear rates for ESD coatings are significantly reduced compared to any steel substrate, which leads to this lifetime increase.

In all the cases mentioned above, the properties of the coating material are extremely important; however, the properties of the interface (both at the macroscopic level and down to the nanometer scale) are just as important to increasing the lifetime of tools. This chapter investigates the properties and the quality of interfaces formed by ESD of two materials. The first material, tungsten carbide (WC), is a common ESD coating [163, 170, 174-187]. It is used in many other deposition techniques for a wide variety of applications. This coating is investigated to provide a benchmark for a much less investigated titanium carbonitride (TiCN) [188, 189]. Several recent studies suggested that TiCN may possess the properties and produce an interface with steel that are far superior to WC [133, 190, 191]. Podchernyaeva et al. [188] deposited a  $\text{TiC}_{0.5}\text{N}_{0.5}$  coating with SiC, AlN and a Ni-Cr binder additions. It was reported that the  $\text{TiC}_{0.5}\text{N}_{0.5}$  coating has shown less wear and a larger range of sliding velocities compared to a WC coating. Korkmaz and Bakan [189] used a  $\text{TiC}_{0.7}\text{N}_{0.3}$  coating. It was found that the microhardness and the wear resistance increased compared to the steel substrate. However, neither of these two studies investigated an ESD TiCN coating with 1:1:1 ratio of Ti:C:N, which has been previously suggested to possess a set of very attractive properties when deposited using other deposition methods [52, 133, 192, 193] and targeted coatings with additional layers present between the TiCN and steel. This chapter addresses these topics directly.

## **5.3 Experimental Procedures**

### **5.3.1 Deposition Methods**

The detailed procedure for the electrospark deposition is found in section 2.2.3. A commercial technique (NanoFusion™, Advanced Surfaces and Processes, Inc.) was used to deposit the coatings, but, although technically somewhat different from ESD, the deposition method is referred to as ESD for simplicity's sake.

### **5.3.2 Characterization Techniques**

For the coatings deposited, surface elemental concentrations and the corresponding oxidation states were interrogated by X-ray photoelectron spectroscopy (XPS). Elemental analysis and large-scale microscopic images were obtained using scanning electron microscopy (SEM). Cross-sectional analysis was also performed by SEM and energy-dispersive X-ray spectroscopy (EDX). High-resolution transmission electron microscopy was utilized to uncover the structures of the interfaces produced. The structural characteristics of the films were obtained using X-ray diffraction (XRD). The surface topology and roughness were investigated by atomic force microscopy (AFM). The Young's modulus, as an indicator of tribological properties, was measured on a Hysitron TI 900 TriboIndenter™.

## **5.4 Results and Discussion**

### **5.4.1 ESD Deposited Chemical States**

Figure 5.1 plots the XPS spectra for (a) the titanium spectral region before and after deposition of the ESD TiCN coating; (b) the tungsten region before and after deposition of the ESD WC coating; and (c) the iron region before and after deposition of both coatings. The same sample was used to obtain all steel spectra. In

Figure 5.1(a), there is no titanium present on the surface before TiCN deposition, as expected. Following the deposition, titanium is definitely present on the surface. The intense peaks at 458.1 eV and 463.8 eV belong to the oxidized  $Ti^{4+}$  species and exhibit the characteristic spin-orbit coupling split between  $2p_{3/2}$  and  $2p_{1/2}$ . The peaks at 455.3 eV and 461.0 eV belong to the Ti  $2p_{3/2}$  and  $2p_{1/2}$  transitions of the Ti – C and Ti – N species, which is consistent with the previous work in literature as well as Chapter 4 [133, 194-196]. The difference between  $2p_{3/2}$  and  $2p_{1/2}$  peaks for each of the species are identical, which is fully consistent with the spin-orbit coupling effect [197].

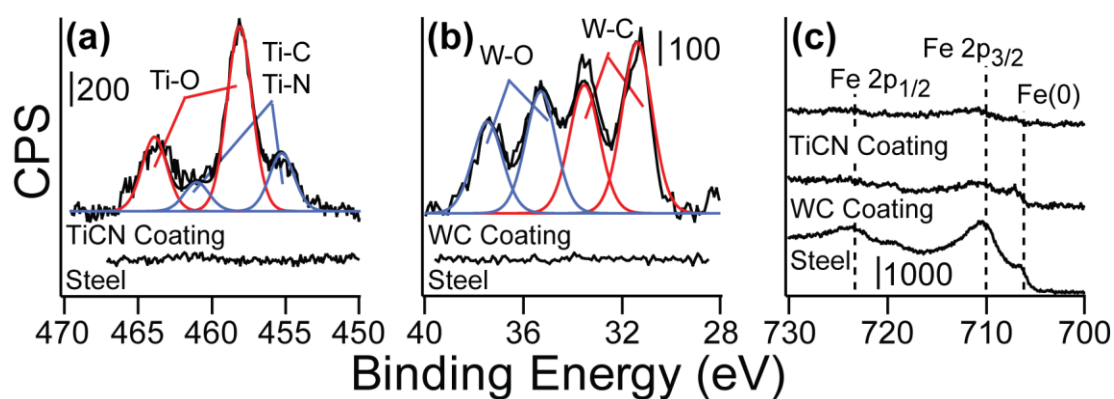


Figure 5.1: XPS analysis of ESD coatings and the steel substrate of the (a) titanium  $2p$ , (b) tungsten  $4f$ , and (c) iron  $2p$  regions.

In Figure 5.1(b), the tungsten region is shown for the bare steel and for the ESD-deposited WC coating. Similarly to the results recorded for the TiCN coating, no tungsten signatures are observed on the steel sample. Also similarly to the titanium spectrum, the spin-orbit coupling doublets are observed for the coating. The peaks at 31.4 eV and 33.5 eV correspond to the W  $4f_{7/2}$  and  $4f_{5/2}$  of the W – C species in

tungsten carbide. The W – O  $4f_{7/2}$  and  $4f_{5/2}$  species peaks from  $WO_3$  are present at 35.3 eV and 37.5 eV, respectively. This observation is in complete agreement with previous peak assignments [198, 199].

Thus, XPS investigation confirms the deposition of TiCN and WC coatings by the ESD method and suggests that the surfaces of both films are oxidized.

In Figure 5.1(c), the Fe  $2p$  region is shown for the 4140 steel sample, WC ESD coating, and TiCN ESD coating. In the spectrum of the 4140 steel, the peak at 707 eV indicates the presence of  $Fe^0$  species based on the previously reported studies [79, 200]. The rest of the observed spectral features are consistent with the signature of iron in  $Fe_2O_3$ . In the WC coating, small peaks at 707 eV and 710 eV indicating the presence of iron can also be observed, although in the TiCN spectra, no peaks indicating the presence of iron were recorded. However, based on the SEM investigations summarized below (section 5.4.2), the possible presence of iron on a surface of ESD-produced samples is adventitious rather than an indication of incomplete coverage, because the thickness of the TiCN or WC films produced by this method is well over 10  $\mu m$ . Thus, the presence of small concentration of iron-containing species on the surfaces of ESD-deposited films most likely originates from the process of mechanical cutting during the sample preparation step.

Overall, the XPS spectra summarized in Figure 5.1 show that ESD produces films of TiCN and WC, respectively, and that the surfaces of these continuous films are oxidized.

#### 5.4.2 Topographic and Cross-sectional Analysis of Coating, Interface, and Substrate

Scanning electron microscopy was used to examine surface morphology on a larger scale and to investigate the interface between the coatings and the substrate by cross-sectional analysis. Figure 5.2 illustrates the morphology of the coatings at 250 X magnification. On this scale, both the TiCN (Figure 5.2(a)) and WC (Figure 5.2(b)) exhibit the typical “splash ” patterns that are commonly observed with electrospark-deposited coatings [66, 70, 158, 162, 163, 167, 168, 182, 201-203]. This “splashing” is caused by the locally-molten droplets rapidly heating and cooling after deposition [163]. As one can see in both of the images, multiple “splash” patterns are observed and the coatings are essentially made up of multiple overlapping “splash” patterns. As confirmed with XPS measurements (section 5.4.1), there are no gaps/porosity in the coatings that show the steel substrate underneath, so this method has high surface coverage.

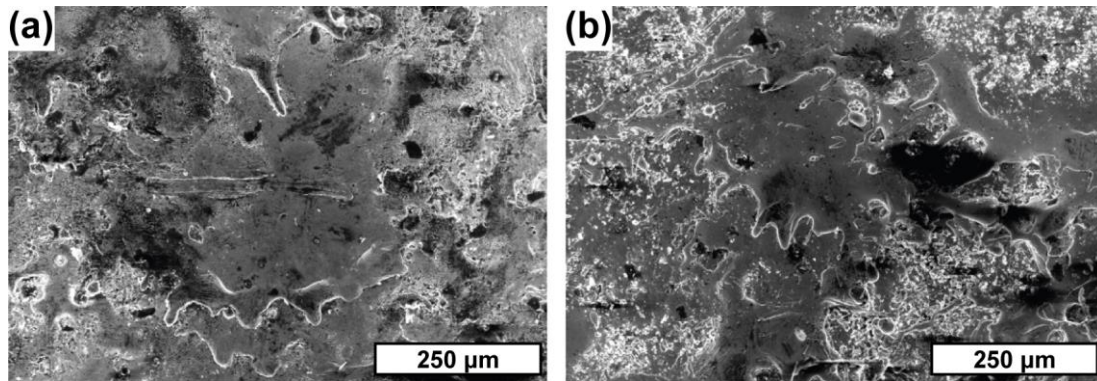


Figure 5.2: Surface (plane view) SEM images for (a) TiCN and (b) WC coatings at 250 X magnification. Both exhibit typical splash patterns commonly observed for electrospark-deposited coatings.

Under higher magnification, differences can clearly be observed between the TiCN and WC coatings. Figure 5.3 illustrates the surface under 10000 X magnification through SEM. Both images are magnified within the “splash” pattern region. The TiCN coating (Figure 5.3(a)) displays a rougher surface with larger features. The WC coating (Figure 5.3(b)) has a smoother surface. This is consistent with the results from the AFM studies in section 5.4.5 below. As shown in that section, the TiCN coating has more pronounced features while the WC coating has lower roughness at the nanometer scale as well.

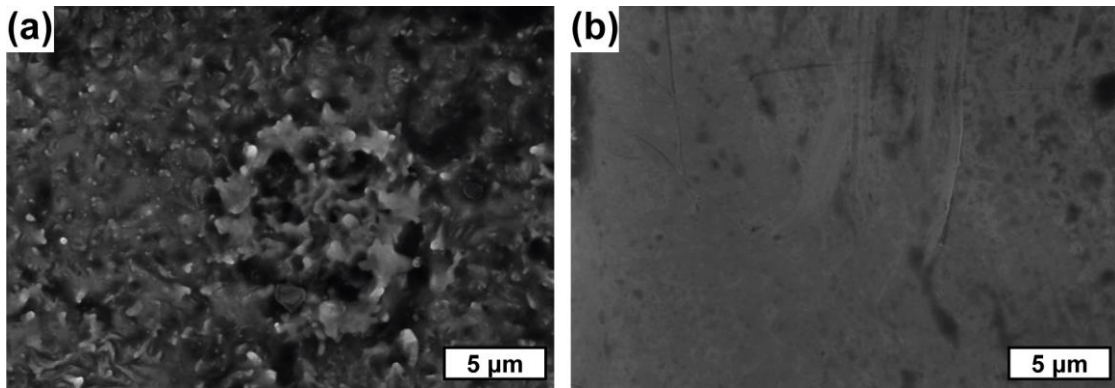


Figure 5.3: Surface (plane view) SEM images for (a) TiCN and (b) WC coatings at 10000 X magnification. Both images were magnifications of the splash patterns seen in Figure 5.2. The TiCN coating is significantly rougher than the WC.

Figure 5.4 shows the SEM cross-section of the ESD WC coating. In this cross-sectional EDX-SEM image, as well as in Figure 5.5, the direction of the line scan proceeds from top to bottom; that is from the coating to the substrate. The line profiles underneath the SEM image are the relative concentrations for each element where the minimum value was set to 0 counts and then the counts were normalized to the

maximum value across the linescan for that element. This was done because the minimum counts for some elements were greater than the maximum for others. The method in meant to show the individual relative concentrations of the elements rather than comparing two different elements with each other. This procedure was performed to account for different sensitivities of elements in EDX. The line-profiles in Figure 5.4 clearly show that upon crossing the interface between the coating and the steel substrate, the concentrations of WC components decrease and the appearance of Fe signature indicates the dominance of substrate material. The interface indicated by a dashed line in the figure is well defined and free of voids. In addition, no concentration spikes of any elements were observed at the interface, again suggesting that the interface is clean and well defined.

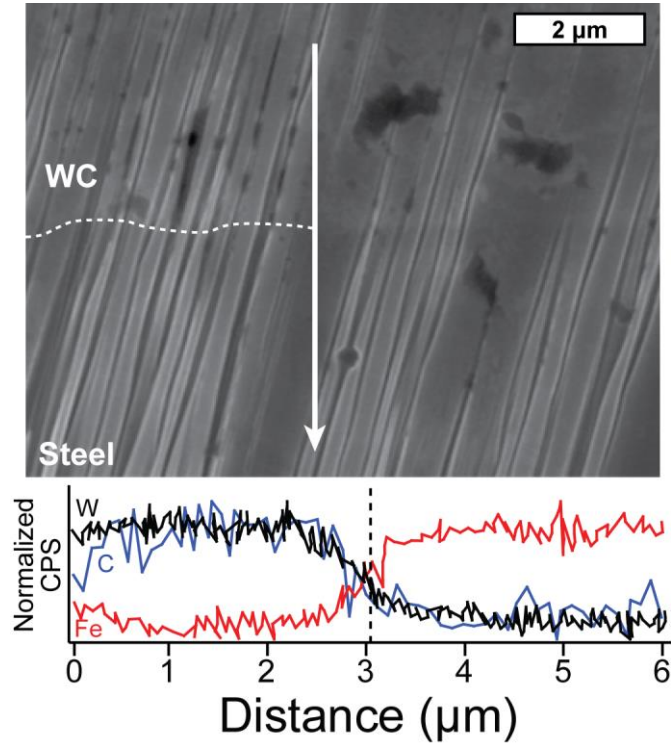


Figure 5.4: SEM cross-section for ESD WC with linescan EDX. The white dashed line in the SEM image represents the WC coating-substrate interface. The red line plots relative Fe concentration in counts-per-second (CPS) along the linescan, the black line plots the relative W (CPS) along the linescan, and the blue line plots the relative C (CPS) along the linescan. The black dashed line in the line profile represents the WC coating-substrate interface.

Figure 5.5 displays similar SEM cross-sectional analysis for TiCN coating produced by ESD. These results are more complex than in the case of WC coating. The region corresponding to the TiCN is indicated by the first 2 μm of the line-profile. The region that corresponds to the steel substrate is observed after approximately 13 μm. However, between those two clearly distinguishable regions there is a mixed layer approximately 11 μm thick. Within this region, there are in phase oscillations of Ti, C, and N corresponding to inclusions of TiCN into the steel matrix. As seen in the TEM

results, at the boundary between the mixed region and the steel, a pure TiCN strip is seen. This unusual observation suggests that instead of a smooth and well-defined interface observed for WC, TiCN coating deposited by ESD exhibits a transition layer, likely produced by intermixing of TiCN droplets during the procedure. The melting point of TiCN is 1450-1480 °C [204, 205], while for WC it is 2870 °C [206]. Because the melting point of 4140 series steel (1415 °C) is near the melting point of TiCN, TiCN droplets can more easily intermix with the steel substrate (as both materials have similar and high mobilities in their molten state) during the deposition and while both materials cool to room temperature. In addition, the specific heat capacity of TiCN is higher and the specific heat capacity of WC is lower [207, 208] than that of steel [209], which can also affect the structural differences of the interfaces formed. In other words, during ESD, TiCN appears to be truly molten into small droplets by local heating, while WC is not. The intermixing can also be observed for the WC sample; however, only at the nano level, as summarized below for TEM studies (section 5.4.3).

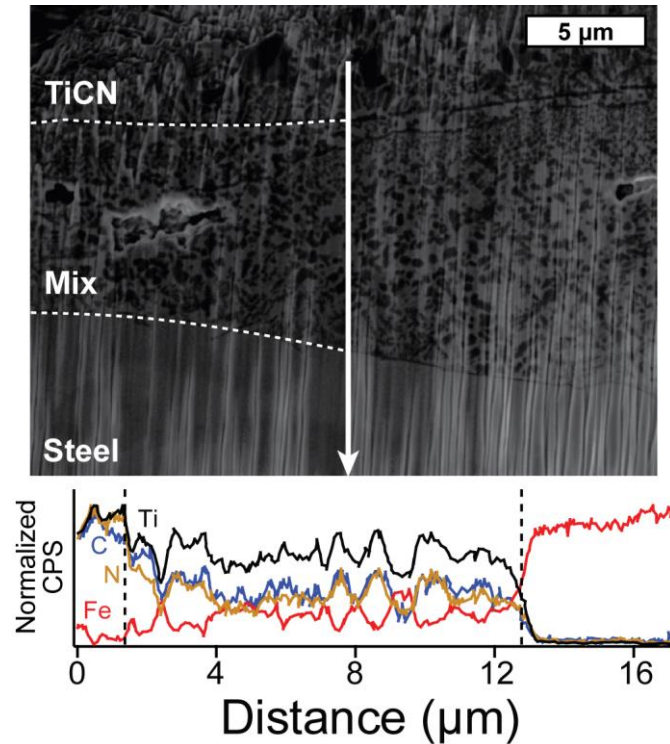


Figure 5.5: SEM cross-section for TiCN with linescan EDX. The white dashed line in the SEM image represents the WC coating-substrate interface. The red line plots relative Fe concentration in counts-per-second (CPS) along the linescan, the black line plots the relative Ti (CPS) along the linescan, the blue line plots the relative C (CPS) along the linescan, and the yellow line plots the relative N (CPS) along the linescan.

#### 5.4.3 TEM Investigation of the Interfaces in ESD-produced Coatings

Figure 5.6 summarized the transmission electron microscopy images of the interfaces produced by ESD method upon deposition of WC and TiCN coatings. The top images (Figure 5.6(a-b)) show the WC interface with 4140 series steel, and the bottom images (Figure 5.6(c-d)) show the TiCN-coated sample. The images on the right are higher magnification of the images presented on the left side of the figure. For the WC in Figure 5.6(a-b), there are two distinct regions in the sample: the WC coating and the steel. Consistent with the SEM studies, these images confirm the

absence of voids at the interface or in the film. However, the higher spatial resolution of TEM allows for the observation of the granular structure of the coating and the darker spots imbedded into the steel substrate, as indicated in the figure. EDX measurement on these spots suggests that they are pockets of W-containing material (most likely tungsten carbide), likely produced during transport of material from the electrode to the molten pool [210].

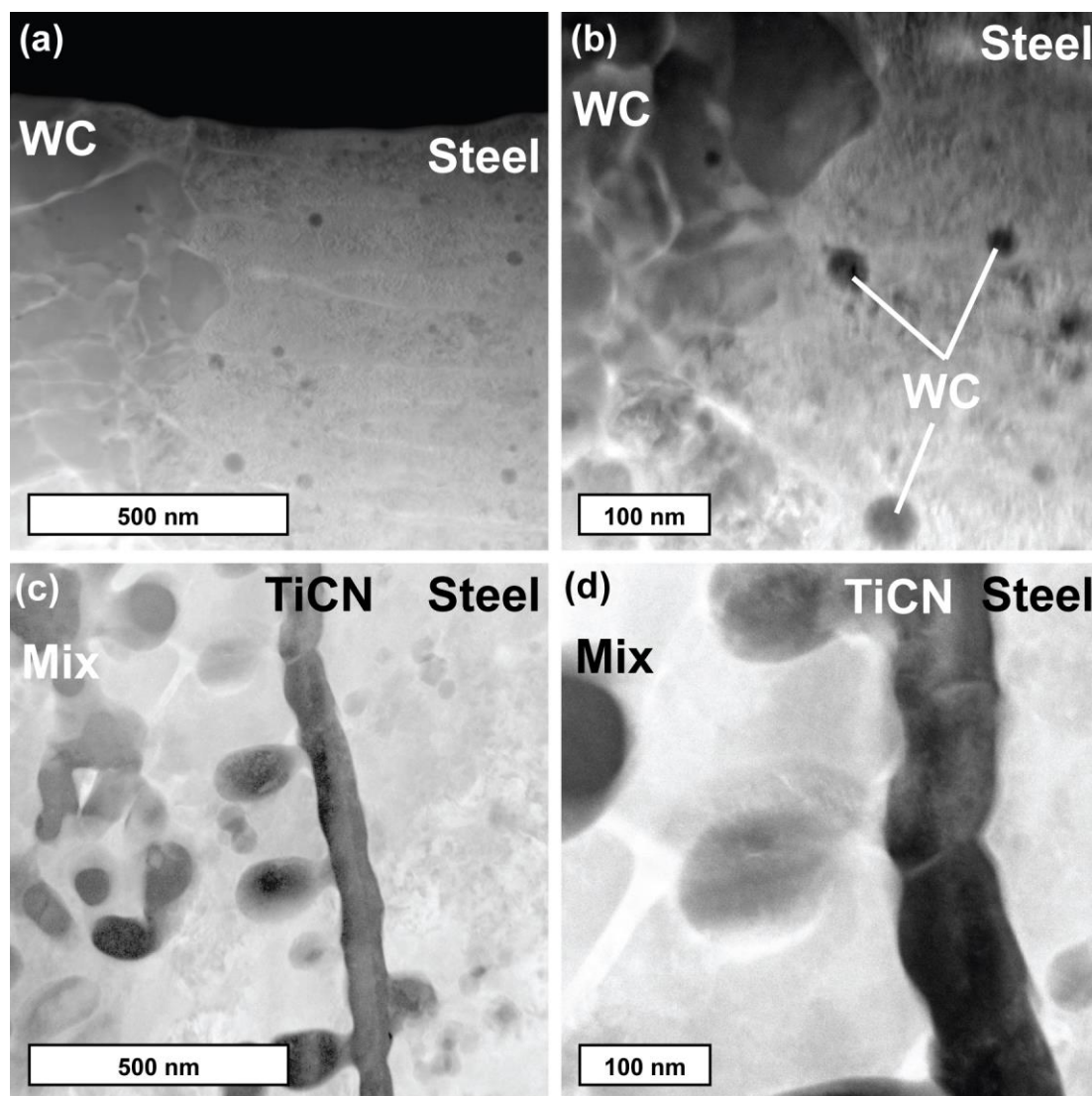


Figure 5.6: TEM images of (a-b) WC and (c-d) TiCN coatings deposited by ESD. The images on the left show the general area of the interface while the images on the right show a high magnification zoom-in.

In the TiCN TEM images in Figure 5.6(c-d), the same complexity as in the SEM investigation presented above is observed. The 4140 steel substrate is depicted on the right side of both images. At the interface of the steel substrate and the coating, a strip of approximately 100 nm wide corresponds to pure TiCN (as seen in the SEM

images). The interface between the TiCN coating and the steel substrate is clean and there are no discernible voids, which suggests that the interface formed is nearly perfect. To the left of this TiCN strip, the coating becomes a mixture of steel and TiCN components. This observation is in a complete agreement with the larger scale SEM results for the TiCN/steel interface.

It is interesting to emphasize again that the interfaces between 4140 steel and the coatings produced by ESD method are very different for TiCN and for WC. The TiCN coating has a mixed layer of TiCN and steel while the WC coating has an abrupt interface where the steel contribution (as signified by the presence of iron) is reduced to zero very quickly. This likely could be explained by the differences in melting point for WC and TiCN, which was explained in section 5.4.2.

#### **5.4.4 Crystalline Structure of the ESD Coatings, Interfaces, and Substrate**

The X-ray diffraction measurements for the WC and TiCN ESD coatings as well as TiCN electrode are summarized in Figure 5.7. In Figure 5.7(a) a bare 4140 steel spectrum is used for comparison. The three main peaks in Figure 5.7(a) belong to  $\alpha$ -Fe phase in the steel [211]. In Figure 5.7(b-c), the WC and TiCN ESD coatings' spectra are shown, respectively. Compared to the spectrum of the original 4140 steel in Figure 5.7(a), the spectra of the coatings are dominated by the characteristic features of  $\gamma$ -Fe phase [211]. The presence of this  $\gamma$ -Fe phase suggests that the ESD process leads to the modification of the steel phase. The electrospark process is characterized by a high current and short pulse that transmits little heat to the bulk substrate but imparts high temperature to a localized region. Because  $\gamma$ -Fe cannot be obtained at temperatures under 723°C and electrospark deposition uses sufficient temperature to melt WC (melting point 2870°C), it is reasonable to expect that the

local temperature of the sample can indeed reach 723°C, which may be responsible for a phase change. In both Figure 5.7(b) and Figure 5.7(c), the presence of the characteristic features of the  $\alpha$ -Fe phase are also consistent with the notion that the ESD only leads to localized heating of the sample and that the underlying steel is not affected. Perhaps the most important conclusion resulting from this study is that the phase change during ESD may correspond to a number of changes in physical properties of the interface, which has to be considered for practical applications. According to the comparison of an XRD spectrum in Figure 5.7(e) for a TiCN electrode used in the ESD process and characteristic features of the TiCN-coated sample in Figures 7(c-d), the coating produced is fully consistent with the TiCN material structure [212]. Thus, TiCN coating is produced on a  $\gamma$ -Fe phase layer, which is formed during the ESD process on a surface of the 4140 steel characterized largely by the  $\alpha$ -Fe phase. This observation is also consistent with the microscopy studies summarized above. WC coatings are largely amorphous in this case and no clear indications of its crystallinity are observed. A part of the “halo” commonly reported for amorphous films [213] is observed for WC coating between 20° and 30° upon a detailed examination.

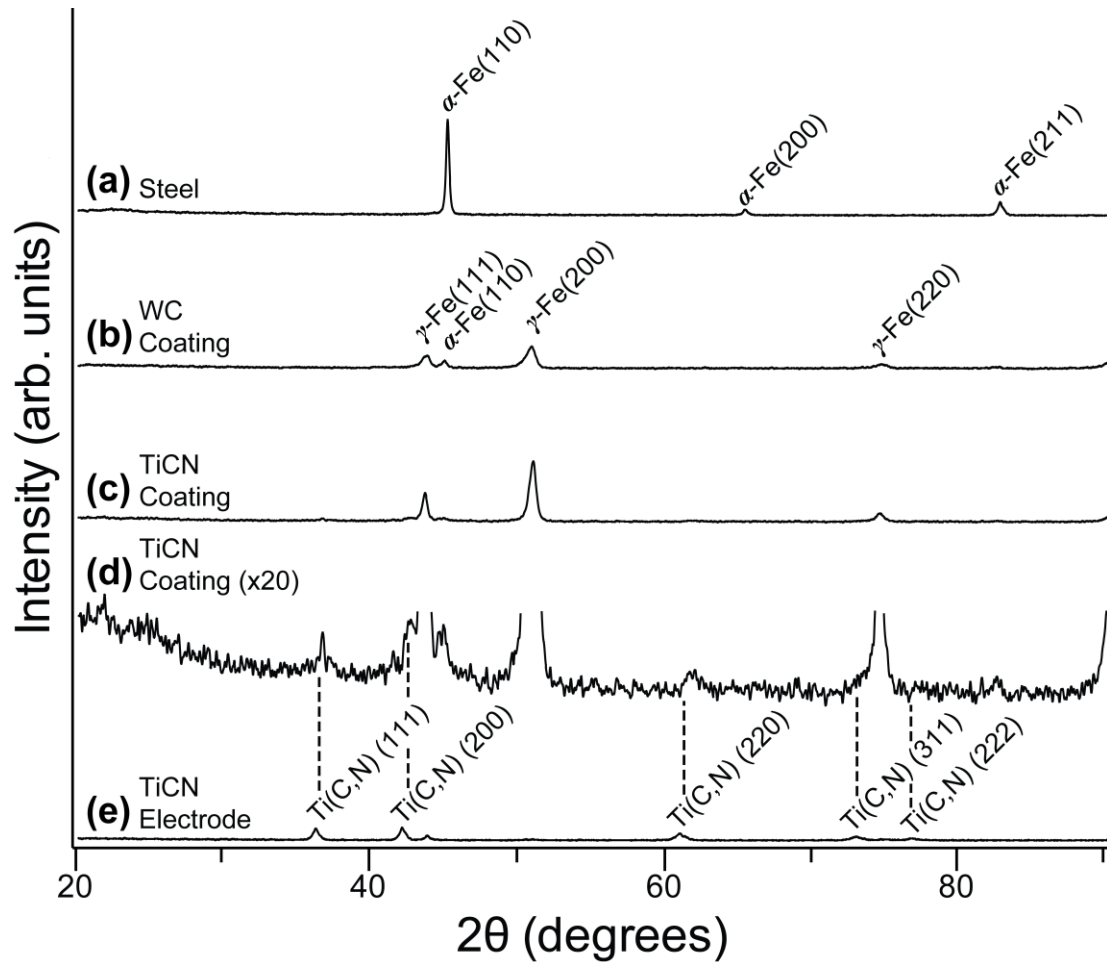


Figure 5.7: XRD investigation of (a) 4140 steel, (b) WC ESD coating on a 4140 steel coupon, (c) TiCN ESD coating on a 4140 steel coupon, (d) a zoom-in (x20) of the TiCN ESD coating on a 4140 steel coupon, (e) TiCN electrode used to deposit TiCN coating for a sample characterized in (c-d).

#### 5.4.5 Topography of the ESD Coatings' Surfaces

Some information about the surface structure and tribological properties are obtained based on the surface morphology. The nanoscale surface morphology was examined by AFM. The images in Figure 5.8 summarize these studies. Figure 5.8(a) illustrates the surface topography of the TiCN coating and Figure 5.8(b) displays the

surface topography of the WC coating. Both are set to the same depth scale (0 to 219.7 nm) for comparison. On this scale both surfaces appear to be very similar and overall the images are similar to those of uncoated polished steel seen in section 4.4.3. One noticeable difference between the two surfaces is roughness. The average roughness ( $R_A$ ) for the TiCN and WC coatings is 24.5 nm and 10.2 nm, respectively. The RMS roughness ( $R_{RMS}$ ) is 33.2 nm and 13.2 nm, respectively. These two roughness values are important to determine the Young's Modulus of the coatings for the same reason explained in section 3.4.5.

Overall, this experiment offers a glimpse at the nanostructuring of the surfaces produced. Compared to the structures of the films of TiCN produced by CVD in Chapter 3, where the formation of nanostructures 20-25 nm in size was observed, the ESD-coated samples do not appear to exhibit any unusual nanostructures on their surfaces.

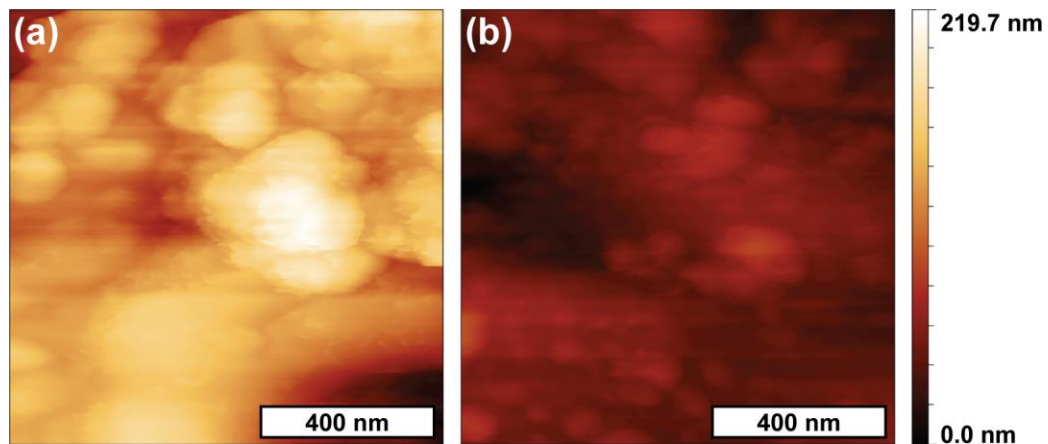


Figure 5.8: Representative 500 nm by 500 nm images of (a) TiCN and (b) WC coated samples. The common depth scale is given on the right. The scale bars are shown at the bottom of each image.

#### 5.4.6 Mechanical properties of ESD coatings

The microscopy and spectroscopy analysis above in sections 5.4.1-5 mostly focused on the quality of the interfaces produced by ESD of WC and TiCN on steel substrates. However, the ultimate goal of the approach is to produce a stable hard coating on steel. To compare structural integrity of the coatings and compare them to the substrate, a Hysitron TI 900 TriboIndenter™ was used to measure the Young's modulus of the coatings. Young's modulus is a measure of stiffness in an elastic material and it normally correlates well with other mechanical properties of coatings. It is compared with the previously measured Young's modulus determined by the same set-up for 4140 steel [133]. To measure the Young's moduli for both coatings, the surface roughness must be taken into account. This measurement is available through AFM studies presented above in section 5.4.5. The average roughness ( $R_A$ ) for the TiCN and WC coatings is 24.5 nm and 10.2 nm, respectively, while the RMS roughness ( $R_{RMS}$ ) is 33.2 nm and 13.2 nm, respectively. Based on this observation, measurements made for less than approximately  $5R_{RMS}$  in depth were discarded because surface effects affect substantially the obtained value. Table 1 summarizes the measured experimental values and relevant literature data.

Table 5.1: Young's modulus of ESD-deposited TiCN, WC and substrate steel, GPa.

Sample	Literature	Experimental
Steel	210 [214]	$259 \pm 32$
ESD-TiCN	467-510 [215]	$465 \pm 91$
ESD-WC	200-600 [178, 216]	$466 \pm 118$

Compared to the steel substrate, the Young's moduli for the TiCN and WC were much greater and also agree very well with intervals reported previously [178, 215, 216]. Because the coatings were sufficiently thick, no substrate effects were

expected to be observed, and no effects were calculated to account for those. The most important observation is that for both TiCN and WC coatings, the Young's moduli are very similar and further studies should focus on the interfaces produced between these coatings and substrate steel by different deposition methods.

## **5.5 Conclusions**

Two different coatings and interfaces formed upon their deposition by ESD onto steel substrate were examined and compared with those obtained by alternative deposition methods. Both a relatively common WC and much lesser understood TiCN films exhibited characteristic “splash” patterns when deposited by ESD. These patterns confirmed the metallurgical bond with underlying substrate. SEM and TEM examined the interfaces between the coatings and underlying steel, and this study suggested that the WC forms a very well-defined and smooth interface free of voids and impurities; however, inclusion of WC droplets into the steel was observed. The interface between TiCN and 4140 series steel was also free of voids and impurities but during ESD procedure a transition layer of intermixed TiCN and steel was observed, several microns in thickness. These differences were explained by different melting points of TiCN compared to WC. The stiffness of the ESD-deposited TiCN and WC coatings was estimated by measuring their Young's moduli. The Young's modulus values were very similar for the two coatings and substantially higher than that of the underlying steel substrate, yet lower than the value measured for the CVD coating in Chapter 4.

ESD is a method for deposition of TiCN and WC coatings that is suitable for practical applications and produces hard coatings with impurity- and void-free

interfaces. Further studies are needed to investigate the physical properties of these coatings and interfaces produced.

## Chapter 6

### NOVEL NANOPARTICLE DEPOSITION TECHNIQUE USING “CLICK CHEMISTRY”

#### 6.1 Abstract

In this chapter, a novel deposition procedure is developed to chemically attach functionalized nanoparticles to a gold surface. Fundamentally similar to previously known atomic and molecular layer deposition processes, this nanoparticle layer deposition approach uses efficient chemical functionalization of the solid substrate material and complementary functionalization of nanoparticles to produce a nearly 100% coverage of these nanoparticles with the use of copper-catalyzed “click chemistry”. Following this initial nanoparticle deposition, a second and third layer of nanoparticles is deposited. This layer-by-layer growth is demonstrated to produce stable covalently bound multilayers of nearly perfect structure over macroscopic solid substrates as confirmed by spectroscopic and microscopic studies.

#### 6.2 Introduction

A very versatile type of reaction is “click chemistry” [217, 218]. One common type of this cycloaddition process is based on the reaction between azide and alkyne functional groups to form triazole rings. Due to fast rate and high selectivity, “click reactions” have been applied in a number of fields, including drug delivery [218-220], and polymer and material science [221-223]. Recently, we have shown a “click chemistry” reaction between iron nanoparticles functionalized with either azide and

alkyne termination [79]. The main purpose of the experiment was to show that the magnetic properties of the iron nanoparticles, although diminished, remain after “click chemistry” (for future use with other materials). However, one result that must be noted from that experiment is that the morphology of the nanoparticles changed after “click chemistry”. This effect is seen in Figure 6.1. In Figures 6.1(a,c), low (50K) and high magnification (200K), respectively, of the iron nanoparticles are seen. Even though there was a wide size distribution of iron nanoparticles that averaged 25 nm in diameter, we see the individual nanoparticles before the “click chemistry”. After the “click chemistry” reaction, seen in Figures 6.1(b,d) (again low (50K) and high magnification (200K), respectively), the morphology of the iron nanoparticles differed substantially; that is, the average size of the clustered nanoparticle features increased to approximately 100 nm.

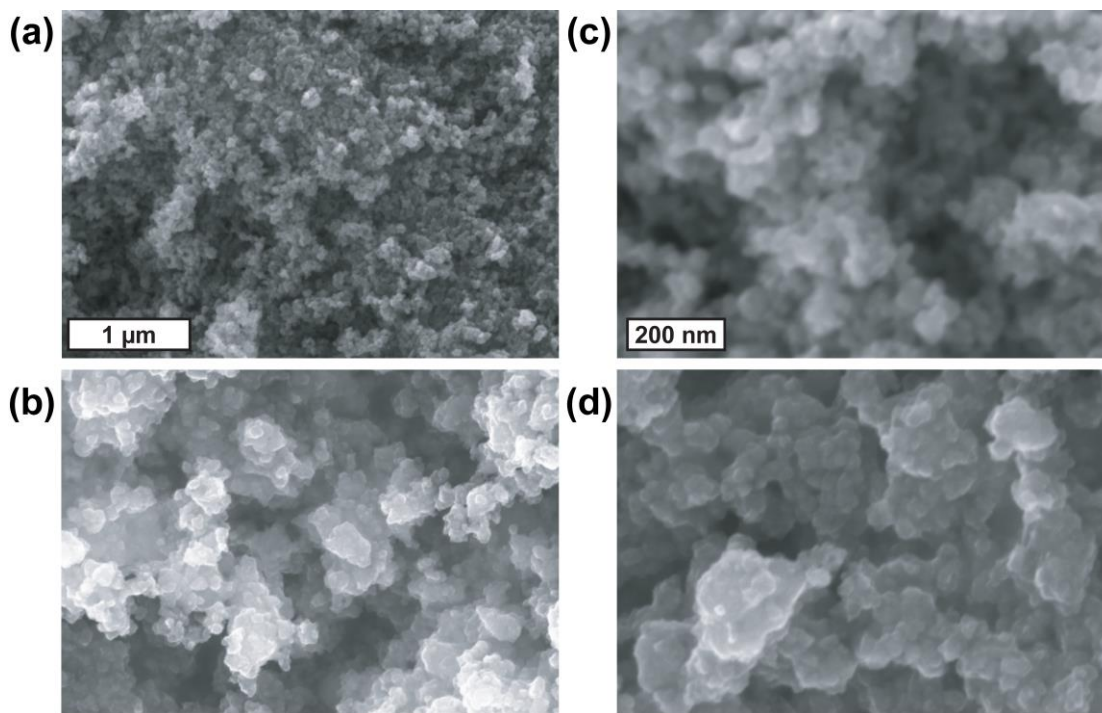


Figure 6.1: Morphological changes after “click chemistry” of functionalized nanoparticles. Figures (a,c) show non-functionalized iron nanoparticles at low and high magnification, respectively. Figures (b,d) show the iron nanoparticles after “click chemistry”. Figures (a) and (b) are at the same magnification (50K), and (c) and (d) are at the same magnification (200K). Figure adapted from reference [79].

As mentioned in section 1.4, the reason that we see the morphological change is the “click chemistry” that occurs over a three-dimensional space because the functionalization covers completely each nanoparticle. We could further enhance the applications by chemically attaching a functionalized nanoparticle to a functionalized surface. This could lead to a very high coverage with fast deposition time. We could then use this sample and deposit another layer onto the surface using nanoparticles that are functionalized with a complementary chemical group. Figure 6.2 illustrates a schematic of this procedure. This nanoparticle layer deposition (NPLD) growth has

applications in heterogeneous catalysis [81, 82], magnetic materials [83, 84], solar-energy conversion with photoelectrochemical cells [85, 86] and many more. Further, a sample like this could have be a “rebar” backbone for protective coatings. However, not much research has been performed on tethering nanoparticles to the surface through “click chemistry”, although there has been research on nanoparticle growth. For a monolayer formation, Toulemon et al. reported that the magnetic iron oxide nanoparticles could be assembled on a solid substrate through “click chemistry” to form a single layer [224, 225]. Atomic layer deposition has also been shown to strengthen the preassembled layers of nanoparticles in the course of a chemical reaction [226]. However, *chemical* assembly of inorganic nanoparticles to form a multilayer system has yet to be demonstrated.

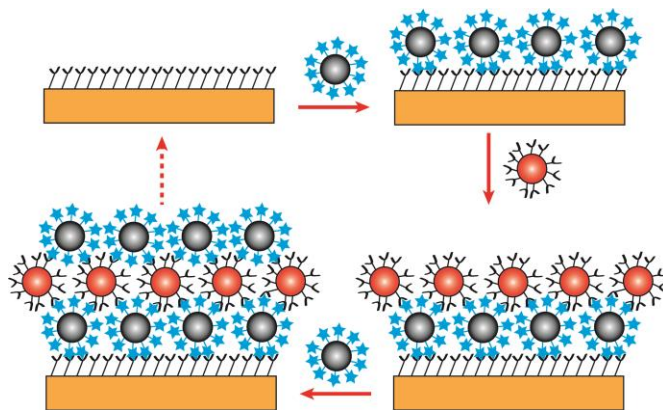


Figure 6.2: Basic scheme of layer-by-layer (LbL) nanoparticle deposition. After the surface is modified with an azide-terminated layer, an alkyne functionalized 80 nm nanoparticle reacts with the surface. The subsequent alkyne-terminated reacts with azide functionalized 50 nm particles. This cycle could theoretically repeat endlessly for the LbL deposition.

The formation of layers of nanoparticles covalently bound to a solid support in a self-limited surface process that utilizes “click chemistry” based on a reaction between azide and alkyne functionalities is described. This general approach can be utilized to form continuous layers consisting of nanoparticles of nanometers to microns in size, made of a variety of materials, and constructed in a variety of shapes. Most importantly, compared to other currently used techniques for construction of relatively thick layers, the proposed process should lead to a conformal filling of intricate features.

This is not a process of self-assembly, but rather a chemically driven self-limiting process. The formation of the first stable layer with high coverage is the first task. Then, a nearly perfect layer is used as a platform for nanoparticle layer deposition of silica nanoparticles of different sizes to form a continuous stable layered film. It should be emphasized that this process is fundamentally different from what is known as layer-by-layer (LbL), where polymer layers [227, 228], polyelectrolytes [229], nanoparticle-incorporated materials [230, 231], and supramolecular thin films [232] are deposited based on a continuous polymer film formed by a variety of deposition methods. Although useful in various applications, these approaches normally involve polymers or fibers as alternate layers, meaning that conformal filling with such processes is nearly impossible. The proposed NPLD process relies on a chemical property of a single nanoparticle as a building block for layered structures. The process is demonstrated for deposition of silica nanoparticles because this material is well known, cheap, easily modified, and nanoparticles with very narrow size distribution that can be purchased from a commercial source. However, in the

future, a variety of materials and size distribution could be used for realistic applications.

### **6.3 Experimental Procedure**

#### **6.3.1 Sample Preparation**

The nanoparticle layer deposition (NPLD) is based on application of a copper-catalyzed “click” reaction between azide and alkyne functional groups to form the triazole ring in a cycloaddition process. The detailed procedure for this NPLD process is found in section 2.2.4. This procedure describes the gold surface functionalization as well as the nanoparticle functionalization and deposition. Alternating nanoparticles were deposited in the NPLD fashion. To demonstrate the feasibility of such an approach, the nanoparticle growth is performed using silica particles of different sizes with very narrow size distributions, so that the completion and quality of the layers are monitored straightforwardly with spectroscopic and microscopic analytical techniques.

#### **6.3.2 Surface Characterization**

Each step of the modification with the functionalized nanoparticles was explored with single-point attenuated total reflectance Fourier-transform infrared spectroscopy (ATR FT-IR), X-ray photoelectron spectroscopy (XPS), and scanning electron microscopy (SEM). Some of these experimental results are compared to and confirmed by density functional theory (DFT) calculations.

## 6.4 Results and Discussion

### 6.4.1 Proof of Chemical Reactions in NPLD

Single-point ATR FT-IR was first used to prove chemical attachment of nanoparticles to the azide-terminated gold surface. Figure 6.3 plots the informative regions of these infrared data. All spectra are referenced to a gold substrate sonically cleaned with ethanol. Figure 6.3(a) shows the infrared data of azide-terminated gold surface. An intense peak observed at  $2090\text{ cm}^{-1}$  is fully consistent with the stretching of the azide functional group for the 11-azidoundecanethiol on gold substrate [95]. At the same time, symmetric and asymmetric  $\text{CH}_2$  stretching peaks are observed at  $2850\text{ cm}^{-1}$  and  $2923\text{ cm}^{-1}$ , respectively. These peaks are indicative of an ordered system [93, 127, 129, 233]. Figure 6.3(b) shows the infrared spectrum collected following the deposition of the first layer of nanoparticles. Here, the azide peak is removed because the terminating layer is the alkyne-terminated nanoparticles after deposition. The symmetric and asymmetric  $\text{CH}_2$  stretches are still present at  $2854\text{ cm}^{-1}$  and  $2923\text{ cm}^{-1}$ , which are indicative of a slightly disordered system [93, 127, 129, 233, 234]. This is expected because the alkyne-termination of functionalized nanoparticles is no longer completely ordered. That is, the geometry of the nanoparticle makes its functionalization with a SAM result in a disordered molecular layer. In addition, the disorder of the alkyl chains in the molecular functionalized layers likely originates from a relatively short alkyl chain, although the alkyne termination could be used to react further with azide-terminated silica nanoparticles.

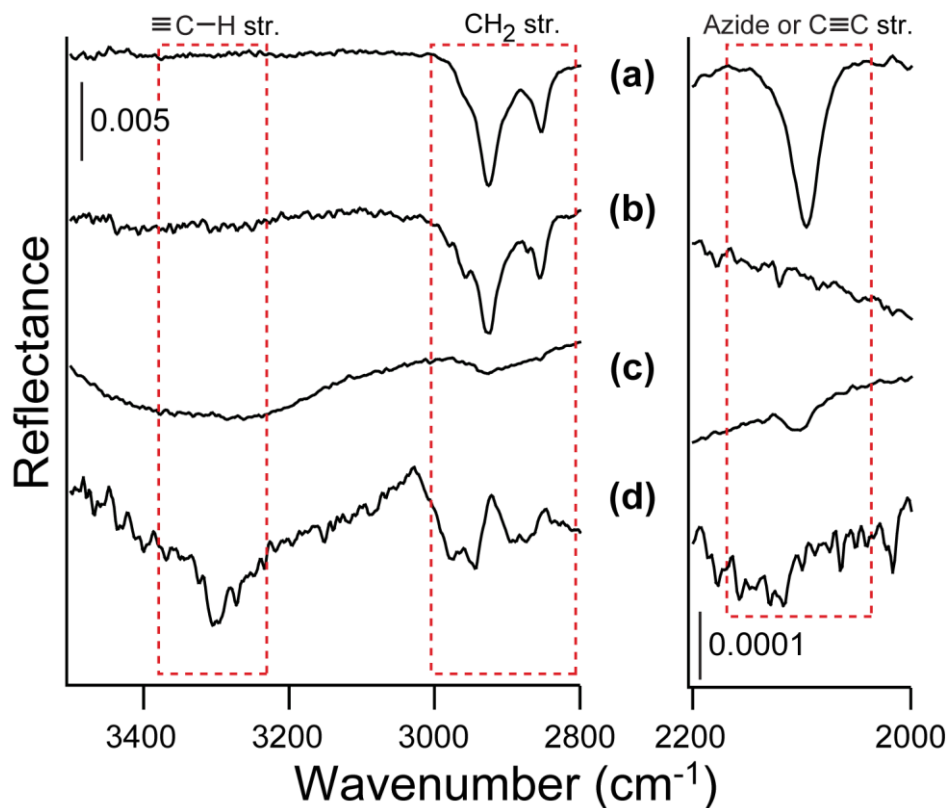


Figure 6.3: ATR FT-IR spectra of (a) 11-azidoundecanethiol modified Au substrate; (b) 80-nm alkyne functionalized nanoparticles deposited onto sample (a); (c) 50-nm azide functionalized nanoparticles deposited on sample (b); and (d) 80-nm alkyne functionalized nanoparticles deposited on sample (c).

Figure 6.3(c) shows the deposition of azide-terminated nanoparticles onto the alkyne-terminated nanoparticles of the first layer. We see the reemergence of the azide-stretching peak at  $2100\text{ cm}^{-1}$ . Likewise, the reduction in the symmetric and asymmetric  $\text{CH}_2$  ordered peaks and the increased broadness signify that the system is much less ordered than before. Again, this result is expected because the short alkyl chain is used for nanoparticle functionalization. Figure 6.4(d) shows the second layer deposition of the alkyne-terminated nanoparticles onto the azide-terminated

nanoparticle surface. The absence of the azide peak is again expected because the top layer is now alkyne-terminated and no azide is expected to be present near the top of the surface region. In the CH<sub>2</sub> stretching region, the shift in wavenumber suggests that there is a very high disorder in the system. There is also a peak present at 3295 cm<sup>-1</sup>, which is the alkyne C-H stretching peak. The presence of this peak is indicative of the alkyne termination of the deposited nanoparticles on the surface. That this peak is not present on the first alkyne-terminated nanoparticle layer does not mean that the nanoparticles were not deposited. A combination of techniques is used for proof of the nanoparticle deposition, and in this case, we use XPS and SEM studies.

The X-ray photoelectron spectroscopic studies summarized in Figure 6.4 also show evidence of the chemical attachment of the nanoparticles through “click chemistry”. All of the peaks were calibrated to the Au 4f<sub>7/2</sub> peak at 83.8 eV unlike in previous chapters, because the alkyne functionality is present in some samples and would influence C 1s peak position. Figures 6.4(a,e) show the azide-terminated gold surface for the C 1s and N 1s, regions respectively. In the C 1s region, there is a large peak at 284.6 eV with two small peaks at 286.0 eV and 288.5 eV. As previously mentioned, the peaks at 284.6 eV, 286.0 eV, and 288.5 eV are assigned to C-C bonds [121, 122], C-N/C-O bonds [49, 92], and C=O bonds [49, 92, 123], respectively. The oxidized species are present, because the samples were transported through the air and adventitious carbon adsorbed on the sample. In the N 1s region, there are two features in the spectrum that can be deconvoluted to three peaks. These three peaks correspond to the three different types of nitrogen present in the sample. The three peaks located at 403.4 eV, 400.6 eV, and 400.0 eV correspond to the ***-N=N=N***, ***-N=N=N***, and ***-N=N=N*** (bolded and italicized) nitrogen species, respectively. These assignments

agree very well with the previous work on “click chemistry” with iron nanoparticles [79]. These two regions show that there is azide present on the surface that is a perfect starting point for further nanoparticle deposition with minimal oxidation.

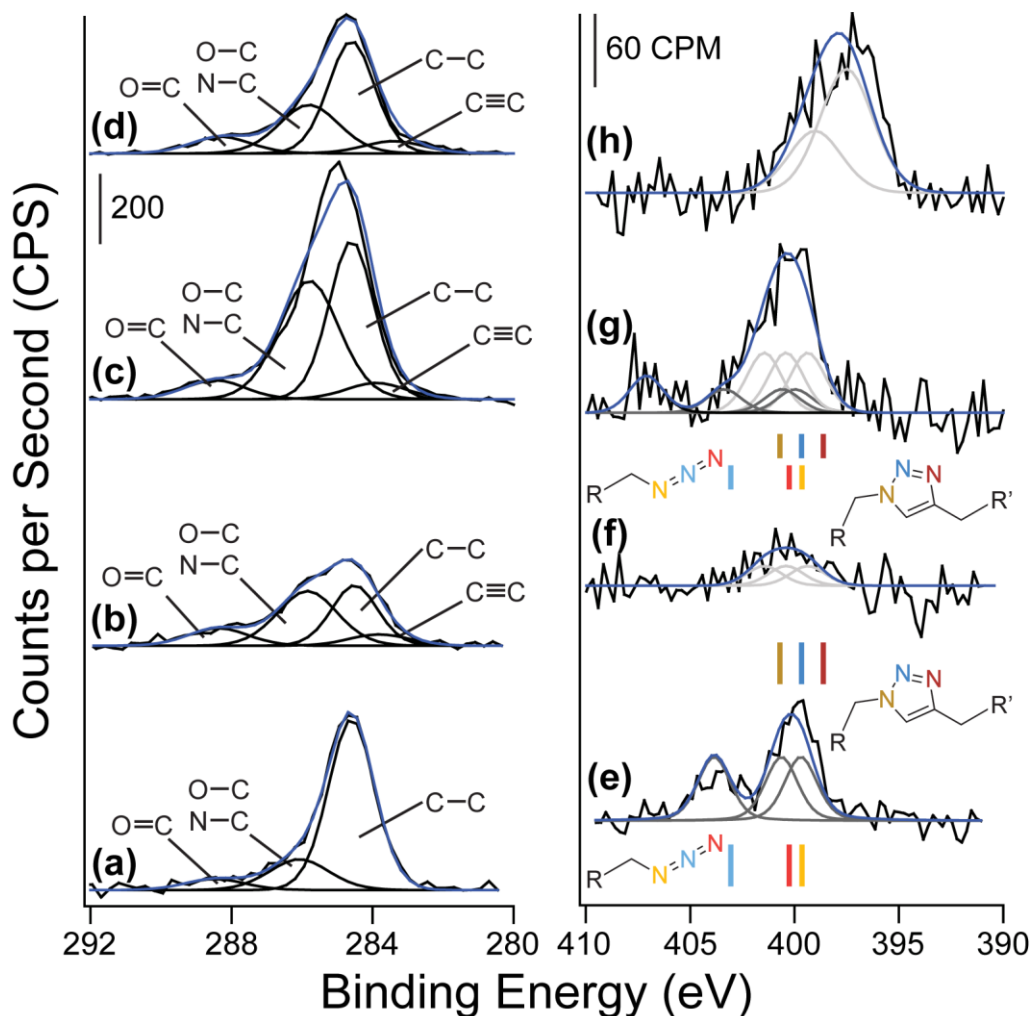


Figure 6.4: XPS studies of each layer of nanoparticle deposition. On the left is the C 1s region, and the right shows the N 1s region of: (a,e) the azide-terminated gold surface; (b,f) the alkyne 80-nm nanoparticle deposited onto azide-terminated gold surface; (c,g) the azide 50-nm nanoparticles deposited onto the first 80-nm nanoparticle layer; and (d,h) the second 80-nm alkyne nanoparticle layer on the 50-nm azide nanoparticle layer. The solid lines in the N 1s region show to the predicted energy shifts from DFT calculations. The colors of each bar correspond with the colors of the model, and the lighter lines show the azide information while the darker lines provide information for the triazole ring compound.

Figures 6.4(b,f) show the C 1s and N 1s spectral regions following the first layer deposition of the 80-nm alkyne-terminated nanoparticles onto the azide-terminated surface, respectively. There are peaks at 284.6 eV, 286.0 eV, and 288.5 eV, which have been assigned in previous sections and chapters. There is also an additional peak at 284.0 eV, which may correspond to the C≡C of the alkyne as well as the C=C of the triazole ring. In the N 1s region, as before, there are three peaks, but they have changed positions. These peaks are present at 401.5 eV, 400.4 eV, and 399.4 eV, and are assigned to the  $-C-N-N-$ ,  $-N-N=N-$ , and  $-N=N-C-$  nitrogen atoms, respectively. There is also the possibility that azide may be present (with incomplete nanoparticle coverage), but the absence of the peak at 403.4 eV suggests that this is not the case. Again, this result is quite similar to the iron nanoparticle “click chemistry” study, in which the peaks appeared to combine to form a broad feature. These spectra show that there is complete nanoparticle deposition, and this sample is an acceptable starting point for the next nanoparticle layer deposition.

Figures 6.4(c,g) show the C 1s and N 1s regions following deposition of the 50-nm azide-terminated nanoparticles onto the first 80-nm alkyne-terminated nanoparticle layer, respectively. As before, the peaks at 284.0 eV, 284.6 eV, 286.0 eV, and 288.5 eV in the C 1s region correspond to the same features of the spectrum discussed in the previous sections and chapters. In the N 1s region, there are now broad features that can be fitted with 7 peaks. The peak at 407.1 eV corresponds to the oxidized nitrogen species. Expected because the sample is transported to the XPS chamber in ambient conditions. The other 6 peaks are perfectly aligned with the results in Figures 6.4(e-f). This consistency is expected because this layer should be a combination of the previous layers; that is, this layer should have the terminated azide

functionality (peaks at 403.4 eV, 400.6 eV, and 400.0 eV) in addition to containing the triazole ring obtained through the “click chemistry” (peaks at 401.5 eV, 400.4 eV, and 399.4 eV). The peak assignments are the same as in the previous section. The XPS spectra show that the “click chemistry” is an excellent method to deposit the nanoparticles layer by layer.

#### **6.4.2 Surface Coverage and Microscopy Studies**

Scanning electron microscopy (SEM) imaging was performed to follow the physical adsorption process and chemical attachment of silica nanoparticles to the gold substrate to determine the surface coverage. Additional studies with a focused ion beam (FIB) to etch and polish the samples determined the thickness of the samples. These results are summarized in Figure 6.5. In Figure 6.5(a), the plane view of the first layer of 80-nm alkyne-terminated nanoparticle is shown. The coverage of the first layer is calculated to be 87.2% based on the absolute maximum number of particles of this size that could fit onto a flat surface, which is excellent even compared to a single cycle of ALD [235]. It has to be emphasized that the silica nanoparticles were not deposited through the self-assembly process; they were randomly reacting with the surface to form covalent linkages. Thus, this coverage is extremely high and the reaction is very efficient. Figure 6.5(b) shows the cross sectional view of the nanoparticle deposition. In this view, one sees (from bottom to top) the silicon substrate, a thin gold layer, and the single layer of SiO<sub>2</sub> nanoparticles. This height is what is expected for a single layer.

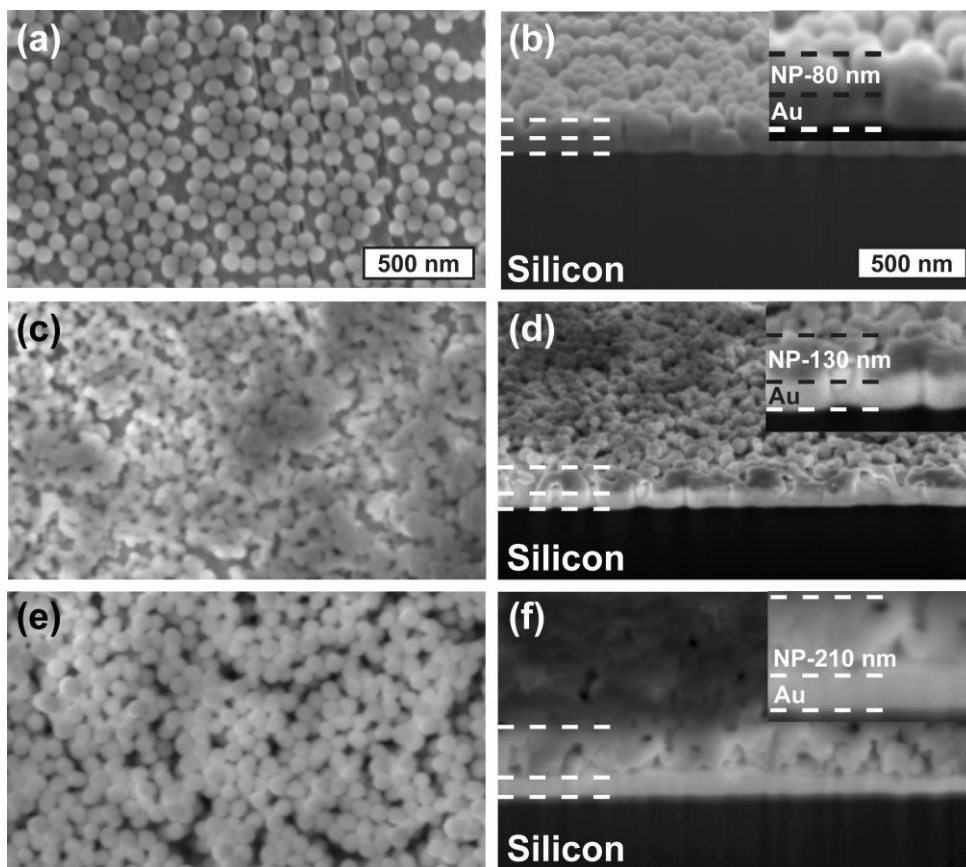


Figure 6.5: SEM studies to determine the surface coverage and film thickness. The figure shows: (a) the 80-nm alkyne nanoparticle-deposited layer surface (plane view); (b) the cross sectional view 80-nm alkyne nanoparticle layer; (c) the 50-nm azide nanoparticle deposited layer surface (plane view) deposited on top of the first layer; (d) the cross sectional view of 50-nm azide nanoparticles layer deposited on top of the first layer; (e) the second 80-nm alkyne nanoparticle deposited layer surface (third overall layer, plane view); and (f) the second cross sectional view of the three-layer system.

Following the deposition of the first layer of 80-nm alkyne functionalized nanoparticles, the second layer was chosen to be based on 50-nm nanoparticles functionalized to have azide termination, as shown in Figures 6.5(c-d). Such a difference in size allows a simple verification of the deposition process and the

completeness of the formation of the second layer by SEM. As shown in Figure 6.5(c), the nearly complete second layer of 50 nm silica nanoparticles is formed on a top of the first layer, and the bilayer system is just as stable as the first monolayer. In Figure 6.5(d), the thickness of the bilayer shown in Figure 6.5(c) is 130 nm, which is fully consistent with depositing the second layer of 50 nm nanoparticles on top of a layer of 80 nm nanoparticles. Because the sizes of the nanoparticles within the first layer are larger than those of the second layer, and because the attachment is driven by a chemical reaction rather than self-assembly, the deposition process does not lead to any specific packing of the second layer.

The same approach was tested to produce the third layer with 80-nm alkyne-terminated nanoparticles and led to a successful high-coverage layer formation shown in Figure 6.5(e-f). Figure 6.5(e) shows a surface (plan) view with high coverage and Figure 6.5(f) demonstrates that the thickness of the 3-layer system reaches 210 nm, which is what would be expected for a layer of 50 nm nanoparticles sandwiched between two layers of 80 nm nanoparticles. In all of these studies, the nanoparticle monolayer and multilayers formed through “click chemistry” are very stable. Washing with any combination of the standard solvents or sonication in ethanol did not remove any particles and did not affect the coverage of this first layer.

It has to be mentioned that a number of experiments with nanoparticles without complementary chemical functionalities lead to physisorption akin to the SEM results demonstrated in Figure 6.5, where the physisorbed particles could be easily removed by solvents or by sonication. Only the formation of strong chemical bonds through the triazole ring keeps the multilayer system stable. To show this behavior, two control experiments were performed: (1) to show the importance of the complementary

chemistry, and (2) to show the stable nature of the triazole ring. These control experiments are summarized in Figure 6.6.

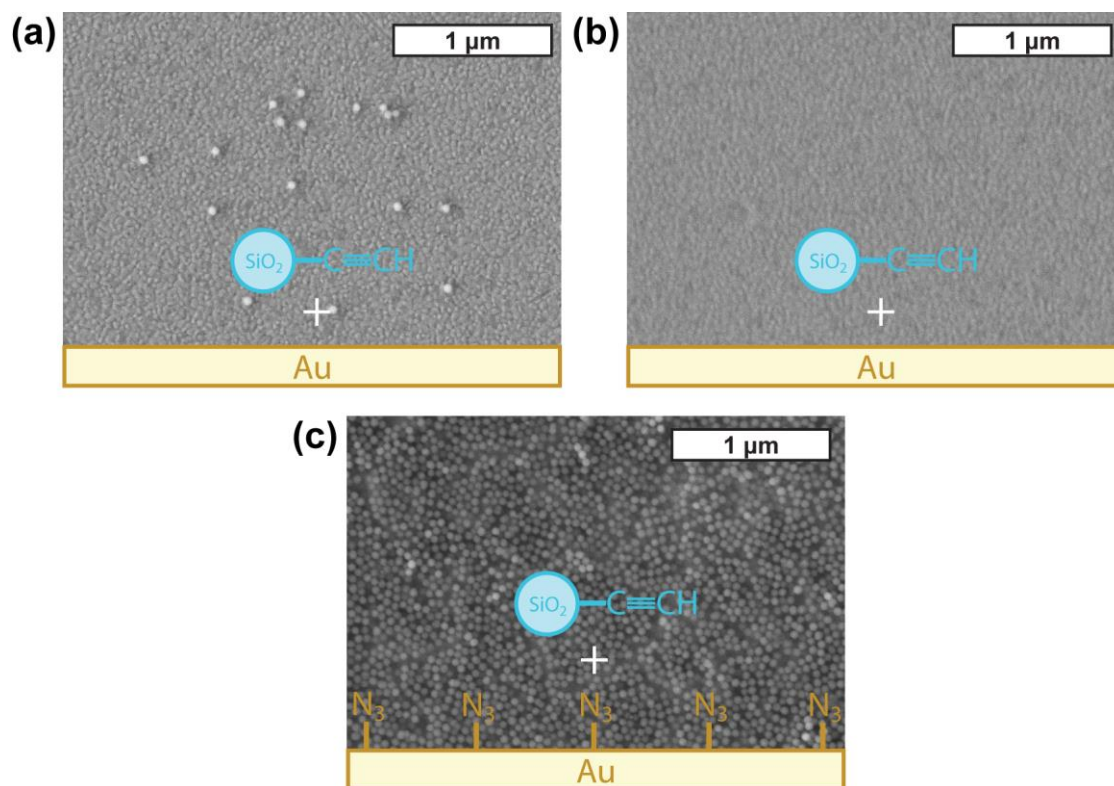


Figure 6.6: Control experiments to show the importance of the complementary chemistry and the stable nature of the triazole ring. The figure shows (a) the same procedure for first layer nanoparticle deposition sans for azide termination of the gold substrate and washing; (b) the same procedure for first layer nanoparticle deposition sans for azide termination of the gold substrate; and (c) the procedure as written (for reference).

For physical adsorption of silica nanoparticles, a small number of nanoparticles was observed on the surface, as shown in Figure 6.6(a); however, after washing and sonication, a pristine surface without any nanoparticles is observed, as demonstrated in

Figure 6.6(b). When compared to the procedure outlined in section 2.2.4, it is evident that there is a need for chemical attachment through the “click” reaction. The nanoparticle monolayer and multilayers formed by this method are very stable with respect to washing with standard solvents and sonication.

## 6.5 Conclusions

A new deposition scheme for multilayer systems of nanoparticles on solid substrates is proposed and tested: nanoparticle layer deposition based on “click” reaction stimulated by sonication. A nearly perfect high coverage of the first layer was formed by this approach using azide-functionalized gold substrate and azide-terminated silica nanoparticles. This deposition step leaves a sufficient number of azide groups to react further with alkyne-terminated silica nanoparticles to form a high-coverage second layer. The feasibility of continuing this process was tested for the third layer as well. This process of growth is fundamentally different from current layer-by-layer growth methods involving nanoparticles and has more in common with the molecular and atomic growth by MLD and ALD, respectively, making this approach an excellent method for growth of controlled layered systems with minimal organic contamination and with potentially high conformal filling. As the process is not driven by self-assembly, but rather by surface chemical reactions, this general approach opens a number of opportunities for three-dimensional design of architectures based on chemically driven attachment.

## Chapter 7

### SUMMARY AND FUTURE WORK

#### 7.1 Thin Films for Photovoltaic Applications

In this work, a silicon substrate was functionalized with 1-amino-10-undecene and reacted with [6,6]-phenyl-C<sub>61</sub>-butyric acid methyl ester (PCBM). Along each step of the process, the sample was interrogated through spectroscopic, microscopic, and computational techniques. Despite the similarity of kinetic and thermodynamic parameters predicted computationally for two competing chemical pathways for the attachment process, where one pathway was through the PCBM ester (**Structure 1**) and the second was through the reaction of the PCBM C<sub>60</sub> cage (**Structure 2**), the experimental results suggest that the reaction took place predominantly directly through the C<sub>60</sub> cage. The XPS results confirmed that a reaction occurred and PCBM is present on the surface. This was shown by the presence the  $\pi$ - $\pi^*$  shake-up in the C 1s region, and the slight shift in binding energy for the main peak in the N 1s region. The AFM measurements showed that the PCBM attached to the surface without large clusters forming more than one molecule high. Infrared spectroscopic measurements indicated the lack of a shift in the C=O stretching frequency, meaning that there was no change of the chemical environment of the carbonyl group. ToF-SIMS analysis suggested that the nitrogen is directly attached to the C<sub>60</sub> cage following surface reaction and the continued presence of the OCH<sub>3</sub><sup>-</sup> peak (which would be removed if **Structure 1** were the dominant product) indicated the dominance of Structure 2. The formation of **Structure 2** (final structure through C<sub>60</sub>) over **Structure 1** (final

structure through ester to form amide) is due to the fact that there are multiple reaction sites through the C<sub>60</sub> cage compared to the single ester per PCBM molecule.

The understanding of competing chemistries is essential for further studies of PCBM reacted with functionalized solid surfaces via the amino functionality. This work has potential applications in organic photovoltaic devices. If a photovoltaic application requires tethering of a PCBM molecule (say for an ordered heterojunction formation), this work suggests novel ways in which such instruments may be designed to carry out the process.

## **7.2 Thin Film TiCN Protective Coating for Perfect Deposition**

In this work, a thin protective titanium carbonitride (TiCN) coating was deposited onto a 4140 steel substrate through a common chemical vapor deposition precursor normally used for producing a diffusion barrier in microelectronics. The thin films were deposited under both HV and UHV conditions. Although there was a difference in vacuum level, both depositions led to coatings with similar properties. Before exposure to the atmosphere, AES showed that the coatings were comprised of titanium, carbon, and nitrogen, while after exposure to ambient conditions the film became partially oxidized. ToF-SIMS analysis demonstrated that the coating was uniform throughout and suggested that the TiCN-steel interface was well defined. Likewise, the TEM images showed a sharp interface consistent with the ToF-SIMS measurements. The AFM measurement revealed the topography of the bare steel and TiCN coating. The surface of the TiCN-coated sample exhibited 25-30 nm nanostructures. The tribological measurements indicated that the Young's modulus of the TiCN coating was roughly 2.5 times greater than that of the 4140 steel. Overall, the coatings exhibited a well-defined interface and were uniform throughout.

This work is especially important to applications that require a thin film for protective applications. One aspect that must be investigated is how the TDMAT actually adheres or bonds to the steel substrate. No work has been performed on the mechanism, unlike the reaction of TDMAT and silicon surfaces, which leads to a formation of a very common diffusion barrier. The order of layers on the surface may play a roll in tribological properties. In other words, if a layer of TiC has been deposited before the TiCN, there may be interesting properties that the pure TiCN coating may not have. Likewise, the addition of various elements in the coating may enhance or degrade the protective aspect.

### **7.3 Thin Film TiCN Protective Coating by Practical Deposition Methods**

Because there are certain applications that are not conducive to vacuum deposition and the coatings must be deposited in the ambient environment, another technique must be used. In this work, a TiCN coating has been deposited on a 4140 steel substrate through electrospark deposition (ESD) and compared to a common WC ESD coating. In the SEM measurements, both the TiCN and WC ESD coatings exhibit “splash” patterning indicative of ESD coatings. SEM also suggests that the interface between the steel and the WC coating is very well-defined and free of voids and impurities, although TEM measurements demonstrate the formation of WC droplets in the steel. The TiCN and steel also exhibit a well-defined and void- and impurity-free interface, but display a several micron thick transitional layer between the pure TiCN and pure steel. The different interfaces are explained by the difference in melting points as well as the differences in specific heat capacity of these materials. The similar Young’s moduli suggest that the both coatings exhibit excellent mechanical

properties. Overall, ESD is a satisfactory method to produce void- and impurity-free protective coatings for practical applications.

This work forms an excellent basis for future ESD work. As previously stated, not much molecular-level work has been done on realistic TiCN coatings, and nitride coatings in particular. This work helps lay a foundation for future applications of ESD nitride and carbonitride coatings that can be compared. Also, additional work should be done to determine the corrosion properties of the TiCN coatings. Just as in the previous section, work should be done to investigate how different elements either enhance or diminish tribological and chemical properties of the coating.

#### **7.4 Novel Wet-Chemistry-Based Nanoparticle Deposition**

In this work, “click chemistry” was shown to deposit silica nanoparticles in a multilayer system with high coverage onto a gold substrate. Both spectroscopic and microscopic measurements were utilized to characterize the system. Infrared and XPS studies confirmed the chemical attachment of the functionalized nanoparticles to the complementary functionalized surface. The SEM images showed that there was nearly perfect nanoparticle layer coverage, and cross-sectional SEM studies indicated that each layer was of the expected thickness. Subsequent control experiments indicated that the nanoparticle deposition on the surface was chemical in nature rather than a physical deposition. The relatively high deposition rate compared to molecular layer deposition and atomic layer deposition techniques makes this an attractive strategy for controlled three-dimensional nanoparticle deposition.

In the future, it would be interesting to look at different substrates and different deposition materials. One direction that will be taken is the deposition of magnetic

nanoparticles on a nonmagnetic surface. Three-dimensional surfaces (i.e. not flat) will be at the focus of several future studies in the group.

## **7.5 Overall Conclusions**

Throughout the the thesis, different surface and interfacial systems have been investigated. All projects are related to the molecular understanding of surfaces and interfaces, and each has brought its own challenges and difficulties. Fundamental and/or field-relevant research was conducted to improve upon points that were previously not understood. This work will be continued by current or future members of the Teplyakov research group.

## REFERENCES

1. Levitin, G., Hess, D.W., Surface Reactions in Microelectronics Process Technology, in: Prausnitz, J.M. (Ed.) Annual Review of Chemical and Biomolecular Engineering, Vol 2, 2011, pp. 299-324.
2. Arya, S.K., Saha, S., Ramirez-Vick, J.E., Gupta, V., Bhansali, S., Singh, S.P., *Anal. Chim. Acta*, **2012**, 737, 1-21.
3. Choy, K.L., *Prog. Mater. Sci.*, **2003**, 48, 57-170.
4. Gao, Y.L., *Mater. Sci. Eng. R-Rep.*, **2010**, 68, 39-87.
5. Nemet, G.F., Kammen, D.M., *Energy Policy*, **2007**, 35, 746-755.
6. Mishra, A., Bauerle, P., *Angew. Chem., Int. Ed.*, **2012**, 51, 2020-2067.
7. Saidur, R., Islam, M.R., Rahim, N.A., Solangi, K.H., *Renew. Sust. Energ. Rev.*, **2010**, 14, 1744-1762.
8. Zarrouk, S.J., Moon, H., *Geothermics*, **2014**, 51, 142-153.
9. Liu, J., Thallapally, P.K., McGrail, B.P., Brown, D.R., Liu, J., *Chem. Soc. Rev.*, **2012**, 41, 2308-2322.
10. Wang, Y., Chen, K.S., Mishler, J., Cho, S.C., Adroher, X.C., *Appl. Energy*, **2011**, 88, 981-1007.
11. Kopyscinski, J., Schildhauer, T.J., Biollaz, S.M.A., *Fuel*, **2010**, 89, 1763-1783.
12. Abu-Khader, M.M., *Prog. Nucl. Energy*, **2009**, 51, 225-235.
13. Ahmaruzzaman, M., *Progr. Energy Combust. Sci.*, **2010**, 36, 327-363.
14. Nicot, J.P., Duncan, I.J., *Greenh. Gases, Sci. Tech.*, **2012**, 2, 352-368.
15. Mukerjee, S., Srinivasan, S., *J. Electroanal. Chem.*, **1993**, 357, 201-224.
16. Yin, Y., Alivisatos, A.P., *Nature*, **2005**, 437, 664-670.
17. Parmesan, C., Yohe, G., *Nature*, **2003**, 421, 37-42.

18. Broecker, W.S., *Science*, **1997**, *278*, 1582-1588.
19. Chapin, D.M., Fuller, C.S., Pearson, G.L., *J. Appl. Phys.*, **1954**, *25*, 676-677.
20. Goetzberger, A., Hebling, C., Schock, H.W., *Mater. Sci. Eng. R-Rep.*, **2003**, *40*, 1-46.
21. Zhao, J.H., Wang, A.H., Green, M.A., Ferrazza, F., *Appl. Phys. Lett.*, **1998**, *73*, 1991-1993.
22. Pizzini, S., *Sol. Energy Mater. Sol. Cells*, **2010**, *94*, 1528-1533.
23. Green, M.A., Emery, K., Hishikawa, Y., Warta, W., Dunlop, E.D., *Prog. Photovoltaics*, **2014**, *22*, 1-9.
24. Tang, C.W., *Appl. Phys. Lett.*, **1986**, *48*, 183-185.
25. Sun, S.-S., Sariciftci, N.S., *Organic Photovoltaics: Mechanisms, Materials, and Devices*, CRC Press, Boca Raton, FL, 2005.
26. Thompson, B.C., Frechet, J.M.J., *Angew. Chem.-Int. Edit.*, **2008**, *47*, 58-77.
27. Mayer, A.C., Scully, S.R., Hardin, B.E., Rowell, M.W., McGehee, M.D., *Mater. Today*, **2007**, *10*, 28-33.
28. Guralnick, B.W., Seppala, J.E., Mackay, M.E., *J. Polym. Sci. Pt. B-Polym. Phys.*, **2011**, *49*, 772-780.
29. Markov, D.E., Hummelen, J.C., Blom, P.W.M., Sieval, A.B., *Phys. Rev. B*, **2005**, *72*.
30. Peumans, P., Yakimov, A., Forrest, S.R., *J. Appl. Phys.*, **2003**, *93*, 3693-3723.
31. Scully, S.R., McGehee, M.D., *J. Appl. Phys.*, **2006**, *100*.
32. Liu, M., Johnston, M.B., Snaith, H.J., *Nature*, **2013**, *501*, 395-+.
33. Sariciftci, N.S., Smilowitz, L., Heeger, A.J., Wudl, F., *Science*, **1992**, *258*, 1474-1476.
34. Yu, G., Gao, J., Hummelen, J.C., Wudl, F., Heeger, A.J., *Science*, **1995**, *270*, 1789-1791.
35. Li, G., Shrotriya, V., Huang, J.S., Yao, Y., Moriarty, T., Emery, K., Yang, Y., *Nat. Mater.*, **2005**, *4*, 864-868.

36. Mor, G.K., Varghese, O.K., Paulose, M., Shankar, K., Grimes, C.A., *Sol. Energy Mater. Sol. Cells*, **2006**, *90*, 2011-2075.
37. Greene, L.E., Law, M., Yuhas, B.D., Yang, P.D., *J. Phys. Chem. C*, **2007**, *111*, 18451-18456.
38. Grimes, C.A., *J. Mater. Chem.*, **2007**, *17*, 1451-1457.
39. Sato, K., Dutta, M., Fukate, N., *Nanoscale*, **2014**, *6*, 6092-6101.
40. Thompson, B.C., Frechet, J.M.J., *Angew. Chem., Int. Ed.*, **2008**, *47*, 58-77.
41. Liu, Y., Chen, J.H.E., Teplyakov, A.V., *Langmuir*, **2012**, *28*, 15521-15528.
42. Zhang, X.C., Antonopoulos, I.H., Kumar, S., Chen, J., Teplyakov, A.V., *Appl. Surf. Sci.*, **2009**, *256*, 815-818.
43. Zhang, X.C., Kumar, S., Chen, J.H., Teplyakov, A.V., *Surf. Sci.*, **2009**, *603*, 2445-2457.
44. Zhang, X.C., Teplyakov, A.V., *Langmuir*, **2008**, *24*, 810-820.
45. Sun, Q.Y., de Smet, L., van Lagen, B., Giesbers, M., Thune, P.C., van Engelenburg, J., de Wolf, F.A., Zuilhof, H., Sudholter, E.J.R., *J. Am. Chem. Soc.*, **2005**, *127*, 2514-2523.
46. Battiston, F.M., Ramseyer, J.P., Lang, H.P., Baller, M.K., Gerber, C., Gimzewski, J.K., Meyer, E., Guntherodt, H.J., *Sens. Actuators, B*, **2001**, *77*, 122-131.
47. Sieval, A.B., Linke, R., Zuilhof, H., Sudholter, E.J.R., *Adv. Mater. (Weinheim, Ger.)*, **2000**, *12*, 1457-1460.
48. Yakovleva, J., Davidsson, R., Lobanova, A., Bengtsson, M., Eremin, S., Laurell, T., Emneus, J., *Anal. Chem.*, **2002**, *74*, 2994-3004.
49. Lin, Z., Strother, T., Cai, W., Cao, X.P., Smith, L.M., Hamers, R.J., *Langmuir*, **2002**, *18*, 788-796.
50. Jørgensen, M., Norrman, K., Krebs, F.C., *Sol. Energy Mater. Sol. Cells*, **2008**, *92*, 686-714.
51. Grossiord, N., Kroon, J.M., Andriessen, R., Blom, P.W.M., *Org. Electron.*, **2012**, *13*, 432-456.

52. PalDey, S., Deevi, S.C., *Mater. Sci. Eng., A*, **2003**, 342, 58-79.
53. Voevodin, A.A., Donley, M.S., *Surf. Coat. Technol.*, **1996**, 82, 199-213.
54. Gray, J.E., Luan, B., *J. Alloys Compd.*, **2002**, 336, 88-113.
55. Sanchez, C., Boissiere, C., Grosso, D., Laberty, C., Nicole, L., *Chem. Mater.*, **2008**, 20, 682-737.
56. Podgornik, B., Zajec, B., Bay, N., Vizintin, J., *Wear*, **2011**, 270, 850-856.
57. Sander, T., Tremmel, S., Wartzack, S., *Surf. Coat. Technol.*, **2011**, 206, 1873-1878.
58. Holleck, H., Schier, V., *Surf. Coat. Technol.*, **1995**, 76, 328-336.
59. Mao, Z., Ma, J., Wang, J., Sun, B., *J. Coat. Technol. Res.*, **2009**, 6, 243-250.
60. O'Hanlon, J.F., *J. Vac. Sci. Technol., A*, **1989**, 7, 2500-2503.
61. Drusedau, T.P., Lohmann, M., Garke, B., *J. Vac. Sci. Technol., A*, **1998**, 16, 2728-2732.
62. Li, Z.C., Zhang, W.H., Fan, X.D., Wu, P., Zeng, C.G., Li, Z.Y., Zhai, X.F., Yang, J.L., Hou, J.G., *J. Phys. Chem. C*, **2012**, 116, 10557-10562.
63. Heinke, W., Leyland, A., Matthews, A., Berg, G., Friedrich, C., Broszeit, E., *Thin Solid Films*, **1995**, 270, 431-438.
64. Stewart, D.A., Shipway, P.H., McCartney, D.G., *Wear*, **1999**, 225, 789-798.
65. Verdon, C., Karimi, A., Martin, J.L., *Mater. Sci. Eng., A*, **1998**, 246, 11-24.
66. Johnson, R.N., Sheldon, G.L., *J. Vac. Sci. Technol., A*, **1986**, 4, 2740-2746.
67. Usmani, S., Sampath, S., Houck, D.L., Lee, D., *Tribol. Trans.*, **1997**, 40, 470-478.
68. Padilla, K., Velasquez, A., Berrios, J.A., Cabrera, E.S.P., *Surf. Coat. Technol.*, **2002**, 150, 151-162.
69. Li, H., Khor, K.A., Cheang, P., *Eng. Fract. Mech.*, **2007**, 74, 1894-1903.
70. Frangini, S., Masci, A., *Surf. Coat. Technol.*, **2004**, 184, 31-39.

71. Knotek, O., Löffler, F., Kramer, G., *Surf. Coat. Technol.*, **1993**, *61*, 320-325.
72. Seidel, F., Stock, H.R., Mayr, P., *Surf. Coat. Technol.*, **1998**, *108*, 271-275.
73. Holleck, H., Schier, V., *Surf. Coat. Technol.*, **1995**, *76*, 328-336.
74. PalDey, S., Deevi, S.C., *Mat. Sci. Eng. A*, **2003**, *342*, 28-79.
75. Choy, K.L., *Prog. Mat. Sci.*, **2003**, *48*, 57-170.
76. Knotek, Löffler, F., Kramer, G., *Surf. Coat. Technol.*, **1993**, *61*, 320-325.
77. Seidel, F., Stock, H.-R., Mayr, P., *Surf. Coat. Technol.*, **1998**, *108-109*, 271-275.
78. Sproul, W.D., *Surf. Coat. Technol.*, **1996**, *81*, 1-7.
79. Liu, Y., RamaRao, N., Miller, T., Hadjipanayis, G., Teplyakov, A.V., *J. Phys. Chem. C*, **2013**, *117*, 19974-19983.
80. Yuasa, S., Djayaprawira, D.D., *J. Phys. D: Appl. Phys.*, **2007**, *40*, R337.
81. Polshettiwar, V., Varma, R.S., *Green Chem.*, **2010**, *12*, 743-754.
82. Cuenya, B.R., *Thin Solid Films*, **2010**, *518*, 3127-3150.
83. Deshpande, U.S., in: Electric Machines and Drives Conference, 2003. IEMDC'03. IEEE International, 2003, pp. 509-515 vol.501.
84. Guo, J., Yang, W., Wang, C., *Adv. Mater. (Weinheim, Ger.)*, **2013**, *25*, 5196-5214.
85. Li, Z., Luo, W., Zhang, M., Feng, J., Zou, Z., *Ener. Environ. Sci.*, **2013**, *6*, 347-370.
86. Ovits, O., Tel-Vered, R., Baravik, I., Wilner, O.I., Willner, I., *J. Mater. Chem.*, **2009**, *19*, 7650-7655.
87. Dai, M., Wang, Y., Kwon, J., Halls, M.D., Chabal, Y.J., *Nat. Mater.*, **2009**, *8*, 825-830.
88. Tian, F.Y., Taber, D.F., Teplyakov, A.V., *J. Am. Chem. Soc.*, **2011**, *133*, 20769-20777.

89. Tian, F.Y., Yang, D., Opila, R.L., Teplyakov, A.V., *Appl. Surf. Sci.*, **2012**, *258*, 3019-3026.
90. Zhang, X., Chabal, Y.J., Christman, S.B., Chaban, E.E., Garfunkel, E., *J. Vac. Sci. Technol., A*, **2001**, *19*, 1725-1729.
91. Zhang, X., Garfunkel, E., Chabal, Y.J., Christman, S.B., Chaban, E.E., *Appl. Phys. Lett.*, **2001**, *79*, 4051-4053.
92. Strother, T., Hamers, R.J., Smith, L.M., *Nucleic Acids Res.*, **2000**, *28*, 3535-3541.
93. Sieval, A.B., Linke, R., Heij, G., Meijer, G., Zuilhof, H., Sudholter, E.J.R., *Langmuir*, **2001**, *17*, 7554-7559.
94. Baldwin, M.J., Collins, G.A., Fewell, M.P., Haydon, S.C., Kumar, S., Short, K.T., Tendys, J., *Jpn. J. Appl. Phys., Part 1*, **1997**, *36*, 4941-4948.
95. Collman, J.P., Devaraj, N.K., Eberspacher, T.P.A., Chidsey, C.E.D., *Langmuir*, **2006**, *22*, 2457-2464.
96. Mader, H., Li, X., Saleh, S., Link, M., Kele, P., Wolfbeis, O.S., Fluorescent silica nanoparticles, in: Wolfbeis, O.S. (Ed.) *Fluorescence Methods and Applications: Spectroscopy, Imaging, and Probes*, 2008, pp. 218-223.
97. Rahman, I.A., Vejayakumar, P., Sipaut, C.S., Ismail, J., Chee, C.K., *Ceram. Int.*, **2008**, *34*, 2059-2066.
98. Nečas, D., Klapetek, P., *Cent. Eur. J. Phys.*, **2012**, *10*, 181-188.
99. Tricoteaux, A., Duarte, G., Chicot, D., Le Bourhis, E., Bemporad, E., Lesage, J., *Mech. Mater.*, **2010**, *42*, 166-174.
100. Miller, T., Teplyakov, A.V., *Langmuir*, **2014**, *30*, 5105-5114.
101. Troshin, P.A., Hoppe, H., Renz, J., Egginger, M., Mayorova, J.Y., Goryachev, A.E., Peregudov, A.S., Lyubovskaya, R.N., Gobsch, G., Sariciftci, N.S., Razumov, V.F., *Adv. Funct. Mater.*, **2009**, *19*, 779-788.
102. Wudl, F., *Acc. Chem. Res.*, **1992**, *25*, 157-161.
103. Padinger, F., Rittberger, R.S., Sariciftci, N.S., *Adv. Funct. Mater.*, **2003**, *13*, 85-88.

104. Yang, X.N., Loos, J., Veenstra, S.C., Verhees, W.J.H., Wienk, M.M., Kroon, J.M., Michels, M.A.J., Janssen, R.A.J., *Nano Lett.*, **2005**, *5*, 579-583.
105. Hummelen, J.C., Knight, B.W., Lepeq, F., Wudl, F., Yao, J., Wilkins, C.L., *J. Org. Chem.*, **1995**, *60*, 532-538.
106. Liu, C., Li, Y.J., Li, C.H., Li, W.W., Zhou, C.J., Liu, H.B., Bo, Z.S., Li, Y.L., *J. Phys. Chem. C*, **2009**, *113*, 21970-21975.
107. Duevel, R.V., Corn, R.M., *Anal. Chem.*, **1992**, *64*, 337-342.
108. Amelines-Sarria, O., Basiuk, V.A., *J. Comput. Theor. Nanosci.*, **2009**, *6*, 73-79.
109. Lin, T.T., Zhang, W.D., Huang, J.C., He, C.B., *J. Phys. Chem. B*, **2005**, *109*, 13755-13760.
110. Seshadri, R., Govindaraj, A., Nagarajan, R., Pradeep, T., Rao, C.N.R., *Tetrahedron Lett.*, **1992**, *33*, 2069-2070.
111. Becke, A.D., *Phys. Rev. A*, **1988**, *38*, 3098-3100.
112. Becke, A.D., *J. Chem. Phys.*, **1993**, *98*, 5648-5652.
113. Lee, C.T., Yang, W.T., Parr, R.G., *Phys. Rev. B*, **1988**, *37*, 785-789.
114. Stephens, P.J., Devlin, F.J., Chabalowski, C.F., Frisch, M.J., *J. Phys. Chem.*, **1994**, *98*, 11623-11627.
115. Frisch, M.J., Trucks, G.W., Schlegel, H.B., Scuseria, G.E., Robb, M.A., Cheeseman, J.R., Scalmani, G., Barone, V., Mennucci, B., Petersson, G.A., Nakatsuji, H., Caricato, M., Li, X., Hratchian, H.P., Izmaylov, A.F., Bloino, J., Zheng, G., Sonnenberg, J.L., Hada, M., Ehara, M., Toyota, K., Fukuda, R., Hasegawa, J., Ishida, M., Nakajima, T., Honda, Y., Kitao, O., Nakai, H., Vreven, T., Montgomery, J., J. A., Peralta, J.E., Ogliaro, F., Bearpark, M., Heyd, J.J., Brothers, E., Kudin, K.N., Staroverov, V.N., Kobayashi, R., Normand, J., Raghavachari, K., Rendell, A., Burant, J.C., Iyengar, S.S., Tomasi, J., Cossi, M., Rega, N., Millam, J.M., Klene, M., Knox, J.E., Cross, J.B., Bakken, V., Adamo, C., Jaramillo, J., Gomperts, R., Stratmann, R.E., Yazyev, O., Austin, A.J., Cammi, R., Pomelli, C., Ochterski, J.W., Martin, R.L., Morokuma, K., Zakrzewski, V.G., Voth, G.A., Salvador, P., Dannenberg, J.J., Dapprich, S., Daniels, A.D., Farkas, Ö., Foresman, J.B., Ortiz, J.V., Cioslowski, J., Fox, D.J., Gaussian 09, Revision A.1, Gaussian, Inc., Wallingford CT, 2009.

116. Pirolli, L., Teplyakov, A.V., *J. Phys. Chem. B*, **2006**, *110*, 4708-4716.
117. Rodriguez-Reyes, J.C.F., Teplyakov, A.V., *J. Phys. Chem. C*, **2007**, *111*, 4800-4808.
118. Leftwich, T.R., Teplyakov, A.V., *J. Electron Spectrosc. Relat. Phenom.*, **2009**, *175*, 31-40.
119. Perrine, K.A., Leftwich, T.R., Weiland, C.R., Madachik, M.R., Opila, R.L., Teplyakov, A.V., *J. Phys. Chem. C*, **2009**, *113*, 6643-6653.
120. Perrine, K.A., Lin, J.M., Teplyakov, A.V., *J. Phys. Chem. C*, **2012**, *116*, 14431-14444.
121. Sahoo, R.R., Patnaik, A., *J. Colloid Interface Sci.*, **2003**, *268*, 43-49.
122. Hamwi, A., Latouche, C., Marchand, V., Dupuis, J., Benoit, R., *J. Phys. Chem. Solids*, **1996**, *57*, 991-998.
123. Olsson, C.-O.A., Hörnström, S.E., *Corros. Sci.*, **1994**, *36*, 141-151.
124. Delpoux, S., Beguin, F., Benoit, R., Erre, R., Manolova, N., Rashkov, I., *Eur. Polym. J.*, **1998**, *34*, 905-915.
125. Grunthaler, F.J., Grunthaler, P.J., Vasquez, R.P., Lewis, B.F., Maserjian, J., Madhukar, A., *J. Vac. Sci. Technol.*, **1979**, *16*, 1443-1453.
126. Lin, J.L., Petrovykh, D.Y., Viernow, J., Men, F.K., Seo, D.J., Himpsel, F.J., *J. Appl. Phys.*, **1998**, *84*, 255-260.
127. Perring, M., Dutta, S., Arafat, S., Mitchell, M., Kenis, P.J.A., Bowden, N.B., *Langmuir*, **2005**, *21*, 10537-10544.
128. Porter, M.D., Bright, T.B., Allara, D.L., Chidsey, C.E.D., *J. Am. Chem. Soc.*, **1987**, *109*, 3559-3568.
129. Sieval, A.B., Demirel, A.L., Nissink, J.W.M., Linford, M.R., van der Maas, J.H., de Jeu, W.H., Zuilhof, H., Sudholter, E.J.R., *Langmuir*, **1998**, *14*, 1759-1768.
130. Snyder, R.G., Strauss, H.L., Elliger, C.A., *J. Phys. Chem.*, **1982**, *86*, 5145-5150.
131. Kansiz, M., Billman-Jacobe, H., McNaughton, D., *Appl. Environ. Microbiol.*, **2000**, *66*, 3415-3420.

132. Ghanbari, B., Taheri, Z., Shekarriz, M., Taghipoor, S., Mohajerani, B., Jamarani, M.S., *Fullerenes, Nanotubes, Carbon Nanostruct.*, **2006**, *14*, 315-319.
133. Miller, T., Lin, J.M., Pirolli, L., Coquilleau, L., Luharuka, R., Teplyakov, A.V., *Thin Solid Films*, **2012**, *522*, 193-198.
134. Bchir, O.J., Green, K.M., Ajmera, H.M., Zapp, E.A., Anderson, T.J., Brooks, B.C., Reitfort, L.L., Powell, D.H., Abboud, K.A., McElwee-White, L., *J. Am. Chem. Soc.*, **2005**, *127*, 7825-7833.
135. Rodriguez-Reyes, J.C.F., Ni, C., Bui, H.P., Beebe Jr., T.P., *Chem. Mater.*, **2009**, *21*, 5163-5169.
136. Rodríguez-Reyes, J.C.F., Teplyakov, A.V., *J. Phys. Chem. C*, **2007**, *111*, 4800-4808.
137. Rodríguez-Reyes, J.C.F., Teplyakov, A.V., *Chem. Eur. J.*, **2007**, *13*, 9164-9176.
138. Korkmaz, K., Bakan, H.I., *Kovove Mater.*, **2010**, *48*, 153-158.
139. Leo, A., Andronenko, S., Stiharu, I., Bhat, R.B., *Sensors*, **2010**, *10*, 1338-1354.
140. Zhang, S.Y., *Mater. Sci. Eng. A*, **1993**, *163*, 141-148.
141. Hsieh, J.H., Tan, A.L.K., Zeng, X.T., *Surf. Coat. Technol.*, **2006**, *201*, 4094-4098.
142. Lee, D.B., Kim, G.Y., Lee, J.K., *Met. Mater. Int.*, **2003**, *9*, 43-46.
143. Hsieh, J.H., Wu, W., Li, C., Yu, C.H., Tan, B.H., *Surf. Coat. Technol.*, **2003**, *163*, 233-237.
144. Bull, S.J., *Wear*, **1999**, *233*, 412-423.
145. Bonora, P.L., Deflorian, F., Fedrizzi, L., *Electrochim. Acta*, **1996**, *41*, 1073-1082.
146. Ni, C., Zhang, Z., Wells, M., Beebe Jr., T.P., Pirolli, L., Mendez de Leo, L.P., Teplyakov, A.V., *Thin Solid Films*, **2007**, *515*, 3030-3039.
147. Zhang, X.C., Kumar, S., Chen, J., Teplyakov, A.V., *Surf. Sci.*, **2009**, *603*, 2445-2457.

148. Zhang, X.C., Teplyakov, A.V., *Langmuir*, **2008**, *24*, 810-820.
149. Leftwich, T.R., Madachik, M.R., Teplyakov, A.V., *J. Am. Chem. Soc.*, **2009**, *130*, 16216-16223.
150. Leftwich, T.R., Teplyakov, A.V., *J. Electron. Spectrosc. Relat. Phenom.*, **2009**, *175*, 31-40.
151. Perrine, K.A., Leftwich, T.R., Weiland, C.R., Madachik, M.R., Opila, R.L., Teplyakov, A.V., *J. Phys. Chem. C*, **2009**, *113*, 6643-6653.
152. Bocharov, S., Zhang, Z., Beebe Jr., T.P., Teplyakov, A.V., *Thin Solid Films*, **2005**, *471*, 159-165.
153. Crocombette, J.P., Jollet, F., *J. Phys. : Condens. Matter.*, **1994**, *6*, 10811-10821.
154. Yaldiz, S., Saglam, H., Unsacar, F., Isik, H., *Mater. Design*, **2007**, *28*, 889-896.
155. Cardinal, S., Malchere, A., Garnier, V., Fantozzi, G., *Int. J. Refract. Met. Hard Mater.*, **2009**, *27*, 521-527.
156. Miller, T., Pirolli, L., Deng, F., Ni, C., Teplyakov, A.V., *Surf. Coat. Technol.*
157. Sheldon, G.L., Wang, R., Clark, R.A., *Surf. Coat. Technol.*, **1988**, *36*, 445-454.
158. Xie, Y.J., Wang, M.C., *Surf. Coat. Technol.*, **2006**, *201*, 691-698.
159. Duan, G., Liu, Y., Yang, G., Zhou, Y., *Mater. Lett.*, **2003**, *57*, 1091-1095.
160. Natesan, K., *Mater. Sci. Eng., A*, **1998**, *258*, 126-134.
161. Johnson, R.N., *Thin Solid Films*, **1984**, *118*, 31-47.
162. Frangini, S., Masci, A., Di Bartolomeo, A., *Surf. Coat. Technol.*, **2002**, *149*, 279-286.
163. Wang, R.J., Qian, Y.Y., Liu, J., *Appl. Surf. Sci.*, **2004**, *228*, 405-409.
164. Frangini, S., Loreti, S., Masci, A., *J. Fuel Cell Sci. Tech.*, **2005**, *2*, 60-64.
165. Xie, Y.J., Wang, M.C., Huang, D.W., *Appl. Surf. Sci.*, **2007**, *253*, 6149-6156.
166. Bogdan, A., Emil, E., Jaromir, A., *Trans. ASME J. Tribology*, **2008**, *130*.

167. Li, X., Sun, D.Q., Zheng, X.Y., Ren, Z.A., *Mater. Sci. Eng., A*, **2008**, *490*, 126-130.
168. Wang, W.F., Wang, M.C., Sun, F.J., Zheng, Y.G., Jiao, J.M., *Surf. Coat. Technol.*, **2008**, *202*, 5116-5121.
169. Ma, J., He, Y.D., Wang, J., Sun, B.D., *Corros. Eng. Sci. Techn.*, **2009**, *44*, 157-160.
170. Wang, J.S., Meng, H.M., Yu, H.Y., Fan, Z.S., Sun, D.B., *Rare Metals*, **2010**, *29*, 380-384.
171. Guo, P.Y., Shao, Y., Zeng, C.L., Wu, M.F., Li, W.L., *Mater. Lett.*, **2011**, *65*, 3180-3183.
172. Brown, E.A., Sheldon, G.L., Bayoumi, A.E., *Wear*, **1990**, *138*, 137-151.
173. Podchernyaeva, I.A., Yurechko, D.V., Bochko, A.V., Sedlyar, G.A., Kostenko, L.M., *Powder Metall. Met. C+*, **2012**, *51*, 198-203.
174. Wang, P.Z., Pan, G.S., Zhou, Y., Qu, J.X., Shao, H.S., *J. Mater. Eng. Perform.*, **1997**, *6*, 780-784.
175. Lesnjak, A., Tusek, J., *Z. Metallkd.*, **2003**, *94*, 1260-1266.
176. Wang, R.J., Qian, Y.Y., Liu, J., *Appl. Surf. Sci.*, **2005**, *240*, 42-47.
177. Levashov, E.A., Vakaev, P.V., Zamulaeva, E.I., Kudryashov, A.E., Pogozhev, Y.S., Shtansky, D.V., Voevodin, A.A., Sanz, A., *Thin Solid Films*, **2006**, *515*, 1161-1165.
178. Chivavibul, P., Watanabe, M., Kuroda, S., Shinoda, K., *Surf. Coat. Technol.*, **2007**, *202*, 509-521.
179. Levashov, E.A., Zamulaeva, E.I., Kudryashov, A.E., Vakaev, P.V., Petrzhik, M.I., Sanz, A., *Plasma Processes Polym.*, **2007**, *4*, 293-300.
180. Levashov, E.A., Vakaev, P.V., Zamulaeva, E.I., Kudryashov, A.E., Kurbatkina, V.V., Shtansky, D.V., Voevodin, A.A., Sanz, A., *Surf. Coat. Technol.*, **2007**, *201*, 6176-6181.
181. Radek, N., Wajs, E., Luchka, M., *Powder Metall. Met. C+*, **2008**, *47*, 197-201.
182. Zamulaeva, E.I., Levashov, E.A., Kudryashov, A.E., Vakaev, P.V., Petrzhik, M.I., *Surf. Coat. Technol.*, **2008**, *202*, 3715-3722.

183. Levashov, E.A., Zamulaeva, E.I., Pogozev, Y.S., Kurbatkina, V.V., *Plasma Processes Polym.*, **2009**, *6*, S102-S106.
184. Radek, N., *Eksploat. Niezawodn.*, **2009**, 10-16.
185. Bolelli, G., Bonferroni, B., Coletta, G., Lusvarghi, L., Pitacco, F., *Surf. Coat. Technol.*, **2011**, *205*, 4211-4220.
186. Korkmaz, K., Ribalko, A.V., *Kovove Mater.*, **2011**, *49*, 265-270.
187. Zamulaeva, E.I., Levashov, E.A., Kudryashov, A.E., *Metallurgist+*, **2012**, *55*, 628-633.
188. Podchernyaeva, I.A., Shchepetov, V.V., Panasyuk, A.D., Gromenko, V.Y., Yurechko, D.V., Katashinskii, V.P., *Powder Metall. Met. C+*, **2003**, *42*, 497-502.
189. Korkmaz, K., Bakan, H.I., *Kovove Mater.*, **2010**, *48*, 153-158.
190. Kessler, O.H., Hoffmann, F.T., Mayr, P., *Surf. Coat. Technol.*, **1999**, *120*, 366-372.
191. Puchi-Cabrera, E.S., Staia, M.H., Quinto, D.T., Villalobos-Gutierrez, C., Ochoa-Perez, E., *Int. J. Fatigue*, **2007**, *29*, 471-480.
192. Li, J.L., Zhang, S.H., Li, M.X., *Appl. Surf. Sci.*, **2013**, *283*, 134-144.
193. Bull, S.J., Bhat, D.G., Staia, M.H., *Surf. Coat. Technol.*, **2003**, *163*, 499-506.
194. Bocharov, S., Zhang, Z.P., Beebe, T.P., Teplyakov, A.V., *Thin Solid Films*, **2005**, *471*, 159-165.
195. Ni, C., Zhang, Z., Wells, M., Beebe, T.P., Jr., Pirolli, L., Mendez De Leo, L.P., Teplyakov, A.V., *Thin Solid Films*, **2007**, *515*, 3030-3039.
196. Rodriguez-Reyes, J.C.F., Ni, C.Y., Bui, H.P., Beebe, T.P., Teplyakov, A.V., *Chem. Mater.*, **2009**, *21*, 5163-5169.
197. Crocombette, J.P., Jollet, F., *J. Phys.: Condens. Matter*, **1994**, *6*, 10811-10821.
198. Nakazawa, M., Okamoto, H., *Appl. Surf. Sci.*, **1985**, *24*, 75-86.
199. Zellner, M.B., Chen, J.G.G., *Catal. Today*, **2005**, *99*, 299-307.

200. Menthe, E., Rie, K.T., Schultze, J.W., Simson, S., *Surf. Coat. Technol.*, **1995**, 74-5, 412-416.
201. Liu, J., Wang, R.J., Qian, Y.Y., *Surf. Coat. Technol.*, **2005**, 200, 2433-2437.
202. Ribalko, A.V., Sahin, O., *Surf. Coat. Technol.*, **2006**, 201, 1724-1730.
203. Heard, D.W., Brochu, M., *J. Mater. Process Tech.*, **2010**, 210, 892-898.
204. Chen, L.M., Lengauer, W., Dreyer, K., *Int. J. Refract. Met. Hard Mater.*, **2000**, 18, 153-161.
205. Qiu, G.B., Ma, S.W., Deng, Q.Y., Lv, X.W., Wang, H., *Metal. Int.*, **2012**, 17, 94-99.
206. Li, M.H., Shi, D., Christofides, P.D., *Powder Technol.*, **2005**, 156, 177-194.
207. Lengauer, W., Binder, S., Aigner, K., Ettmayer, P., Guillou, A., Debuigne, J., Groboth, G., *J. Alloys Compd.*, **1995**, 217, 137-147.
208. Reeber, R.R., Wang, K., *J. Am. Ceram. Soc.*, **1999**, 82, 129-135.
209. Arrazola, P.J., Arriola, I., Davies, M.A., *Cirp Annals-Manufacturing Technology*, **2009**, 58, 85-88.
210. Ribalko, A.V., Sahin, O., Korkmaz, K., *Surf. Coat. Technol.*, **2009**, 203, 3509-3515.
211. Parkansky, N., Beilis, I., Gindin, D., Alterkop, B., Boxman, R.L., Moshkovich, A., Perfilyev, V., Rapoport, L., Rosenberg, Y., *Surf. Coat. Technol.*, **2010**, 205, 287-293.
212. Karlsson, L., Hultman, L., Sundgren, J.E., *Thin Solid Films*, **2000**, 371, 167-177.
213. Amini, R., Shokrollahi, H., Salahinejad, E., Hadianfard, M.J., Marasi, M., Sritharan, T., *J. Alloys Compd.*, **2009**, 480, 617-624.
214. Yaldiz, S., Saglam, H., Unsacar, F., Isik, H., *Materials & Design*, **2007**, 28, 889-896.
215. Cardinal, S., Malchere, A., Garnier, V., Fantozzi, G., *Int. J. Refract. Met. Hard Mater.*, **2009**, 27, 521-527.
216. Bewilogua, K., Dimigen, H., *Surf. Coat. Technol.*, **1993**, 61, 144-150.

217. Kolb, H.C., Finn, M.G., Sharpless, K.B., *Angew. Chem., Int. Ed.*, **2001**, *40*, 2004-+.
218. Kolb, H.C., Sharpless, K.B., *Drug Discov. Today*, **2003**, *8*, 1128-1137.
219. Lipinski, C., Hopkins, A., *Nature*, **2004**, *432*, 855-861.
220. Hjorringgaard, C.U., Vad, B.S., Matchkov, V.V., Nielsen, S.B., Vosegaard, T., Nielsen, N.C., Otzen, D.E., Skrydstrup, T., *J. Phys. Chem. B*, **2012**, *116*, 7652-7659.
221. Fournier, D., Hoogenboom, R., Schubert, U.S., *Chem. Soc. Rev.*, **2007**, *36*, 1369-1380.
222. Binder, W.H., Sachsenhofer, R., *Macromol. Rapid Commun.*, **2007**, *28*, 15-54.
223. Acikgoz, S., Aktas, G., Inci, M.N., Altin, H., Sanyal, A., *J. Phys. Chem. B*, **2010**, *114*, 10954-10960.
224. Toulemon, D., Pichon, B.P., Cattoen, X., Man, M.W.C., Begin-Colin, S., *Chem. Commun. (Cambridge, U. K.)*, **2011**, *47*, 11954-11956.
225. Toulemon, D., Pichon, B.P., Leuvrey, C., Zafeiratos, S., Papaefthimiou, V., Cattoen, X., Begin-Colin, S., *Chem. Mater.*, **2013**, *25*, 2849-2854.
226. Dafinone, M.I., Feng, G., Brugarolas, T., Tettey, K.E., Lee, D., *ACS Nano*, **2011**, *5*, 5078-5087.
227. Chen, W., McCarthy, T.J., *Macromolecules*, **1997**, *30*, 78-86.
228. Khademhosseini, A., Suh, K.Y., Yang, J.M., Eng, G., Yeh, J., Levenberg, S., Langer, R., *Biomaterials*, **2004**, *25*, 3583-3592.
229. Zhang, J., Senger, B., Vautier, D., Picart, C., Schaaf, P., Voegel, J.-C., Lavallo, P., *Biomaterials*, **2005**, *26*, 3353-3361.
230. Dubas, S.T., Kumlangdudsana, P., Potiyaraj, P., *Colloids Surf., A*, **2006**, *289*, 105-109.
231. Jiang, C., Tsukruk, V.V., *Adv. Mater. (Weinheim, Ger.)*, **2006**, *18*, 829-840.
232. Nishiyama, F., Yokoyama, T., Kamikado, T., Yokoyama, S., Mashiko, S., *Appl. Phys. Lett.*, **2006**, *88*, -.
233. Tian, F.Y., Ni, C.Y., Teplyakov, A.V., *Appl. Surf. Sci.*, **2010**, *257*, 1314-1318.

234. Snyder, R.G., Strauss, H.L., Elliger, C.A., *J. Phys. Chem.*, **1982**, *86*, 5145-5150.
235. Wind, R.W., Fabreguette, F.H., Sechrist, Z.A., George, S.M., *J. Appl. Phys.*, **2009**, *105*.

**Appendix A**  
**DFT MODEL XYZ COORDINATES**

Table A.1: PCBM Coordinates

Atom	x	y	z
C	1.4090	-1.9284	-0.5442
C	1.1222	-1.3715	-1.8915
C	1.2464	-0.0039	-2.1470
C	2.1439	0.3527	0.3355
C	1.8109	-1.1009	0.5073
C	0.4512	-3.0042	-0.3006
C	-0.4163	-3.1251	-1.4713
C	-0.0038	-2.1172	-2.4461
C	-0.9756	-1.4701	-3.2323
C	0.2110	0.6719	-2.9113
C	0.8836	2.1385	-1.1849
C	0.4212	2.7736	-0.0311
C	0.7058	2.2172	1.3158
C	1.4433	1.0423	1.4682
C	0.9885	0.0344	2.4102
C	1.2122	-1.2825	1.8198
C	0.3068	-2.3274	2.0716
C	-0.0829	-3.2117	0.9850
C	-1.7755	-3.4441	-1.3155
C	-2.3308	-3.6467	0.0239
C	-1.5004	-3.5334	1.1507
C	-1.9844	-2.8425	2.3481
C	-0.8641	-2.0959	2.9197
C	-1.0787	-0.8306	3.4870
C	-0.1313	0.2555	3.2305
C	-0.8801	1.4944	3.0976
C	-0.4725	2.4486	2.1461
C	-0.0116	1.9887	-2.3199
C	-3.7168	2.7370	0.3414

Table A.1 continued.

C	-3.1917	2.9255	-0.9473
C	-3.5969	2.0365	-2.0388
C	-4.5062	0.9932	-1.7947
C	-5.0526	0.7989	-0.4517
C	-4.3856	1.1057	1.9229
C	-3.2617	1.8488	2.4902
C	-2.8416	2.8520	1.5099
C	-1.4773	3.1402	1.3403
C	-0.9265	3.3342	0.0001
C	-1.7725	3.2361	-1.1207
C	-2.4263	1.8001	-2.8835
C	-2.2122	0.5348	-3.4513
C	-3.1585	-0.5519	-3.1996
C	-4.2827	-0.3274	-2.3875
C	-4.6915	-1.3367	-1.4103
C	-5.1693	-0.6408	-0.2141
C	-4.9001	-1.1670	1.0600
C	-4.5025	-0.2761	2.1512
C	-2.2999	1.1845	3.2682
C	-2.4231	-0.2552	3.5094
C	-3.5007	-0.9706	2.9604
C	-3.2770	-2.2915	2.3681
C	-4.1408	-2.4117	1.1931
C	-3.6771	-3.0774	0.0457
C	-3.9585	-2.5289	-1.2834
C	-2.7857	-2.7602	-2.1253
C	-2.3927	-1.7933	-3.0650
C	-1.3031	2.5436	-2.3096
C	-0.8658	-0.0393	-3.4681
C	-4.6672	1.6548	0.5941
C	1.8247	0.9703	-1.1644
C	3.2362	0.9416	-0.5629
C	3.8527	2.2694	-0.1716
C	4.0264	3.2697	-1.1515
C	4.3503	2.4905	1.1284
C	4.6835	4.4717	-0.8376
H	3.6422	3.1104	-2.1571
C	5.0075	3.6926	1.4459
H	4.2241	1.7279	1.8929
C	5.1769	4.6872	0.4643

Table A.1 continued

H	4.8072	5.2365	-1.6005
H	5.3858	3.8506	2.4528
H	5.6837	5.6173	0.7098
C	4.2470	-0.0398	-1.1875
H	4.7371	0.4780	-2.0247
H	3.7261	-0.9032	-1.6164
C	5.3098	-0.5357	-0.1851
H	5.8756	0.3094	0.2219
H	4.8197	-1.0240	0.6673
C	6.2815	-1.5279	-0.8473
H	5.7460	-2.3989	-1.2508
H	6.7967	-1.0686	-1.7028
C	7.3402	-2.0389	0.1125
O	7.4534	-1.7444	1.3138
O	8.2042	-2.9102	-0.5270
C	9.2886	-3.4947	0.2845
H	9.8341	-4.1438	-0.4017
H	9.9351	-2.7033	0.6767
H	8.8699	-4.0660	1.1191

Table A.2: Si111-AUD Coordinates

Atom	x	y	z
Si	4.8489	2.7952	0.0138
Si	2.3681	0.5831	-1.9165
Si	4.5497	1.4766	-1.9164
Si	6.1246	-0.2757	-1.9203
Si	3.6325	-2.4907	-0.0133
Si	5.8187	-1.6118	-0.0036
Si	6.1152	-0.2933	1.9266
H	3.4429	-3.3445	-1.2184
H	4.7268	2.2911	3.1518
H	1.3740	1.6805	1.9467
Si	2.0115	-0.7681	-0.0093
Si	2.3589	0.5647	1.9125
Si	4.5402	1.4589	1.9304
H	2.1460	-0.2573	3.1360
H	3.4366	-3.3553	1.1830

Table A.2 continued.

H	1.3836	1.6994	-1.9445
H	2.1601	-0.2273	-3.1484
H	4.7426	2.3196	-3.1294
H	3.8677	3.9131	0.0165
H	6.2150	3.3836	0.0200
H	5.9537	-1.1037	-3.1442
H	7.5029	0.2835	-1.9346
H	7.4936	0.2653	1.9531
H	5.9376	-1.1323	3.1420
H	6.8092	-2.7243	-0.0064
N	-13.6279	1.0179	0.0250
C	-11.1633	0.7135	0.0334
C	-9.9848	-0.2823	-0.0007
C	-8.6045	0.4094	0.0283
C	-7.4235	-0.5844	-0.0061
C	-6.0420	0.1043	0.0208
C	-4.8634	-0.8924	-0.0130
C	-3.4798	-0.2073	0.0107
C	-2.3054	-1.2095	-0.0180
C	-0.9189	-0.5259	-0.0001
C	0.2488	-1.5441	-0.0190
H	-13.6033	1.6844	-0.7433
H	-11.0838	1.4001	-0.8265
H	-11.1113	1.3357	0.9377
H	-10.0633	-0.9690	0.8578
H	-10.0572	-0.9075	-0.9056
H	-8.5256	1.0977	-0.8288
H	-8.5300	1.0326	0.9338
H	-7.5027	-1.2723	0.8513
H	-7.5003	-1.2081	-0.9116
H	-5.9619	0.7916	-0.8369
H	-5.9646	0.7282	0.9259
H	-4.9434	-1.5782	0.8460
H	-4.9430	-1.5179	-0.9170
H	-3.3979	0.4752	-0.8507
H	-3.4009	0.4204	0.9129
H	-2.3856	-1.8887	0.8461
H	-2.3868	-1.8400	-0.9181
H	-0.8421	0.1490	-0.8667
H	-0.8458	0.1107	0.8953

Table A.2 continued

H	0.1678	-2.2136	0.8510
H	0.1655	-2.1841	-0.9106
C	-12.5394	0.0223	0.0001
H	-12.5789	-0.6514	-0.8803
H	-12.6433	-0.6131	0.8910
H	-14.5583	0.6372	0.1758

Table A.3: Si111-AUD-PCBM **Structure 1** Coordinates

Atom	x	y	z
Si	-18.6460	-1.6168	2.9691
Si	-16.4267	-2.2247	-0.1111
Si	-18.4205	-2.8553	0.9769
Si	-20.2601	-2.4193	-0.4295
Si	-18.3242	0.4996	-2.0127
Si	-20.3269	-0.1194	-0.9375
Si	-20.5541	1.1148	1.0565
H	-18.1859	-0.2614	-3.2851
H	-18.8518	1.4670	3.7205
H	-15.5635	1.0537	2.2776
Si	-16.4444	0.0801	-0.6396
Si	-16.7162	1.2999	1.3682
Si	-18.7121	0.6834	2.4614
H	-16.7435	2.7575	1.0647
H	-18.3706	1.9468	-2.3601
H	-15.2694	-2.5426	0.7701
H	-16.2674	-3.0201	-1.3599
H	-18.3730	-4.3090	1.2986
H	-17.4989	-1.9022	3.8721
H	-19.8939	-2.0153	3.6738
H	-20.1361	-3.2107	-1.6829
H	-21.5210	-2.8257	0.2469
H	-21.8149	0.7326	1.7471
H	-20.6238	2.5679	0.7462
H	-21.4847	0.1613	-1.8317
N	-0.7236	0.4534	-1.0580
C	-3.2295	0.5157	-0.9813
C	-4.5202	0.7870	-1.7833

Table A.3 continued.

C	-5.7993	0.5347	-0.9563
C	-7.1027	0.8138	-1.7352
C	-8.3733	0.5193	-0.9090
C	-9.6850	0.7935	-1.6758
C	-10.9481	0.4605	-0.8523
C	-12.2648	0.7225	-1.6153
C	-13.5218	0.3440	-0.7985
C	-14.8398	0.5934	-1.5734
H	-0.5633	-0.4890	-0.7216
H	-3.2546	-0.5157	-0.5926
H	-3.1855	1.1833	-0.1088
H	-4.5145	1.8284	-2.1414
H	-4.5370	0.1481	-2.6813
H	-5.8038	-0.5109	-0.6076
H	-5.7761	1.1630	-0.0515
H	-7.1142	1.8661	-2.0617
H	-7.1165	0.2035	-2.6527
H	-8.3576	-0.5342	-0.5856
H	-8.3574	1.1258	0.0110
H	-9.7153	1.8521	-1.9801
H	-9.6923	0.2026	-2.6059
H	-10.9111	-0.5980	-0.5475
H	-10.9422	1.0515	0.0778
H	-12.3192	1.7860	-1.8977
H	-12.2596	0.1495	-2.5564
H	-13.4514	-0.7168	-0.5122
H	-13.5263	0.9184	0.1409
H	-14.9207	1.6600	-1.8322
H	-14.8151	0.0442	-2.5271
C	-1.9522	0.7171	-1.8247
H	-1.9787	0.0610	-2.7074
H	-1.8844	1.7514	-2.1762
C	0.1719	1.4398	-0.7026
C	1.3130	0.9907	0.2159
O	0.0466	2.6359	-1.0785
C	2.6446	1.7012	-0.1035
H	1.4374	-0.1012	0.1771
H	1.0116	1.2419	1.2450
C	3.6901	1.4404	1.0010
H	2.4471	2.7724	-0.2107

Table A.3 continued.

H	3.0254	1.3452	-1.0718
C	5.0702	2.0599	0.7107
H	3.3310	1.8658	1.9496
H	3.7846	0.3604	1.1607
C	5.9878	1.3220	-0.2708
C	6.2839	1.3768	1.3552
C	5.0571	3.5747	0.6835
C	5.7804	-0.0550	-0.8314
C	7.0587	1.9272	-1.1297
C	6.3026	0.0461	2.0469
C	7.5763	2.0292	1.7465
C	5.1251	4.2920	1.8965
C	4.8734	4.2823	-0.5211
C	5.6835	-1.2026	-0.0401
C	6.4612	-0.1362	-2.1139
C	8.1480	2.6346	-0.6188
C	7.2445	1.0830	-2.2974
C	5.9476	-1.1513	1.4212
C	7.3853	0.0458	3.0166
C	8.4108	2.6871	0.8416
C	8.1681	1.2650	2.8315
C	5.0152	5.6930	1.9054
H	5.2691	3.7556	2.8324
C	4.7637	5.6842	-0.5157
H	4.8150	3.7414	-1.4624
C	6.1980	-2.4768	-0.5350
C	6.9424	-1.3603	-2.6095
C	9.4393	2.5696	-1.2962
C	8.4777	1.0300	-2.9707
C	6.6175	-2.3943	1.7922
C	8.0231	-1.1476	3.3969
C	9.8581	2.6536	1.0302
C	9.5586	1.2443	3.0368
C	4.8339	6.3945	0.6974
H	5.0722	6.2347	2.8464
H	4.6194	6.2175	-1.4519
C	6.7703	-3.2131	0.5909
C	6.8055	-2.5619	-1.8021
C	8.2296	-1.4170	-3.3047
C	9.6032	1.7949	-2.4599

Table A.3 continued.

C	10.4942	2.5862	-0.2844
C	8.9817	-0.2460	-3.4808
C	7.6286	-2.3998	2.7719
C	9.4724	-1.1719	3.6024
C	10.4266	1.9582	2.1144
C	10.2242	-0.0006	3.4255
H	4.7487	7.4784	0.7021
C	7.9203	-3.9990	0.4120
C	8.0098	-3.3717	-1.9890
C	8.8919	-2.6630	-2.9193
C	10.8153	0.9971	-2.6488
C	11.6626	1.8291	-0.4677
C	10.4306	-0.2671	-3.2808
C	8.8327	-3.2091	2.5822
C	9.9743	-2.4492	3.0967
C	11.6376	1.1594	1.9232
C	11.5125	-0.0536	2.7348
C	8.5574	-4.0757	-0.9042
C	8.9765	-3.9927	1.4260
C	10.2834	-2.6853	-2.7244
C	11.8248	1.0126	-1.6725
C	12.2442	1.0955	0.6582
C	11.0690	-1.4628	-2.9096
C	11.2115	-2.5027	2.4323
C	11.9962	-1.2796	2.2473
C	10.0053	-4.1032	-0.7041
C	10.2645	-4.0523	0.7369
C	10.8517	-3.4210	-1.5948
C	12.4917	-0.2304	-1.2887
C	12.7510	-0.1792	0.1524
C	12.1215	-1.4439	-1.8933
C	11.3593	-3.3208	1.2283
C	12.6288	-1.3436	0.9298
C	11.9885	-2.6548	-1.0814
C	12.2370	-2.6058	0.3000

Table A.4: Si111-AUD-PCBM **Structure 2** Coordinates

Atom	x	y	z
Si	17.9838	-2.4029	1.3765
Si	15.6781	0.6335	1.8872
Si	17.8351	-0.2332	2.2832
Si	19.4439	1.1550	1.2649
Si	16.8821	2.1034	-1.4351
Si	19.0434	1.2428	-1.0553
Si	19.1945	-0.9274	-1.9598
H	16.7928	3.4829	-0.8815
H	17.6727	-3.6867	-1.5179
H	14.4185	-2.3399	-0.7219
Si	15.2282	0.7421	-0.4317
Si	15.4318	-1.4352	-1.3311
Si	17.5839	-2.3149	-0.9442
H	15.1675	-1.3926	-2.7962
H	16.6296	2.1919	-2.8999
H	14.6720	-0.2292	2.5657
H	15.5716	1.9952	2.4804
H	18.0851	-0.2908	3.7506
H	16.9834	-3.2903	2.0280
H	19.3352	-2.9676	1.6362
H	19.3661	2.5238	1.8420
H	20.8088	0.6241	1.5257
H	20.5565	-1.4780	-1.7269
H	18.9645	-0.8784	-3.4286
H	20.0545	2.1240	-1.7034
N	-0.2982	-1.0436	0.8636
C	2.1327	-0.6516	0.6155
C	3.2539	0.2315	0.0267
C	4.6637	-0.2614	0.4178
C	5.8035	0.6051	-0.1597
C	7.2058	0.0941	0.2354
C	8.3593	0.9441	-0.3399
C	9.7541	0.4035	0.0427
C	10.9191	1.2344	-0.5383
C	12.3061	0.6494	-0.1858
C	13.4786	1.4689	-0.7809
H	-0.1516	-1.1338	1.8698
H	2.2284	-0.6692	1.7140
H	2.2520	-1.6893	0.2739

Table A.4 continued.

H	3.1667	0.2513	-1.0714
H	3.1229	1.2705	0.3687
H	4.7474	-0.2838	1.5164
H	4.7910	-1.3012	0.0764
H	5.7216	0.6307	-1.2583
H	5.6827	1.6447	0.1853
H	7.2867	0.0696	1.3342
H	7.3200	-0.9474	-0.1064
H	8.2723	0.9796	-1.4379
H	8.2594	1.9830	0.0136
H	9.8426	0.3708	1.1406
H	9.8445	-0.6379	-0.3066
H	10.8167	1.2880	-1.6341
H	10.8527	2.2696	-0.1671
H	12.4055	0.5976	0.9095
H	12.3532	-0.3887	-0.5496
H	13.3567	1.5473	-1.8720
H	13.4484	2.4972	-0.3901
C	0.7210	-0.1664	0.2403
H	0.6003	0.8925	0.5359
H	0.6005	-0.2045	-0.8514
C	-2.1729	0.7013	0.7747
C	-2.6128	-1.4733	1.6170
C	-2.8156	0.8369	2.0638
C	-2.5020	1.5867	-0.2410
C	-3.0893	-0.5056	2.5817
C	-3.3554	-2.6209	1.3861
C	-2.5963	-0.2564	-1.9201
C	-3.0399	-2.4260	-1.0766
C	-3.7197	1.8857	2.3229
C	-3.4553	2.6628	-0.0045
C	-2.7168	1.0963	-1.6319
C	-4.2529	-0.7428	3.3397
C	-3.5716	-3.1202	-0.0001
C	-4.5770	-2.8734	2.1379
C	-3.5746	-0.8864	-2.7807
C	-3.8469	-2.2258	-2.2605
C	-4.0480	2.8241	1.2610
C	-4.9366	1.6310	3.0953
C	-4.2598	2.8412	-1.2117

Table A.4 continued.

C	-3.7982	1.8798	-2.2123
C	-5.1966	0.3468	3.5929
C	-5.0173	-1.9583	3.1113
C	-4.9214	-3.6610	-0.0678
C	-5.5460	-3.5064	1.2452
C	-4.6107	-0.1389	-3.3776
C	-5.1444	-2.7695	-2.3581
C	-5.4693	3.1510	1.3662
C	-6.0156	2.4161	2.4962
C	-5.6247	3.1566	-1.1102
C	-4.7264	1.2803	-3.0844
C	-6.5474	-0.2086	3.5126
C	-6.4383	-1.6287	3.2165
C	-5.6966	-3.5040	-1.2320
C	-6.9106	-3.1905	1.3464
C	-5.9604	-0.6983	-3.4579
C	-6.2210	-1.9831	-2.9609
C	-6.2486	3.3065	0.2037
C	-7.3128	1.8794	2.4083
C	-6.5938	2.5220	-2.0028
C	-6.1481	1.6079	-2.9765
C	-7.5838	0.5411	2.9276
C	-7.3693	-2.2258	2.3452
C	-7.1172	-3.1727	-1.1256
C	-7.7152	-3.0109	0.1384
C	-6.9067	0.3888	-3.2074
C	-7.4394	-2.2363	-2.1913
C	-7.6018	2.7667	0.1346
C	-8.1392	2.0907	1.2329
C	-7.8179	2.2740	-1.2505
C	-8.5807	-0.0859	2.0770
C	-8.4541	-1.4432	1.7644
C	-8.6716	-1.9357	0.3784
C	-8.0728	0.1486	-2.4583
C	-8.3453	-1.1903	-1.9411
C	-9.0910	0.9388	1.1087
C	-8.5638	1.1191	-1.4971
C	-9.0106	-1.0580	-0.6559
C	-10.4650	0.9554	0.4266
C	-9.3349	0.3908	-0.4373

Table A.4 continued.

C	-11.0446	2.3077	0.0632
C	-11.5197	-0.0363	0.9548
C	-11.2757	3.2586	1.0799
C	-11.4531	2.6006	-1.2534
H	-12.0438	0.4517	1.7895
H	-11.0321	-0.9254	1.3700
C	-12.5394	-0.4719	-0.1181
C	-11.9016	4.4821	0.7860
H	-10.9596	3.0440	2.0988
C	-12.0788	3.8244	-1.5511
H	-11.2815	1.8767	-2.0461
H	-13.0668	0.4000	-0.5203
H	-12.0167	-0.9391	-0.9628
C	-13.5615	-1.4664	0.4590
C	-12.3059	4.7693	-0.5327
H	-12.0698	5.2083	1.5776
H	-12.3885	4.0375	-2.5712
H	-13.0638	-2.3614	0.8580
H	-14.1095	-1.0254	1.3039
C	-14.5817	-1.9216	-0.5680
H	-12.7883	5.7162	-0.7628
O	-14.6496	-1.5607	-1.7544
O	-15.4696	-2.8263	-0.0118
C	-16.5216	-3.3619	-0.8959
H	-17.0907	-4.0505	-0.2700
H	-17.1554	-2.5491	-1.2647
H	-16.0711	-3.8829	-1.7466
C	-1.7278	-0.7784	0.5507
C	-2.0071	-1.2905	-0.9435
H	-1.0300	-1.6483	-1.2937

## Appendix B

### COPYRIGHT PERMISSIONS

Rightslink® by Copyright Clearance Center

https://s100.copyright.com/AppDispatchServlet

HomeCreate AccountHelp

**ACS Publications**  
MOST TRUSTED. MOST CITED. MOST READ.

**Title:** Attachment Chemistry of PCBM to a Primary-Amine-Terminated Organic Monolayer on a Si(111) Surface

**Author:** Timothy Miller and Andrew V. Teplyakov

**Publication:** Langmuir

**Publisher:** American Chemical Society

**Date:** May 1, 2014

Copyright © 2014, American Chemical Society

User ID

Password

Enable Auto Login

**LOGIN**

[Forgot Password/User ID?](#)

If you're a **copyright.com** user, you can login to RightsLink using your copyright.com credentials. Already a **RightsLink** user or want to [learn more?](#)

#### PERMISSION/LICENSE IS GRANTED FOR YOUR ORDER AT NO CHARGE

This type of permission/license, instead of the standard Terms & Conditions, is sent to you because no fee is being charged for your order. Please note the following:

- Permission is granted for your request in both print and electronic formats, and translations.
- If figures and/or tables were requested, they may be adapted or used in part.
- Please print this page for your records and send a copy of it to your publisher/graduate school.
- Appropriate credit for the requested material should be given as follows: "Reprinted (adapted) with permission from (COMPLETE REFERENCE CITATION). Copyright (YEAR) American Chemical Society." Insert appropriate information in place of the capitalized words.
- One-time permission is granted only for the use specified in your request. No additional uses are granted (such as derivative works or other editions). For any other uses, please submit a new request.

**BACK**

**CLOSE WINDOW**

Copyright © 2014 [Copyright Clearance Center, Inc.](#) All Rights Reserved. [Privacy statement.](#) Comments? We would like to hear from you. E-mail us at [customercare@copyright.com](mailto:customercare@copyright.com)

**ELSEVIER LICENSE  
TERMS AND CONDITIONS**

Jun 03, 2014

---

This is a License Agreement between Timothy Miller ("You") and Elsevier ("Elsevier") provided by Copyright Clearance Center ("CCC"). The license consists of your order details, the terms and conditions provided by Elsevier, and the payment terms and conditions.

**All payments must be made in full to CCC. For payment instructions, please see information listed at the bottom of this form.**

Supplier	Elsevier Limited The Boulevard, Langford Lane Kidlington, Oxford, OX5 1GB, UK
Registered Company Number	1982084
Customer name	Timothy Miller
Customer address	University of Delaware NEWARK, DE 19716
License number	3401561441014
License date	Jun 03, 2014
Licensed content publisher	Elsevier
Licensed content publication	Thin Solid Films
Licensed content title	Investigation of thin titanium carbonitride coatings deposited onto stainless steel
Licensed content author	Timothy Miller, Jia-Ming Lin, Laurent Pirolli, Laurent Coquilleau, Rajesh Luharuka, Andrew V. Teplyakov
Licensed content date	1 November 2012
Licensed content volume number	522
Licensed content issue number	None
Number of pages	6
Start Page	193
End Page	198
Type of Use	reuse in a thesis/dissertation
Portion	full article
Format	both print and electronic

[Print This Page](#)



# RightsLink®

[Help](#)


**Title:** Structurally Different Interfaces between Electrospray-Deposited Titanium Carbonitride and Tungsten Carbide Films on Steel

**Author:** Timothy Miller, Laurent Pirolli, Fei Deng, Chaoying Ni, Andrew V. Teplyakov

**Publication:** Surface and Coatings Technology

**Publisher:** Elsevier

**Date:** Dec 31, 1969

Copyright © 1969, Elsevier

User ID	<input type="text"/>
Password	<input type="password"/>
<input type="checkbox"/> Enable Auto Login	
<input type="button" value="LOGIN"/>	
<a href="#">Forgot Password/User ID?</a>	
<p>If you're a <b>copyright.com</b> user, you can login to RightsLink using your copyright.com credentials. Already a <b>RightsLink</b> user or want to <a href="#">learn more?</a></p>	

## Order Completed

Thank you very much for your order.

This is a License Agreement between Timothy Miller ("You") and Elsevier ("Elsevier") The license consists of your order details, the terms and conditions provided by Elsevier, and the [payment terms and conditions](#).

License number	Reference confirmation email for license number
License date	Aug 05, 2014
Licensed content publisher	Elsevier
Licensed content publication	Surface and Coatings Technology
Licensed content title	Structurally Different Interfaces between Electrospray-Deposited Titanium Carbonitride and Tungsten Carbide Films on Steel
Licensed content author	Timothy Miller, Laurent Pirolli, Fei Deng, Chaoying Ni, Andrew V. Teplyakov
Licensed content date	Available online 4 August 2014
Licensed content volume number	n/a
Licensed content issue number	n/a
Number of pages	1
Type of Use	reuse in a thesis/dissertation
Portion	full article
Format	both print and electronic
Are you the author of this Elsevier article?	Yes
Will you be translating?	No
Title of your thesis/dissertation	Fabrication and Characterization of Thin Films and Coatings



RightsLink®

Home

Create Account

Help

ACS Publications  
MOST TRUSTED. MOST CITED. MOST READ.**Title:** Controlling Physical Properties of Iron Nanoparticles during Assembly by "Click Chemistry"**Author:** Yue Liu, Neelam RamaRao, Timothy Miller, George Hadjipanayis, and Andrew V. Teplyakov**Publication:** The Journal of Physical Chemistry C**Publisher:** American Chemical Society**Date:** Oct 1, 2013

Copyright © 2013, American Chemical Society

User ID
<input type="text"/>
Password
<input type="text"/>
<input type="checkbox"/> Enable Auto Login
<input type="button" value="LOGIN"/>
<a href="#">Forgot Password/User ID?</a>
<b>If you're a copyright.com user,</b> you can login to RightsLink using your copyright.com credentials. Already a <b>RightsLink user</b> or want to <a href="#">learn more?</a>

**PERMISSION/LICENSE IS GRANTED FOR YOUR ORDER AT NO CHARGE**

This type of permission/license, instead of the standard Terms & Conditions, is sent to you because no fee is being charged for your order. Please note the following:

- Permission is granted for your request in both print and electronic formats, and translations.
- If figures and/or tables were requested, they may be adapted or used in part.
- Please print this page for your records and send a copy of it to your publisher/graduate school.
- Appropriate credit for the requested material should be given as follows: "Reprinted (adapted) with permission from (COMPLETE REFERENCE CITATION). Copyright (YEAR) American Chemical Society." Insert appropriate information in place of the capitalized words.
- One-time permission is granted only for the use specified in your request. No additional uses are granted (such as derivative works or other editions). For any other uses, please submit a new request.

Copyright © 2014 [Copyright Clearance Center, Inc.](#) All Rights Reserved. [Privacy statement.](#) Comments? We would like to hear from you. E-mail us at [customercare@copyright.com](mailto:customercare@copyright.com)